

## ABSTRACT

Title of dissertation: SYNTHESIS OF POROUS FILMS FROM NANOPARTICLE AGGREGATES AND STUDY OF THEIR PROCESSING-STRUCTURE-PROPERTY RELATIONSHIPS

Oluwatosin A. Ogunsola, Doctor of Philosophy, 2005

Dissertation directed by: Professor Sheryl H. Ehrman  
Department of Chemical and Biomolecular Engineering

Porous films made from titania nanoparticle aggregates have a variety of uses in high surface area applications such as gas sensors, photocatalysts in treatment of wastewater and air pollutants, optical filters, and photovoltaic electrodes for low cost solar cells. A hybrid process based upon gas-to-particle conversion and particle precipitated chemical vapor deposition was used to synthesize porous films of titania nanoparticle aggregates. The residence time of particles in the reactor was varied and the influence on particle morphology and mechanical properties was studied. An increase in residence time resulted in an increase in primary particle diameter but did not significantly affect aggregate diameter, over the range of residence times considered in this study. The Young's modulus is shown to increase with a decrease in primary particle diameter.

A study of the effect of post processing annealing on the particle morphology and mechanical properties was conducted. Increasing the annealing temperature resulted in particle growth at different temperatures and aggregate growth only at the highest temperature studied. The Young's modulus, however, shows only an

influence of aggregate diameter, increasing as aggregate diameter increased. It is interesting to note that annealing did not result in a significant increase in Young's modulus or hardness until most of the surface area was lost. This suggests that annealing may not be the most effective process for strengthening films, if preservation of high surface area is desired.

To better understand the effect of change in particle and aggregate diameters on Young's modulus, Monte Carlo and continuum methods were employed to explore structure-property relationships. A Monte Carlo method was used to simulate particle deposits and a finite element method was used to calculate the Young's modulus from strain energy of the deposits simulated. The results of this study indicate that a decrease in particle diameter increases the Young's modulus, especially below 15 nm. Aggregate size was not seen to have any effect on the Young's modulus, for the range of aggregate sizes considered. The results of these studies can be used to optimize the mechanical properties of titania films, made up of nanoparticle aggregates, for different desired applications.

SYNTHESIS OF POROUS FILMS FROM NANOPARTICLE AGGREGATES  
AND  
STUDY OF THEIR PROCESSING-STRUCTURE-PROPERTY RELATIONSHIPS

by

Oluwatosin A. Ogunsola

Dissertation submitted to the Faculty of the Graduate School of the  
University of Maryland, College Park in partial fulfillment  
of the requirements for the degree of  
Doctor of Philosophy  
2005

Advisory Committee:

Professor Ehrman, Dept. of Chemical and Biomolecular Engineering, Chair  
Professor Dasgupta, Dept. of Mechanical Engineering, Dean's representative  
Professor Raghavan, Dept. of Chemical and Biomolecular Engineering  
Professor Kofinas, Dept. of Chemical and Biomolecular Engineering  
Professor Salamanca-Riba, Dept. of Materials Science and Engineering

©Copyright by  
Oluwatosin A. Ogunsola  
2005

## ACKNOWLEDGEMENTS

This work is dedicated to my big daddy “GOD”, without whom I would not have started on this path, not to talk of finishing it.

First and foremost, I would like to thank my family for their unwavering support and belief in me. A special thanks goes to the females for helping me out of financial, emotional, physical and spiritual pits that I got into. A big thank you to my dad who always told me I was special.

Thanks to Ebele for being there for me always, you are a true friend indeed. To all my friends and special cousins, you know who you are, thank you for your support and prayers.

We have a saying where I come from, that it takes a whole village to raise a child. Indeed, it took literally a whole village of people to get me to this point. I would like to acknowledge all the people who taught me how to use various instruments or programs and who assisted me in taking measurements. A big thanks to Inuka, Dr. Gbenga Famodu, Dr. Tim Zhang, Prof. Doug English, Andrew, Dr. Peter Zavalji, Dr. Fettinger, Ashish, Lucy and Ehrman group. To my wonderful assistants, Jason and Osifo, may the good Lord bless you both. Thanks to Bernie and Jack for making it possible to continue with my experiments. Thanks to Dr. Jinwon Park and Prof. Gil Lee for taking mechanical properties measurements of some parts of this work. To all who allowed me the use of their various instruments, thank you.

Thanks to my Dissertation Committee for their service and for answering all my questions in all their various classes I took over the years. Most of all, I would

like to thank Dr. Sheryl Ehrman for not only taking a chance on me, but being more than an advisor to me. The care, advice, career talks and general talks mean more to me than you would ever know. Thank you very much from the bottom of my heart.

To all those who I did not mention by name, believe me, I am grateful for all your support and I thank you.

Lastly, I just want to thank the one who made it possible for me to get to this point. I faced so many challenges on the way here, and at times I thought it would be impossible to finish. *Just when I am about to give up, he carries me and strengthens me to go on.* Thank you GOD for being my staunchest supporter and helper. I love you.

## TABLE OF CONTENTS

List of Tables .....	vii
List of Figures .....	viii
Chapter 1: Introduction .....	1
1.1 Nanoparticle Processing	1
1.2 Overview of Dissertation	2
Chapter 2: Background .....	3
2.1 Overview of Titania Films	3
2.2 Aerosol Film Processing	7
2.3 Characterization Overview	8
2.4 Overview of Simulation Methods	11
Chapter 3: Effect of Structure on Mechanical Properties: Experimental Study .....	13
3.1 Abstract	13
3.2 Introduction	14
3.3 Experimental	19
3.3.1 Process Description	19
3.3.2 Apparatus	19
3.3.3 Experimental Procedure	21
3.4 Characterization Methods	23
3.4.1 Physical and Chemical Characterization	23
3.4.2 Mechanical Characterization	24
3.5 Results and Discussion	27

3.6 Summary	42
Chapter 4: Effect of Annealing on Mechanical Properties .....	43
4.1 Abstract	43
4.2 Introduction	44
4.3 Experimental	45
4.3.1 Experimental Procedure	45
4.4 Characterization Methods	48
4.4.1 Physical and Chemical Characterization	48
4.4.2 Mechanical Characterization	49
4.5 Results and Discussion	52
4.6 Summary	66
Chapter 5: Effect of Structure on Mechanical Properties: Simulation Study .....	68
5.1 Abstract	68
5.2 Introduction	69
5.3 Deposit Simulation	72
5.3.1 Aggregate Simulation	72
5.3.2 Final Deposit Simulation	73
5.4 Continuum Finite Element Analysis	75
5.5 Results and Discussion	80
5.6 Summary	85
Chapter 6: Conclusions and Recommendations for Future Work .....	86
6.1 Conclusions	86
6.2 Recommendations for Future Work	89

Appendices.....	90
A. Supplementary Experimental Information	90
B. Procedures for Characterization	95
C. Supplementary Computational Information	104
References.....	137

## LIST OF TABLES

**Table 2.1.** Comparative costs and efficiencies of power generators.

**Table 3.1.** Coalescence and collision times in reactor.

**Table 4.1.** Average value of Young's modulus and hardness for each film. The error represents standard deviation of three measurements.

**Table 5.1.** Parameter values used in simulations.

## LIST OF FIGURES

**Fig. 3.1.** Aerosol processes in the experimental apparatus. After particle formation via (a) condensation, (b) collision between these particles may occur. After collision, some particles may join to form larger particles via (c) coalescence. These larger particles may form single particles or aggregates.

**Fig. 3.2.** Bond reaction to applied force, (a) before strain and (b) after strain.

**Fig. 3.3.** Overall schematic of the aerosol growth and film deposition process.

**Fig. 3.4.** Schematic illustrating indentation.

**Fig. 3.5.** Collection location points inside quartz tube (not to scale). Zone 4, 3, 2 and 1 are 57, 77, 87 and 99 cm in from entrance (left) into the quartz tube.

**Fig. 3.6.** Temperature profile inside quartz tube. The legend indicates the location of the deposition stage.

**Fig. 3.7.** X-Ray diffraction spectra of films collected at different locations.

**Fig. 3.8.** Transmission electron microscope images of films collected at different locations. The legend indicates the position of the deposition stage. 57 cm corresponds to the shortest residence time and 99 cm corresponds to the longest residence time.

**Fig. 3.9.** Aggregate size distribution at different locations. The legend indicates the position of the deposition stage.

**Fig. 3.10.** Illustration of primary particle and aggregate morphology.

**Fig. 3.11.** Aggregate size distribution in quartz tube at 77 cm from the quartz tube entrance.

**Fig. 3.12.** Typical load-indentation curve.

**Fig. 3.13.** Effect of primary particle diameter on Young's modulus. The error bars for primary particle diameter represents the standard deviation of the size distribution. The error bars for Young's modulus represent standard deviation of two to four measurements. In some cases, the standard deviations are smaller than the data point markers.

**Fig. 4.1.** Overall schematic of the aerosol growth and film deposition process.

**Fig. 4.2.** XRD spectra of a) the sample annealed at 1000 °C, b) the sample annealed at 800 °C, c) the sample annealed at 600 °C, d) the sample annealed at 400 °C and e) the unannealed sample. The notations A and R represent anatase and rutile crystalline phases respectively.

**Fig. 4.3.** Transmission electron microscope images of a) the unannealed sample, b) the sample annealed at 400 °C, c) the sample annealed at 600 °C, d) the sample annealed at 800 °C and e) the sample annealed at 1000 °C.

**Fig. 4.4.** Effect of annealing temperature on primary particle and aggregate sizes. Error bars represent measurement uncertainty. In some cases, the error bars are smaller than the data point markers.

**Fig. 4.5.** Change in specific surface area and film porosity with annealing treatment. Error bars represent measurement uncertainty. In some cases, the error bars are smaller than the data point markers.

**Fig. 4.6.** Atomic force microscope indentation measurements on the porous films annealed at 1000 °C. Load - indenter displacement behavior for a 70 N/m cantilever at a maximum load of 3.9  $\mu$ N.

**Fig. 4.7.** Young's modulus and hardness of the titania film as a function of annealing temperature. Error bars represent standard deviation of three measurements.

**Fig. 5.1.** Equivalent-continuum model representation of the nanoparticulate film.

**Fig. 5.2.** Bond distribution in the nanoparticulate film.

**Fig. 5.3.** Growth of nanoparticle deposit obtained from simulations. F1, F2 and F3 represent x, y and z axis respectively.

**Fig. 5.4.** Influence of primary particle size on Young's modulus.

**Fig. 5.5.** Influence of aggregate size on Young's modulus.

**Fig. 5.6.** Influence of porosity on Young's modulus.

## **CHAPTER 1: INTRODUCTION**

### **1.1 Nanoparticle Processing**

A nanoparticle is defined as a particle 100 nanometers or less in diameter. Nanoparticles are of interest because of their emerging useful optical, catalytic, mechanical, and magnetic properties that are different from those of the bulk material. Nanoparticles are made top down from bulk (mechanical attrition) and the bottom up from molecules (chemical synthesis in both gas and liquid phases). Wet phase approaches include sol gel methods, hydrothermal synthesis, solvothermal synthesis, and reduction in solution processes. Gas phase approaches include spray pyrolysis, plasma, flame, furnace, and laser synthesis. Every method or process has its advantages and disadvantages. Nanoparticles are synthesized in the gas phase by reaction of precursor gases (gas-to-particle conversion) or by evaporation and/or reaction of precursor droplets (particle-to-particle conversion). The gas-to-particle conversion method was used in this work.

## **1.2 Overview of Dissertation**

The focus of this work is to determine the relationship between the structure of porous titania films (made up of nanoparticle aggregates produced via a gas phase method) and their mechanical properties. To that effect, a detailed background of the applications and processing routes of titania films is shown in Chapter 2. The various characterization methods used in this work are presented also, along with a basic introduction into computer simulation methods in Chapter 2. In Chapter 3, the effects of reactor residence time on film structure and mechanical properties are described. Post-processing effects on the synthesized titania films via annealing are shown in Chapter 4. The films were simulated computationally and the mechanical properties of film structures beyond what could be generated experimentally were studied. The computational study of structure-mechanical property relationships is presented in Chapter 5. Finally, Chapter 6 is a summary of the work presented and includes recommendations for future research.

## CHAPTER 2: BACKGROUND

### 2.1 Overview of Titania Films

Porous films made from titania nanoparticle aggregates have a variety of uses in high surface area applications such as gas sensors,<sup>1; 2</sup> photocatalysts in treatment of wastewater<sup>3</sup> and air pollutants,<sup>4; 5</sup> optical filters,<sup>6</sup> and photovoltaic electrodes for lithium batteries<sup>7</sup> and low cost solar cells.<sup>8</sup> Generally, films are processed via different routes such as sol-gel dip/spin coating,<sup>3</sup> chemical vapor deposition (CVD),<sup>9</sup> modified CVD (MCVD) and particle precipitation aided CVD (PPCVD),<sup>10</sup> magnetron sputtering,<sup>11</sup> plasma electrolytic oxidation,<sup>12</sup> electrochemical oxidation,<sup>13</sup> chemical vapor synthesis,<sup>14</sup> and ion-beam deposition.<sup>15</sup> Different microstructures and deposit morphologies are generated from the various processing routes mentioned above.

The use of solar cells to convert solar energy to electricity is of major interest especially in third world countries. There is a critical need to make solar cells that will generate power at a reasonable cost, for the solar cells to compete with other forms of power generation. Table 2.1 compares production costs and efficiencies of different forms of power generators as compiled by Nuclear Energy Institute (NEI).

**Table 2.1.** Comparative costs and efficiencies of power generators.

<b>POWER GENERATOR</b>	<b>COST (cents/ kWh)</b>	<b>EFFICIENCY</b>
Solar cell	2.5	25 %
Wind	0.2	25 %
Hydro	0.5	Not Available
Nuclear	1.7	90 %
Coal	1.9	70 %
Petroleum	5.4	Not Available
Natural gas	5.9	14 – 50 %

<http://www.nei.org/>

Grätzel solar cells, also known as dye-sensitized solar cells (DSC), use relatively cheaper materials compared to other available solar cells. A Grätzel solar cell includes a wide band gap semiconductor oxide (titania nanoparticles) placed in contact with an electrolyte. Adsorbed on the surface of the titania nanocrystalline film are the organic dye molecules. Two conducting electrodes and a sensitizer complete the cell arrangement. The nanocrystalline film morphology, the solar cell stability, the choice of the sensitizer, dye and electrolyte are important as described by Grätzel<sup>16</sup> and others in the literature.<sup>17-19</sup> There has been extensive research into the study of the materials used, with the motivation of improving the efficiency of the Grätzel solar cell. As mentioned earlier, one of the materials is a layer of nanostructured titanium

dioxide (titania). There have been a number of experimental and simulation studies on the influence of titania film morphology on photocatalytic activity. For example, studies of microstructural changes of titania films with heat treatment revealed that crystallinity, specific surface area and photocatalytic properties of the titania films, changed with increasing calcining temperature.<sup>20; 21</sup> Titania films sintered via heat were shown to have a more homogeneous morphology and higher electrical density than pressure sintered titania films.<sup>18</sup> The result was attributed to the heat sintered films being well connected. Barbe et al.<sup>8</sup> showed that the microstructure (particle size, porosity) of the titania films influenced the photovoltaic response of the Grätzel solar cell. A study of titania nanoparticle size on electron diffusion by Nakade et al.<sup>17</sup> showed that the electron diffusion coefficient increased with increasing particle size. Hu et al.'s<sup>22</sup> experimental study of influence of particle coordination number in nanoporous titania films and the solar cell performance revealed that low and very high particle coordination numbers result in lower solar cell efficiency, and the presence of small pores slows down the diffusion of electrolyte. In simulations of the microstructure of nanoparticle films, with emphasis on titania films for solar cells, Lagemaat et al.<sup>23</sup> showed that increasing the porosity of the film decreases the coordination number of each particle. In a related study, the particle connectivity was also shown to influence electron transport in solar cells.<sup>24</sup> The results from the study done by Benkstein et al.<sup>25</sup> on dye sensitized titania solar cells agree with the results presented by Lagemaat et al.<sup>23</sup> that the coordination number decreases with an increase in porosity; furthermore, they show that the average number of particles in contact with electrons increases with increasing porosity. Kulkarni and Biswas<sup>26</sup>

used a Brownian dynamics simulation approach to predict morphology of nanoparticle deposits in the presence of interparticle interactions, with the motivation that the deposit morphology and microstructure affected the efficiency of the solar cell. The simulations revealed that van der Waals and Coulombic interactions influence the morphologies of the nanoparticle deposits.

In all the above-mentioned studies of titania films, the focus is mainly on how the film morphology affects their photocatalytic properties. Studies have shown that particle coordination number, surface area, particle size, particle connectivity and film porosity all affect electron and electrolyte transport within the solar cell. It is reasonable to assume that these same parameters will affect the mechanical properties of the films and efficiency of the solar cells. With the increasing number of applications for titania nanostructured films, it will be essential to have an understanding and control of the mechanical properties of these titania films. The mechanical properties of the films can then be optimized for different desired applications. It is important to realize that properties change when the material is nanostructured and assuming the mechanical property values of the bulk for the nanostructured material will lead to gross mistakes. The mechanical properties of nanoparticle based materials have been shown in a few studies to be different from those of bulk solid materials. Friedlander et al.<sup>27</sup> characterized the nanomechanical properties of graphitic nanoparticle chain aggregates by AFM and found the Young's modulus value for single chain aggregates to be in the range of 3.0 to 8.8 MPa with the bulk value for graphite ranging between of 2.1 to 18.6 GPa. Studies of nanoindentation on aluminum oxide nanoparticulate films by Bonilla and Lee<sup>28</sup> also

show the films having a Young's modulus in the range 0.4 to 1 MPa with the bulk value in the range of 390 GPa. In all cases, the experimentally determined Young's modulus values were orders of magnitude less than bulk values. However, there are no reports in the literature on the mechanical properties of titania films made up of nanoparticle aggregates generated in the gas phase.

The understanding of the relationship between the film structures, as generated by a particular processing route, and the resulting mechanical properties is the basis of this work. The change in film structure and mechanical properties with post processing is also studied. A combination of simulation methods is also used to study parameters of the film for an increased understanding of structure-mechanical property relationships.

## **2.2 Aerosol Film Processing**

Films processed via aerosol routes include droplet, vapor and solid particle deposition. Droplet deposition (spray pyrolysis)<sup>29</sup> involves deposition of droplets containing reactants onto a substrate where they evaporate and react to form a film. In aerosol-assisted chemical vapor deposition,<sup>30</sup> the solution containing the reactants is brought close to the substrate where it evaporates and further reacts on the substrate. Plasma-enhanced chemical vapor deposition<sup>31</sup> and laser-enhanced chemical vapor deposition<sup>32</sup> involve the use of plasma and laser close to the substrate. Electrostatic and inertial particle deposition take place by inertia and electrophoresis.<sup>33</sup> Particle-

precipitated chemical vapor deposition<sup>10; 34</sup> involves forming solid particles in a CVD system and depositing the particles with or without vapor onto a substrate, with further reaction occurring or not at the substrate.

### **2.3 Characterization Overview**

In this work, as-synthesized and post processed films were characterized via different techniques to understand the chemical, physical and mechanical behavior of the films.

Fourier transform infrared spectroscopy (FTIR) is an analytical technique that measures the absorption of various infrared light wavelengths by a material.<sup>35</sup> When a material is subjected to infrared light, it causes molecular bond vibration. The absorption of infrared light is possible when the frequency of the infrared light and the molecular vibration are the same. The absorption band values are fingerprints for materials as documented in reference libraries.<sup>36</sup> FTIR (Nicolet 550 Series II) was used to determine the presence of absorption bands characteristic to the material synthesized.

X-ray diffraction (XRD) is a technique in which a material is subjected to X-rays to obtain crystallinity information.<sup>37</sup> The Bragg angle in the XRD spectrum is the angle at which an incident x-ray wave makes with the plane that diffracts it. The peak

at each Bragg angle corresponds to the plane from which the x-ray is diffracted. These planes give characteristic information about the shape and size of the crystal's unit cell. XRD (Bruker D8 Diffractometer) was used to determine the crystalline phase of the as-synthesized and post processed films.

In electron microscopy, high voltage electron beams are focused by electromagnetic lenses to produce images. Transmission electron microscopy (TEM) produces images from primary electrons that are transmitted through the material<sup>38</sup> and scanning electron microscopy (SEM) produces images from secondary electrons emitted from the surface due to the excitation by the primary electrons.<sup>39</sup> TEM (Hitachi 600AB) was used in this work in the determination of average particle size, while SEM (JEOL SEM 5400) was used to estimate the thickness of as-synthesized and post processed films.

The Brunauer-Emmett-Teller (BET) method (Quantachrome Nova 1200) was employed in this work to measure specific surface area of the films. The amount of material adsorbed on a sample is plotted as a function of pressure at a fixed temperature to generate an adsorption isotherm.<sup>40</sup> From the isotherm, the total surface area and specific surface area of the sample is calculated.

Dynamic light scattering (DLS; Photocor-FC) was used in some parts of this work to measure average aggregate size. When a beam of light passes through a colloidal solution, some light is scattered by particles in the solution.<sup>41</sup> A detector

observes time dependent fluctuations of the intensity of the scattered light resulting from Brownian motion of the particles. Analysis of the intensity fluctuations gives the diffusion coefficient from which the hydrodynamic radius of the particle can be calculated using the Stokes Einstein equation.

The differential mobility analyzer (DMA; TSI Model 3081) separates particles based on their electrical mobility. The DMA is made up of two concentric cylinders, inlet exit and outlet exit. Voltage is applied to the inner cylinder to create an electric field. A small stream of the generated particles is electrically charged before entrance into the DMA by ions from a radioactive Po-208 source. A narrow range of the particles is then selected by their electrical mobility by varying the voltage applied to the inner cylinder. The diameter of the particles selected is calculated from the electrical mobility. Particles of a given electrical mobility would be of the same equivalent size if they have the same charge. The selected range passes through the outlet exit to the condensation particle counter (CPC; TSI Model 3022A). The CPC counts the particles by condensing water or alcohol on the particles to make them large enough to be scattered by light.<sup>41</sup> A detector in the CPC detects and counts the number of times a beam of light is scattered. This number gives the concentration of the particles in the selected range from the DMA. This is done repeatedly until a large range of particle size is covered, thereby getting the size distribution of the generated particles. The DMA and CPC were used in this work to measure the size distributions of deposited aggregates in the synthesized films.

The Young's modulus and hardness of films in this work were determined using an atomic force microscopy (AFM; Asylum Research 3-D Molecular Force Probe) indentation technique. AFM can measure the vertical cantilever deflection with applied force.<sup>42</sup> The mechanical properties are determined from the force-indentation depth measurements.

## **2.4 Overview of Simulation Methods**

Generally, simulation methods for properties of materials include computational chemistry and computational mechanics. The length and time scales at which they operate differentiate them. Computational chemistry simulations operate on the smaller scale ( $10^{-10}$  m) while computational mechanics operates on a larger scale ( $10^0$  m). The computational chemistry methods are based on the assumption of the presence of discrete molecular structures of matter while the computational mechanics methods typically require the assumption of a continuous material structure. Each simulation method is further subdivided into quantum mechanics and nanomechanics for computational chemistry, and micromechanics and structural mechanics for computational mechanics. The molecular based methods include<sup>43</sup> ab initio, Monte Carlo, molecular mechanics and molecular dynamics methods. Finite element method (FEM), boundary element method (BEM), Eshelby, Halphin-Tsai and rule-of-mixtures methods are examples of continuum based methods.<sup>43</sup> A

combination of computational chemistry and mechanics can be also used and this is called multiscale modeling.

In molecular dynamics simulations, Newton's equations are used to simulate motion in a system of particles. This method allows for the study of reaction paths, but its main disadvantage is the high computational cost involved. In molecular mechanics, molecules are represented as spheres connected by springs, allowing systems to be represented by classical physics and simple potential energy functions. The presence of electrons is ignored, which enables larger systems to be studied; however, it is difficult to follow reaction paths with this method. The ab initio methods are based on solving Schrödinger's equation for each electron. Ab initio methods are generally accurate. Because of the high computation cost involved, they can only be used for small systems of atoms. Monte Carlo methods can be generally described as statistical or stochastic simulation methods, as they use a sequence of random numbers and probabilities to perform the simulations. Micromechanics methods are used to study the properties of composite materials by averaging properties of the individual constituents. FEM and BEM discretize the material into smaller elements for which stress and strain values are determined. FEM involves elements throughout the volume while BEM uses elements only along the boundary.

## **CHAPTER 3: EFFECT OF STRUCTURE ON MECHANICAL PROPERTIES- EXPERIMENTAL STUDY**

### **3.1 Abstract**

The morphology, defined as size and shape, of nanoparticle aggregates synthesized in gas phase can be varied via reactor temperature, particle residence time and flow rate into the reactor. In this work, the residence time of particles in the furnace was varied. The influence of the above-mentioned variation on primary particle size, aggregate size and Young's modulus of titania nanoparticle deposits was investigated. The results show that a decrease in the primary particle diameter results in an increase in the Young's modulus.

## 3.2 Introduction

Nanoparticle based films of gold, diamond, iron oxide, alumina, platinum, titanium nitride and titania have been synthesized via various routes as reported in the literature.<sup>10; 14; 34; 44-48</sup> In this work, nanoparticle based films of titania were synthesized via a gas phase method.

Particles are synthesized in the gas phase by reaction of precursor gases (gas-to-particle conversion) or by evaporation and/or reaction of precursor droplets (particle-to-particle conversion).<sup>49</sup> Both paths are used in making a variety of particles. In this work, gas-to-particle conversion is used. The precursor vapor reacts to form condensable product species. The presence of condensable species in the gas phase causes the system to be in a non-equilibrium supersaturated state; the system then tries to achieve equilibrium by generation of new particles (homogeneous nucleation) or condensation on existing particles (heterogeneous condensation).<sup>50</sup> The particles then grow by collision and coalescence, via viscous flow for liquid phase particles or solid-state diffusion for solid phase particles, as shown in Fig. 3.1.

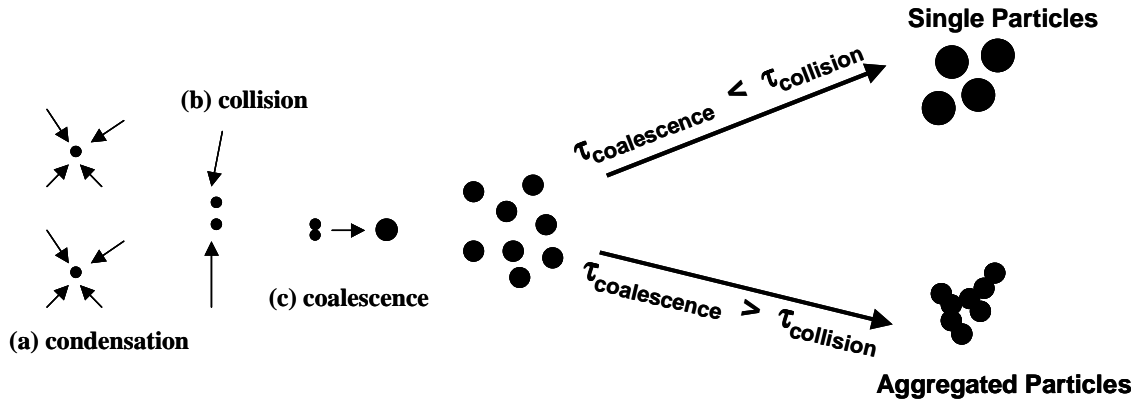


**Fig. 3.1.** Aerosol processes in the experimental apparatus. After particle formation via (a) condensation, (b) collision between these particles may occur. After collision, some particles may join to form larger particles via (c) coalescence. These larger particles may form single particles or aggregates.

If collisions occur faster than the particles sinter, in other words, if the time between collisions ( $\tau_{collision}$ ) is shorter than the time required for the particles to coalesce ( $\tau_{coalescence}$ ), aggregated particles are formed. The partially sintered particles have chemical bonds between them. However, if collisions occur slower than the particles sinter, single particles are formed as shown schematically in Fig. 3.1.

For the production of porous films, aggregated particles are advantageous as they lead to a highly porous microstructure. Generally, strong chemical bonds are found between primary particles (because they are partially sintered at high temperatures) and weak van der Waals forces exist between particles from different aggregates that collide together at low temperatures.<sup>50</sup> Porous films are then formed by the thermophoretic deposition of the particles onto the substrate that is maintained

at a lower temperature. Under mechanical stress, single titania (alumina and iron oxide) nanoparticle aggregates (with small primary particle size) have exhibited an elastic response.<sup>51</sup> The degree of fragmentation of nanoparticle aggregates were shown to decrease with primary particle size.<sup>52</sup> This implies that decreasing the particle size should increase the strength of films made from nanoparticle aggregates. Unpublished preliminary results<sup>28</sup> for indentation of alumina films composed of nanoparticle aggregates suggest the films are relatively fragile. The alumina films were of low strength and so offered little resistance to applied load. The films exhibited an elastic response upon consolidation.

However, there is nothing yet reported in the literature about the mechanical behavior of a large number of titania nanostructured aggregates in physical contact with each other. With the increasing wide application of porous films made from aggregates, much needs to be understood about the mechanical properties. The weak van der Waals bonds found in a film comprised of aggregates deform (Fig. 3.2) with applied force or strain, while the strong chemical bonds do not.

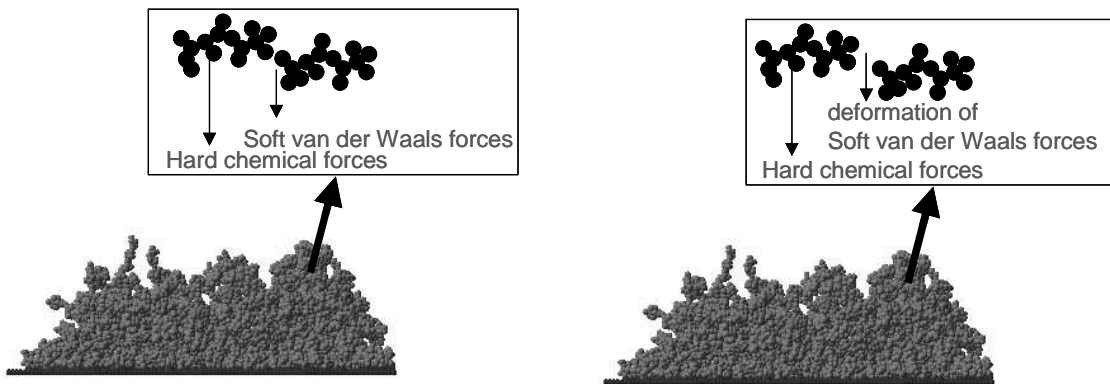


**Fig. 3.2.** Bond reaction to applied force, (a) before strain and (b) after strain.

Fig. 3.2 shows how the strong chemical bonds act as a resistance to the contraction and expansion of the van der Waals bonds. A basic understanding of the above-described mechanism will lead to being able to engineer strong titania films that will not collapse in their end use. Also, it might be possible to change the elastic limit of the film as needed. Engineering of the films will occur by varying the amount of chemical and van der Waals bonds. To that end, depositing different sized aggregates and variation of particle size can influence the mechanical properties of the film by changing the amount of chemical and van der Waals bonds. The particle and aggregate size changes can be achieved by varying the temperature, precursor vapor flow rate and the residence time of particles in the reactor. Variation of the above-mentioned parameters has been shown to influence the ratio of characteristic times of collision and coalescence, leading either to unaggregated particles, or to soft or hard aggregates of different particle sizes.<sup>53; 54</sup> The change in residence time of particles has also been shown to influence the lattice structure of anatase titania nanoparticles.<sup>55</sup>

Variation of temperature, precursor vapor flow rate and particle residence time in the reactor is known to influence the particle and aggregate sizes<sup>53-57</sup>. They can be used as tools to tune the particle and aggregate size of material synthesized. Temperature was not chosen because at lower temperatures the titania synthesized is generally amorphous and as our interest in the study was from the use of crystalline titania in photocatalytic and solar cell applications, it was logical not to synthesize amorphous titania. Precursor vapor flow rate was also not chosen as a tool because we wanted to synthesize very thick films (because of AFM indentation requirements)

and reducing the precursor flow rate would have greatly increased collection times required to make thick films. Instead, the amount of time the particles spend in the reactor before collection was varied in this study. It is postulated that collecting the titania film earlier in the reactor should yield structurally different films than those collected at the end of the reactor. The difference in structures of the film consists of variation in the primary particle size, aggregate size and porosity. The structural differences will have an impact on the mechanical properties of the films.

A differential mobility analyzer (DMA, TSI Model 3081) and condensation particle counter (CPC, TSI Model 3022A) combination was introduced into the experimental set up, via a sample probe inside the reactor, to obtain the size distribution of the aggregated particles as a function of residence time at a set furnace temperature. An explanation of how the DMA and CPC combination works is given in Appendix B. The average primary particle size was obtained from TEM images. The primary particle and aggregate size distributions illuminate how the microstructure of the porous titania film evolves with residence time in the reactor.

### **3.3 Experimental**

#### **3.3.1 Process Description**

In this work, a hybrid process based upon gas-to-particle conversion and particle precipitated chemical vapor deposition (PPCVD) is used for the production of titania nanoparticulate films. Here, gas-to-particle conversion involves the titanium isopropoxide precursor vapor reacting to form titania particles in the gas phase. The generated particles are then collected as a film by PPCVD. In PPCVD, the particles are formed at an elevated temperature and deposited on a cooled substrate by thermophoresis. This hybrid process offers the advantages of single-stage, atmospheric, solvent free, and low substrate temperature operation, enabling deposition onto materials (such as polymeric membranes, microelectronics) for which thermal degradation is a limiting factor. This hybrid process has been used to make nanoparticulate films of a variety of materials including titanium nitride,<sup>10</sup> alumina,<sup>34</sup> and platinum/alumina.<sup>58</sup> Here, we extend this process to the formation of titania films.

#### **3.3.2 Apparatus**

The reaction chamber is a quartz tube (National scientific; ID 47 mm, OD 50 mm, 43 inches in length) that is vertically mounted within a three-zone furnace (Lindberg 54747-V Tube Furnace). Within the quartz tube, film deposition occurs by thermophoresis onto a substrate placed on an adjustable, vertical water-cooled stage with the cooling water maintained at 15 °C. The maximum stage surface temperature was measured to be 120 °C at a furnace temperature of 1000 °C and with the stage in

the lower heating zone.<sup>58</sup> A gas-drying unit (Drierite) is used to remove any moisture from the carrier gas before it comes in contact with the precursor, which is moisture sensitive. Liquid titanium tetra isopropoxide (98+ %, Acros Organics), TTIP, precursor is housed in a stainless steel bubbler (Strem Chemicals). The bubbler is a 150 ml electropolished stainless steel bubbler that can be placed horizontally in line with the gas-drying unit. It has a one-way valve (Swagelok) at the entrance to the bubbler to prevent back flow into the gas-drying unit. To prevent precursor condensation before entrance into the main reactor chamber, the feed lines into the reactor chamber are also heated. The feed line temperatures are independently controlled by mechanical relay and solid-state temperature controllers (OMEGA). The carrier gas (argon, 99.99%, Air Products) and oxygen (99.99%, Air Products) gas flows are controlled by rotameters (Cole-Parmer). The substrate used to collect the particles is a polished square shaped silicon wafer (475-575  $\mu\text{m}$  in thickness, cut to 2 cm x 2 cm, Silicon Quest International). The water temperature of the water-cooled stage is monitored by a thermocouple located at the inlet of the cooling stage; constant temperature is maintained by a chiller (NESLAB Model RBC-3). A stainless steel sample probe (ID 4.5 mm, OD 6mm, 60 inches in length) is vertically inserted into the quartz tube. The sample probe is connected to the DMA (TSI Model 3081). The monodisperse stream outlet of the DMA is connected to the CPC (TSI Model 3022A) and its excess stream outlet is connected to a vacuum pump (United Vacuum Model E2M2). During operation, particulate matter and gas species are removed from the exhaust stream by a liquid nitrogen cold trap (MDC Vacuum). The venting system for the process also includes a pump (Pfeiffer Vacuum) and braided hose assembly

(McMaster-Carr). For safety, a Lexan box (1/4 in thickness) surrounds the reactor to provide physical shielding and an enclosed environment for improved ventilation. An overall schematic of the aerosol reactor is illustrated in Fig. 3.3.

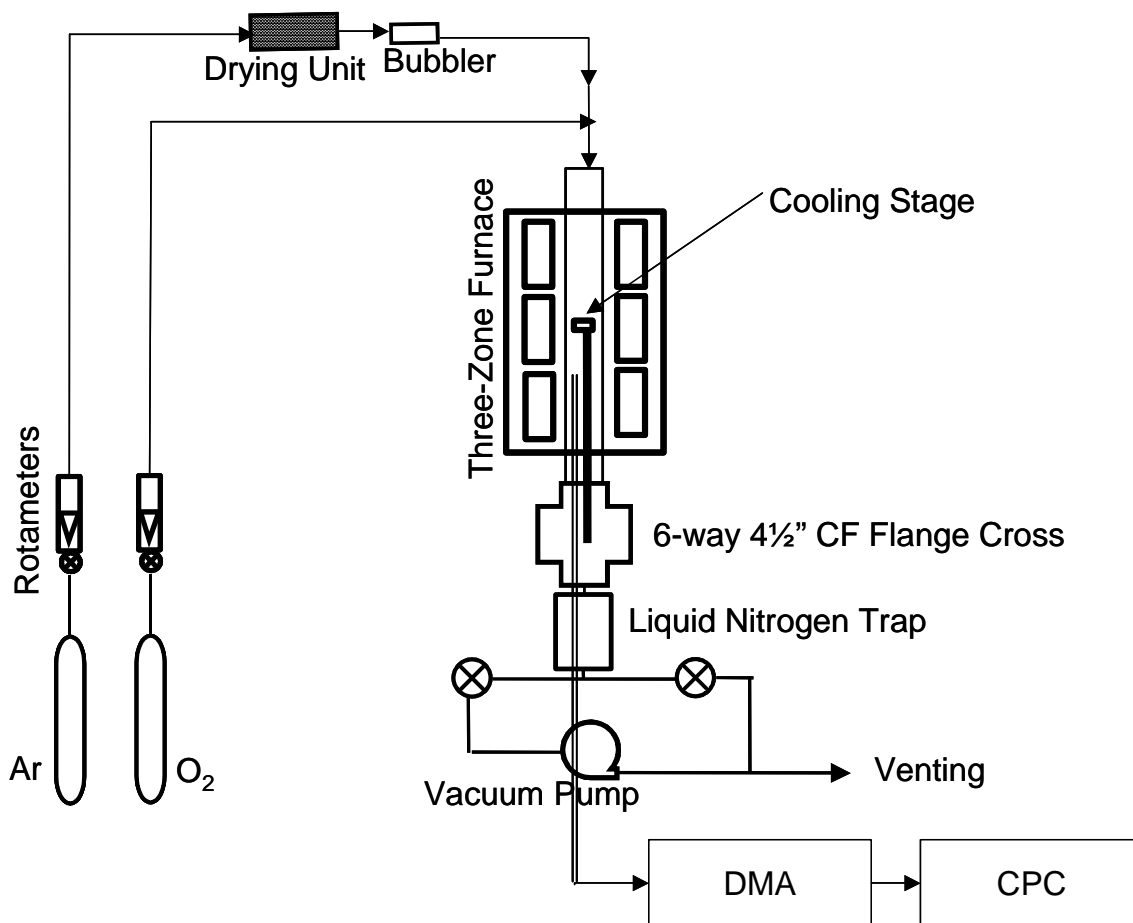


**Fig. 3.3.** Overall schematic of the aerosol growth and film deposition process.

### 3.3.3 Experimental Procedure

The preweighed silicon substrate is placed on top of the cooling stage. The furnace is preheated for four hours to obtain the desired furnace processing temperature. In these experiments, the three zones of the furnace were set to a chosen temperature. The cooling stage water temperature was maintained at 0 °C for 4.5

hours during furnace preheating and 15 °C during the film deposition. The bubbler was heated to 54 °C to increase the vapor pressure of the TTIP. The feed lines going into the reactor chamber were heated to 150 °C to prevent condensation of the TTIP vapor. Oxygen was allowed to flow in at 900 sccm (standard cubic centimeters per minute). Argon, the carrier gas, was fed into the gas-drying unit at 400 sccm. The TTIP vapor is bubbled out at  $1.3 \times 10^{-5}$  moles/min by opening the exit and entrance valves of the bubbler. The processing time is defined as the amount of time in which the carrier gas was supplied to the bubbler. The reactor was allowed to cool, and the sample and substrate were removed and weighed. To obtain additional powder for characterization, powder that deposited on the cooling stage was scraped off and collected.

### 3.4 Characterization Methods

#### 3.4.1 Physical and Chemical Characterization

Transmission electron microscopy (TEM; Hitachi 600AB) was used to determine the size distribution of primary particles. Samples were prepared by pressing a carbon TEM grid to the collected powder and tapping to remove excess powder. The average size was determined by measuring the diameters of 50 primary particles. Measurements of aggregate size distribution were obtained using differential mobility analyzer (DMA; TSI model 3081) for an equivalent electrical mobility size selection and a condensation particle counter (CPC; TSI model 3022A) for particle counting. Scanning electron microscopy (SEM; JEOL SEM 5400) was used to measure the approximate thickness of films. The mass of the film was measured gravimetrically by weighing the wafer before and after film deposition. The density of the films was estimated from the measured area of the wafer, and measured thickness and mass of the films. The porosities of the films were calculated with the densities of the film ( $\rho_{film}$ ) and bulk solid ( $\rho_{solid}$ ) as shown in the equation below

$$Porosity = 1 - \frac{\rho_{film}}{\rho_{solid}} \times 100 \quad . \quad (1)$$

Titania production was confirmed with Fourier transform infrared spectroscopy (FTIR; Nicolet 550 Series II) on pellets consisting of a 1:200 mass ratio of titania to KBr.

### 3.4.2 Mechanical Characterization: AFM indentation

Indentation was conducted using a 3-D Molecular Force Probe AFM (Asylum Research, Santa Barbara, CA). Indentations were performed with an 8  $\mu\text{m}$  diameter borosilicate glass sphere (Duke Scientific) attached to silicon nitride cantilever (Veeco Instruments, Santa Barbara, CA). The spring constants for the silicon nitride cantilever was determined from the thermal frequency spectrum of the cantilever to be 0.02 N/m.<sup>59</sup>

The applied load and depth of penetration into the titania films were continuously monitored at a series of maximum loads, resulting in a set of displacement-deflection curves. A maximum force load of 10 nN was applied on the films with the cantilever. Indentation is made up of two components, namely plastic and elastic indentation. These components can be identified from analysis of the unload curve. If the unload curve is approximately identical to the load curve, the indentation includes only the elastic component. For an elastic half space, the depths of the elastic indentation ( $\delta$ ) into the films were determined using the relation

$$\delta = \Delta d - \Delta z , \quad (2)$$

where  $\Delta d$  is displacement of the porous film and  $\Delta z$  is the deflection of the borosilicate glass sphere attached to the cantilever as shown in Fig 3.4.

Before indentation

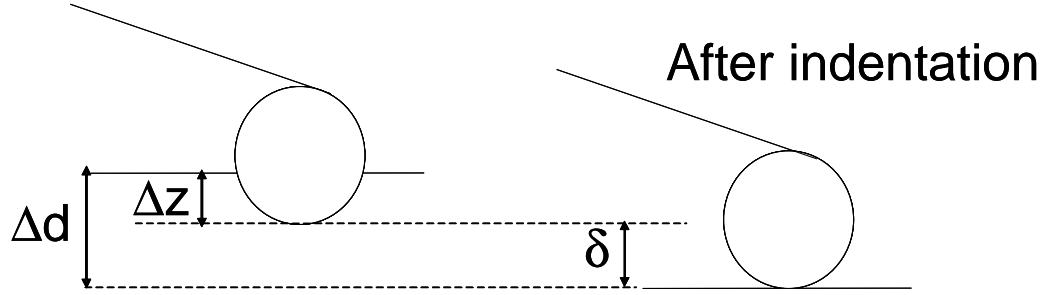


Fig. 3.4. Schematic illustrating indentation.

The unload curve was used to estimate the elastic modulus according to the following equation<sup>60</sup>

$$S = \frac{2}{\sqrt{\pi}} E^* \sqrt{A}. \quad (3)$$

Here,  $S$  is the measured stiffness of the upper portion of the unloading curve and where  $A$  is the projected area of the sphere contact on the film given by

$$A = 2\pi R \delta. \quad (4)$$

The reduced Young's modulus is given as

$$\frac{1}{E^*} = \left( \frac{1 - \nu_m^2}{E_m} \right) + \left( \frac{1 - \nu_i^2}{E_i} \right). \quad (5)$$

In which  $\nu_m$  and  $E_m$  are the Poisson's ratio and Young's modulus for the porous film respectively, and  $\nu_i$  and  $E_i$  are Poisson's ratio and Young's modulus for the material of the indenter, respectively. Since the glass sphere's Young's modulus, 103 GPa, is much larger than what was expected for the Young's modulus of the films, the value of  $E^*$  is dominated by the properties of the film and reduces to

$$\frac{1}{E^*} \approx \left( \frac{1 - \nu_m^2}{E_m} \right). \quad (6)$$

The Poisson's ratio of the films was not known. However, Arnold *et al* show that Poisson's ratio asymptotically approaches 0.5 as the porosity becomes close to 1.<sup>61</sup> The minimum porosity of all films including as synthesized and annealed was estimated to be 0.96. Therefore, the Young's modulus was calculated using 0.5 as a Poisson's ratio. Use of smaller values of the Poisson's ratio had a small effect on the measured mechanical properties of the films.

### 3.5 Results and Discussion

Fig. 3.5 is a schematic of the locations chosen for sampling in the quartz tube. The cooling stage was moved to chosen locations and the temperature inside the quartz tube was recorded at intervals of 7.6 cm. Overheating of the cooling stage prevented moving the sampling probe further up inside the furnace. The reactor temperature profile at the different collection locations was measured using a K type thermocouple as shown in Fig. 3.6. The profiles are typical of tube furnace reactor systems. As the cooling stage is moved up inside the quartz tube, the temperature decreases much faster, as shown on the right hand side of the temperature profiles.

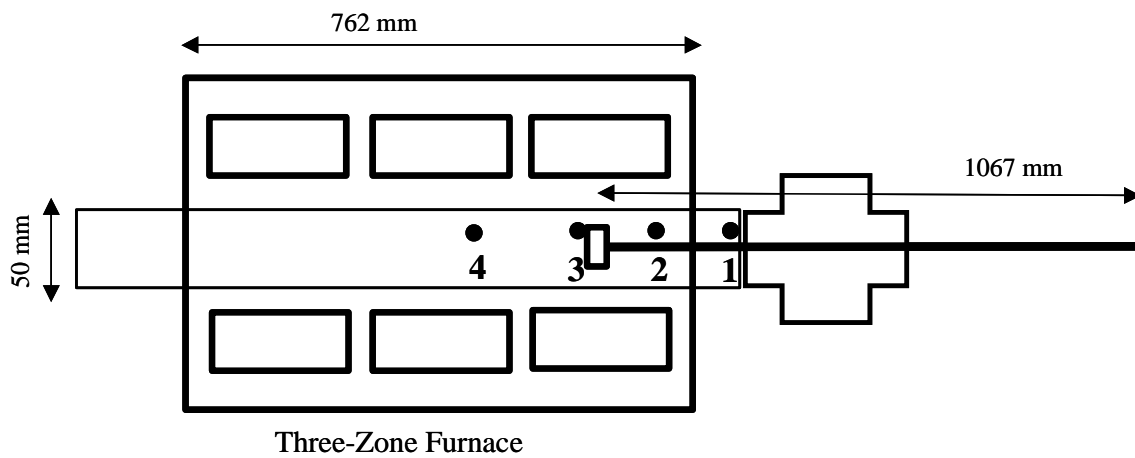


**Fig. 3.5.** Collection location points inside quartz tube (not to scale). Zone 4, 3, 2 and 1 are 57, 77, 87 and 99 cm in from entrance (left) into the quartz tube.

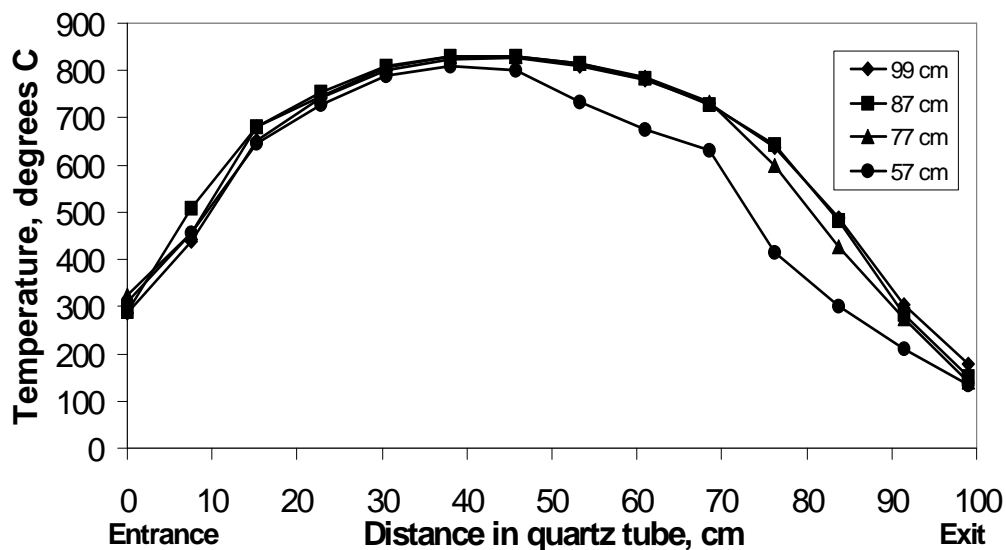


**Fig. 3.6.** Temperature profile inside quartz tube. The legend indicates the location of the deposition stage.

X-ray diffraction (XRD) analyses, of the synthesized films revealed the crystalline phases to be anatase, as shown in Fig. 3.7. Film collected at location/zone 1 is not shown as there was not enough sample to do XRD analysis. The XRD spectra of the films have the characteristic single peaks at d spacing values of 3.54, 2.37 and 1.89 Å with a characteristic double peak at 1.70 and 1.67 Å.<sup>62</sup> The diffraction pattern values and intensities are given in Appendix A.

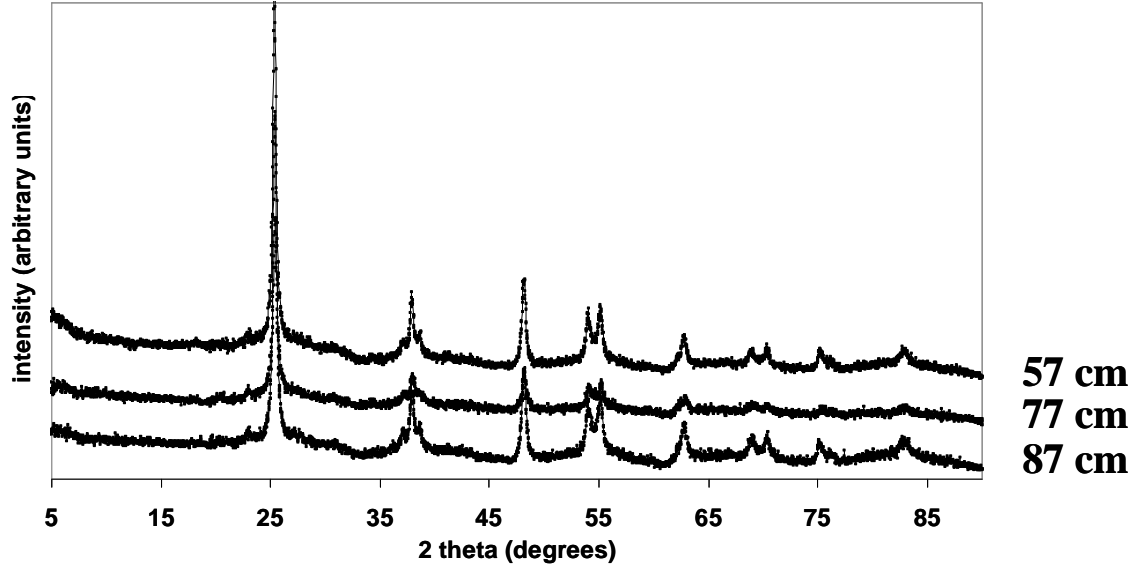


**Fig. 3.7.** X-Ray diffraction spectra of films collected at different locations. The legend indicates the position of the deposition stage.

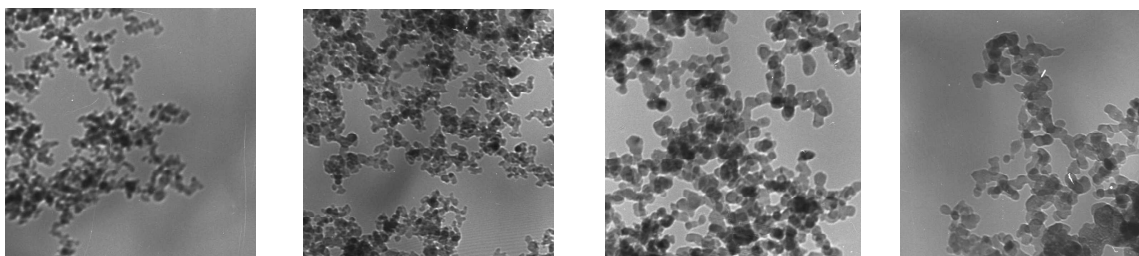
Primary particles form and grow in an unaggregated manner when  $\tau_{\text{coalescence}} < \tau_{\text{collision}}$ . Necking (solid state bonding) starts when  $\tau_{\text{coalescence}} > \tau_{\text{collision}}$ . Necking causes the particles to be aggregated. The aggregate is made up of small nanometer sized particles. Since the temperature is still high, the initial aggregates will start coalescing and form aggregates made up of larger nanoparticles. When  $\tau_{\text{coalescence}} \gg \tau_{\text{collision}}$ , coalescence is negligible and the aggregated particles collide on the substrate to form a porous film with weak van der Waals forces holding the particles between the aggregates together.

It is known that for a cooling temperature profile, coalescence time increases rapidly and then reduces, whereas collision time is slow to rise but keeps

increasing.<sup>50</sup> This is because coalescence time ( $\tau_{\text{coalescence}}$ ) depends inversely on the solid-state diffusion coefficient of the material and the particle volume. Initially the particle volume is very small and the diffusion coefficient is very small (at high temperature). The particle volume increases with time as the particles coalesce; the diffusion coefficients increase as temperature decreases. The time in between collisions ( $\tau_{\text{collision}}$ ) depends inversely on temperature and directly on particle size. As temperature decreases and particle size increase, the collision time increases. The time required for collisions and coalescence changes with particle and aggregate diameters, and in turn has an effect on the growth rate of primary particle and aggregate diameters.

Fig. 3.8 shows TEM images of titania nanoparticles collected at different zonal points. From the images, the average primary particle diameter was calculated. The average primary particle diameter is  $7.8 \pm 2.0$  nm at sampling location of 57 cm into quartz tube,  $6.9 \pm 1.7$  nm at 77 cm,  $15.9 \pm 1.9$  nm at 87 cm and  $14.7 \pm 2.7$  nm at 99 cm. At 57 and 77 cm into the quartz tube, the primary particle diameter is approximately half of the primary particle diameter at 87 and 99 cm into the quartz tube. It was expected that the primary particle diameter would increase as the particles spend more time in the reactor. Based on the temperature profile, the reactor temperature reaches a maximum at the midpoint of the furnace. The temperature starts to decrease at the location where the top of the cooling stage is positioned. When particles spend more time at a high temperature, they tend to coalesce and bigger primary particles are formed.

100 nm



**57 cm**

**77 cm**

**87 cm**

**99 cm**

**Fig. 3.8.** Transmission electron microscope images of films collected at different locations. The legend indicates the position of the deposition stage. 57 cm corresponds to the shortest residence time and 99 cm corresponds to the longest residence time.

The aggregate size distribution, at the different sampling locations, measured via the DMA and CPC is shown in Fig. 3.9. The particle count number of the sampling locations decreases slightly as you go down the quartz tube. However, the size distribution shows the same trend for all locations. The average aggregate diameter was calculated to be  $279 \pm 2$  nm for all the locations.

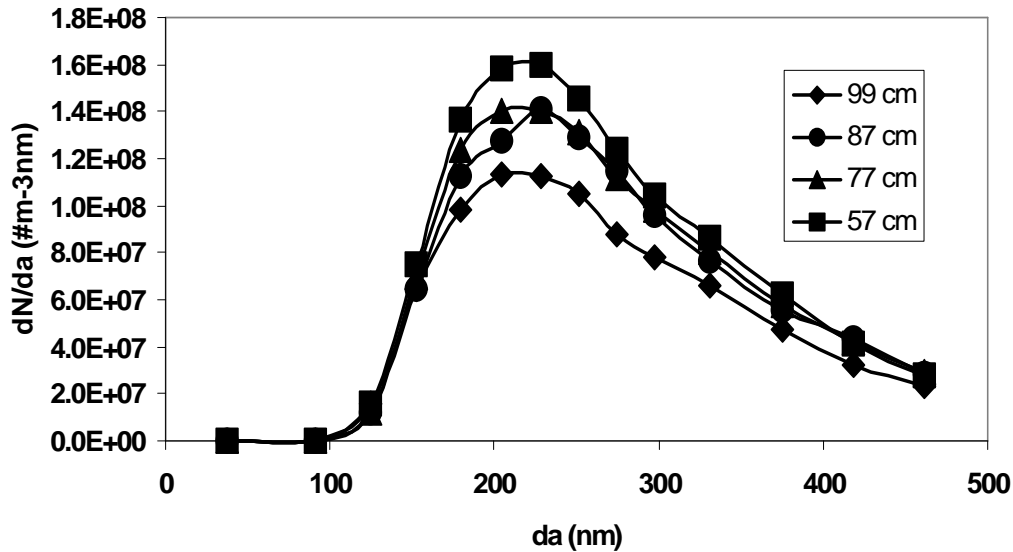


**Fig. 3.9.** Aggregate size distribution at different locations. The legend indicates the position of the deposition stage.

Though the primary particle diameter changed, the aggregate size distribution remained nearly constant at all locations. Using the definitions in DeCarlo<sup>63</sup> et al.'s paper,  $d_{me}$  is the mass equivalent diameter of a spherical particle of the same mass as the particle under consideration and  $d_{ve}$  is the volume equivalent diameter of a particle of the same volume as the particle under consideration. When the particles have no internal voids,  $d_{me}$  is equal to  $d_{ve}$ . The DMA measures the electrical mobility of a particle, defined as the diameter of a sphere with the same migration velocity in a constant electric field as the particle being measured. When two particles have the same migration velocity and same charge, it is to be assumed that they will have the same electrical mobility. Particles that have the same volume equivalent diameter and

if no internal voids will have the same mass equivalent diameter and migration velocity within the same ball park. The reason why the aggregate sizes do not change even when the primary particle size changes is proposed to be because the mass of the aggregate does not change. This is possible if the concentration of the aggregate is dilute and so very little collision occurs after the aggregates are initially formed as illustrated in Fig. 3.10.

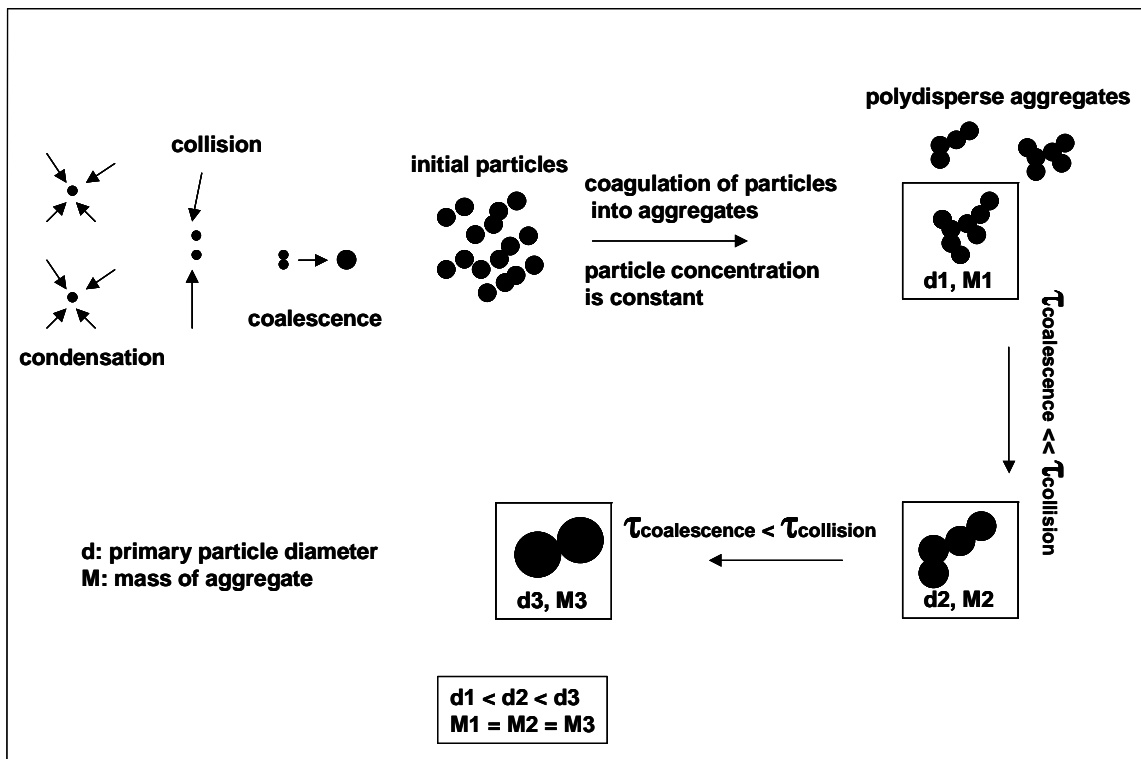


**Fig. 3.10.** Illustration of primary particle and aggregate morphology.

Time required for coalescence<sup>50; 64-66</sup> and collision<sup>50</sup> were calculated from equations 7 and 8, respectively. The primary particle diameter ( $d_p$ ) was used in the calculation of coalescence time and the time required for collision was calculated using the average aggregate diameter ( $d_a$ , electrical mobility diameter). The average aggregate diameter

was used in collision time calculation because it is the aggregates colliding and not the primary particles, while it is the primary particles that coalesce to form a bigger particle.

$$\tau_{\text{coalescence}} = 1500Td_p e^{\frac{34416}{T}} \quad (7)$$

$$\tau_{\text{collision}} = \frac{2}{\beta N} \quad (8)$$

Where  $\tau_{\text{coalescence}}$  is the time for two particles to coalesce via atomic diffusion,  $\tau_{\text{collision}}$  is the time for two particles to collide, T is particle temperature,  $d_p$  is primary particle diameter,  $\beta$  is the collision frequency function and N is the number of particles per unit volume of carrier gas.

The collision frequency function is given by<sup>67</sup>

$$\beta = 8\pi D d_a \left[ \frac{d_a}{d_a + \sqrt{2}g} + \frac{4\sqrt{2}D}{c d_a} \right]^{-1} \quad (9)$$

where  $d_a$  is the aggregate mobility diameter and the aggregate diffusion coefficient D, aggregate velocity c, and the transmission parameter g are calculated as<sup>67</sup>:

$$D = \frac{k_B T}{3\pi\mu_g d_a} \left[ \frac{5 + 4Kn + 6Kn^2 + 18Kn^3}{5 - Kn + (8 + \pi)Kn^2} \right] \quad (10)$$

$$c = \sqrt{\frac{8k_B T}{\pi\rho_a v_a}} \quad (11)$$

$$g = \frac{1}{3d_a \lambda_a} \left[ (d_a + \lambda_a)^3 - (d_a^2 + \lambda_a^2)^{\frac{3}{2}} \right] - d_a \quad (12)$$

where T is the aggregate temperature,  $k_B$  is the Boltzmann constant,  $\lambda_a$  is the gas viscosity,  $v_a$  is the aggregate volume,  $\rho_a$  is the aggregate density,  $\lambda_a$  is the mean free

path for the aggregates and Kn is the Knudsen number. The aggregate mean free path and Knudsen number are given as

$$Kn = \frac{2\lambda}{d_a} \quad (13)$$

$$\lambda_a = \frac{8D}{\pi c} \quad (14).$$

All parameters used in calculations are given in Appendix A.

The ratio of the collision time to the coalescence time was calculated using the measured temperature in the quartz tube at deposition location. The ratios are tabulated in Table 3.1. The ratio at 57 and 77 cm from the beginning of the quartz tube (zones 3 and 4) are much smaller than the ratios at 87 and 99 cm from the beginning of the quartz tube (zones 1 and 2). This means that after zones 3 and 4, coalescence between the particles will still occur at a much faster rate than collision is occurring between the aggregates. But by zones 1 and 2, coalescence will hardly occur anymore. Any collision that occur will not change the aggregate size as coalescence needed for solid state bonding between the particles of the colliding aggregates is impossible. The solid-state atomic diffusion coefficient (D) in the particles was calculated using<sup>68</sup>

$$D = A \exp\left(-\frac{B}{T}\right) \quad (15),$$

where T is temperature, A and B are material-dependent constants given as  $7.2 \times 10^{-6} \text{ m}^2/\text{s}$ <sup>66</sup> and  $34416 \text{ K}$ <sup>65</sup>, respectively. The diffusion coefficients (Table 3.1) at zones 3 and 4 are much larger than those of zones 1 and 2. This leads to further confirmation that the particles can grow after zones 3 and 4; but by zones 1 and 2, their growth is

practically impossible. This is reasonable as diffusion coefficient is a function of temperature and the temperatures at zones 1 and 2 are not as high as zones 3 and 4. As explained, after zones 3 and 4, the primary particle diameters will increase as the particles grow because of coalescing; the number of particles could change in each aggregate but the mass of each aggregate is preserved. Because the aggregates are of the same mass equivalent diameter and qualitatively similar fractal morphology, their electrical mobility diameters are measured to be the same.

**Table 3.1.** Coalescence and collision times in reactor.

<b>Zone #</b>	<b>Coalescence time (s)</b>	<b>Collision time (s)</b>	<b>Ratio of coalescence time to collision time</b>	<b>Diffusion Coefficient (m<sup>2</sup>/s)</b>
Zone 1	$3.449 \times 10^{15}$	$10.2 \times 10^5$	$3.38 \times 10^{10}$	$4.5 \times 10^{-39}$
Zone 2	7627	$7.10 \times 10^4$	0.11	$4.0 \times 10^{-27}$
Zone 3	0.059	$6.52 \times 10^4$	$8.99 \times 10^{-7}$	$5.2 \times 10^{-23}$
Zone 4	0.001	$5.53 \times 10^4$	$2.03 \times 10^{-8}$	$4.5 \times 10^{-21}$

The cooling stage was fixed at 77 cm from the quartz tube entrance and the aggregate size was measured at different points in the quartz tube. This was to observe the point at which the initial aggregate size formed. The results, shown in Fig. 3.11, indicate that the final aggregate size is effectively fixed near the beginning of the quartz tube. Other studies show initial aggregates formed grew in size, as

initially aggregate number concentration is high which enables collision between aggregates.<sup>57; 69</sup> However, our results show the initial aggregate size is nearly the same as the final aggregate size at the point of collection. This could be because the number concentration is not high enough to enable collision between aggregates or the stainless steel probe may not have been positioned high enough to capture the initial aggregate formation. The sampling probe was not long enough to reach higher into the reactor. The initial aggregate size was measured at a location (within the first 10 cm of the quartz tube), at which the temperature was 450 –500 °C. The time required for complete reaction was estimated to be approximately 1.1 secs, while the particle residence time by the location of measurement was 4.4 secs. This suggests that the TTIP precursor vapor will have completely reacted, with the products forming particles by the location at which the measurement was taken. It should also be noted that the residence time in the sampling probe was calculated to be 2.8 – 3.2 secs. Compared to the residence time in the quartz tube (16 - 28 secs), it is small and we make assumptions that any collisions inside the sampling tube will be minimal. Experimental information on the residence and reaction times is given in Appendix A.

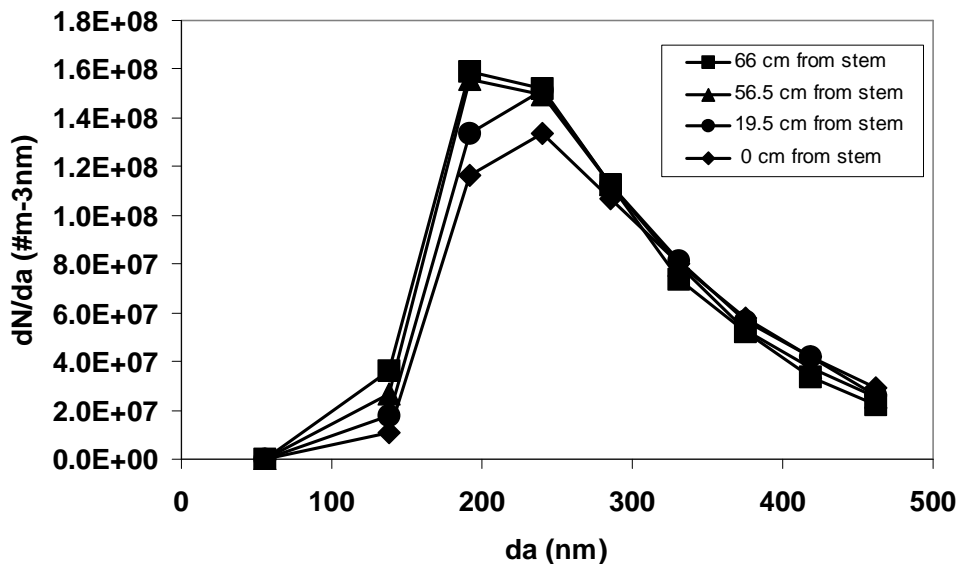


**Fig 3.11.** Aggregate size distribution in quartz tube at 77 cm from the quartz tube entrance.

The estimated porosity of the films deposited was  $98 \pm 1\%$ . The films are highly porous. A typical load-indentation depth curve is presented in Fig. 3.12. The gap between the approaching and retracting curves is a manifestation of plastic deformation. The retracting curve also shows a sawtooth shape towards the end of the curve; this has been interpreted to be the breaking of the aggregate chains as the cantilever is being pulled up from the film after indentation. This was also observed by Friedlander et al., in their AFM indentation of carbon nanoparticle aggregates.<sup>27</sup>

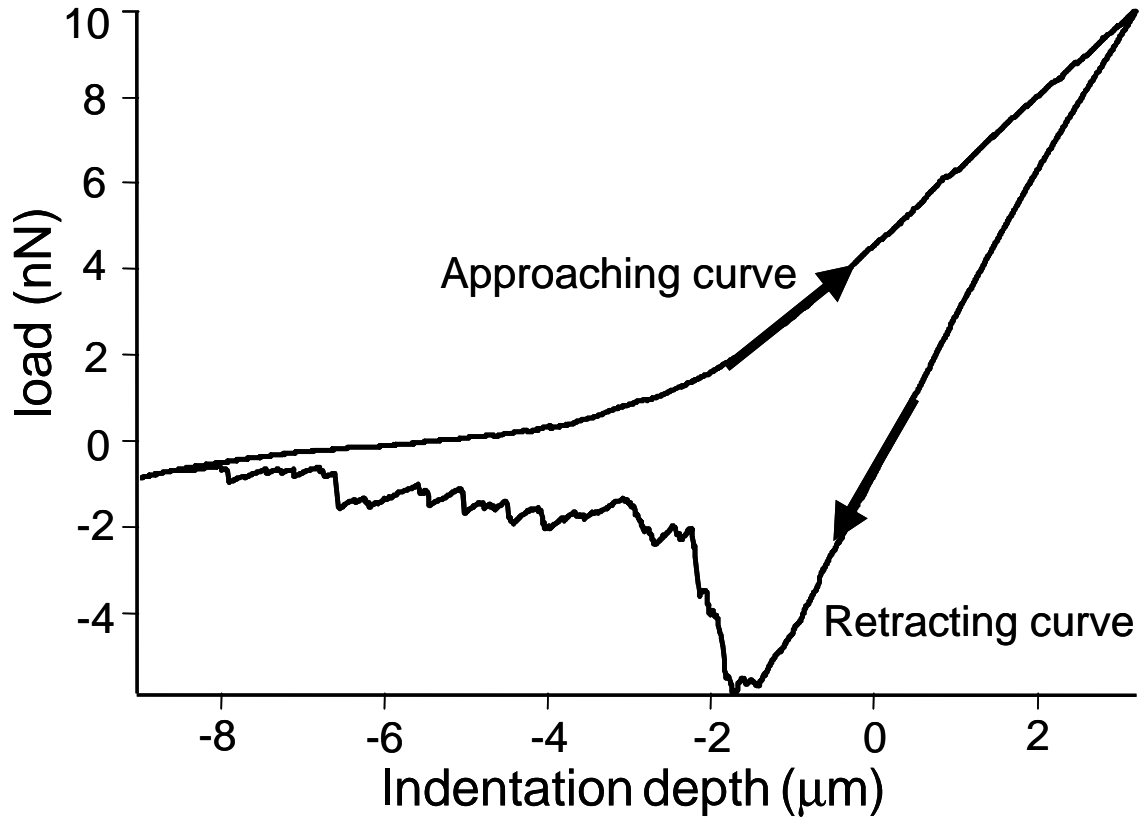


**Fig. 3.12.** Typical load-indentation curve.

The Young's modulus of the films was estimated from the AFM measurements, and normalized with respect to the shortest residence time sample's Young's modulus. The Young's modulus was normalized because the magnitude of the modulus was much less than values obtained using another instrument, and reported in Chapter 4 of this work. This may be attributed to the differences in adhesion of the sphere unto the cantilever tip. The sphere may not be adhered strongly and therefore it may have lead to inaccurate determination of the spring constant, or the tip of the cantilever may have ended up indenting the film rather than the sphere. However, since the same tip and sphere combination was used for all measurements reported in this Chapter, we

can focus on the relative values of the Young's modulus as a function of film properties. The results show a decrease in the Young's modulus with an increase in primary particle diameter, as shown in Fig. 3.13.

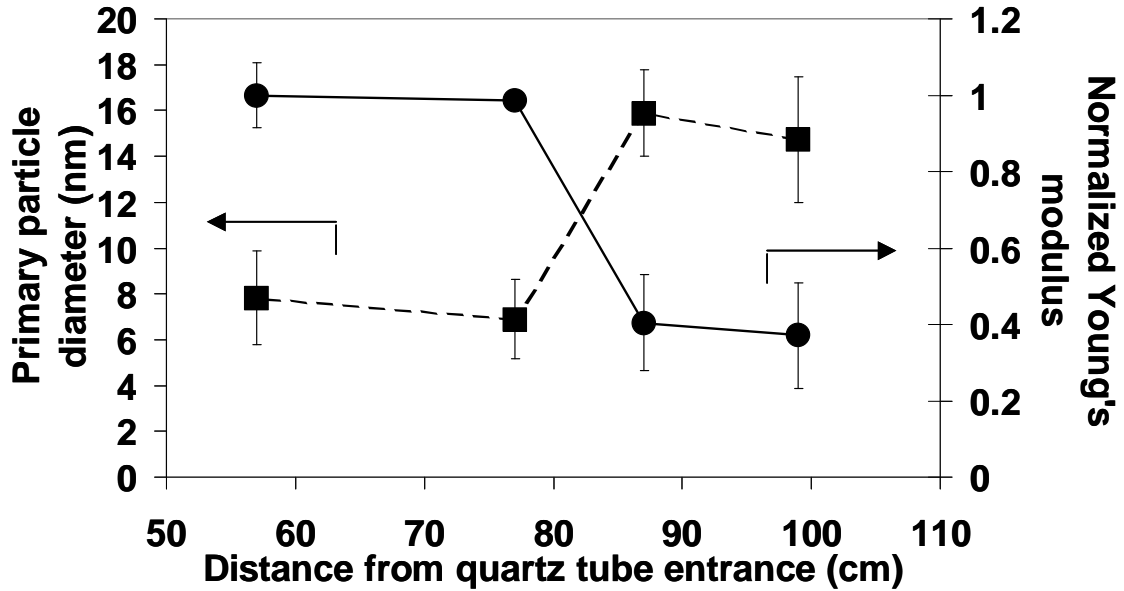


**Fig. 3.13.** Effect of primary particle diameter on Young's modulus. The error bars for primary particle diameter represents the standard deviation of the size distribution. The error bars for Young's modulus represent standard deviation of two to four measurements. In some cases, the standard deviations are smaller than the data point markers.

This could be as a result of increase in surface energy with decreasing particle size. In a study of influence of grain size on Young's modulus, a decrease in grain size led to an increase in grain boundary defects, which ultimately resulted in a decrease in Young's modulus.<sup>70</sup> However, Dinreille et al.<sup>71</sup> showed that the effect of

surface energy on the elastic behavior becomes more significant when one of the dimensions is below 10 nm. The result of our study is comparable to the results of Dinreville et al.'s study because our synthesized films are made up of particles and not grains. A reasonable explanation is that grain boundaries affect materials composed of grains, while surface energy affects materials composed of particles. In general, a change in primary particle diameter influences material properties. The average aggregate mobility diameter was the same in all four zones and any influence on Young's modulus could therefore not be evaluated.

### **3.6 Summary**

A hybrid process based upon gas-to-particle conversion and particle precipitated chemical vapor deposition was used to synthesize deposits of titania nanoparticle aggregates. The residence time of particles in the reactor was varied and the influence was studied in relationship to particle morphology and mechanical properties. Increase in residence time was shown to result in an increase in primary particle diameter, the aggregate size however remained constant. This was interpreted to be because the nanoparticles within each initial aggregate coalesce and grow, while the mass of the aggregate is still conserved resulting in a constant aggregate electrical mobility diameter as measured with a differential mobility analyzer and a condensation particle counter. The Young's modulus results show that a decrease in the primary particle diameter results in an increase in the Young's modulus of the synthesized films.

## **CHAPTER 4: EFFECT OF PHYSICAL SINTERING ON MECHANICAL PROPERTIES**

### **4.1 Abstract**

Highly porous films of titania composed of nanoparticle aggregates were synthesized via gas-to-particle conversion and particle-precipitated chemical vapor deposition. The films were annealed in air for 12 hours at temperatures ranging from 400 to 1000 °C. Atomic force microscopy was used to determine the Young's modulus and hardness of both the as-synthesized and annealed films. The Young's modulus and hardness of the as-synthesized films were  $4.0 \pm 0.4$  MPa and  $0.026 \pm 0.003$  MPa, respectively. There was no significant change in either modulus or hardness upon annealing until the films were annealed at a temperature of 1000 °C. The Young's modulus and hardness of these films were  $56 \pm 6$  MPa and  $0.10 \pm 0.01$  MPa, respectively. Results from dynamic light scattering measurements of aggregate size and surface area measurements suggest that annealing at 1000 °C leads to increased networking between distinct nanometer scale titania aggregates that strengthens the film.

## 4.2 Introduction

Annealing is a heat treatment in which a material is exposed to an elevated temperature for an extended amount of time and then cooled. It is used to alter properties of the material by sintering. Sintering is the movement of material at the atomic level in a system of particles.<sup>72</sup> Movement of material occurs via one or more of the following: grain boundary diffusion, surface diffusion, volume diffusion and viscous flow. Lunden<sup>73</sup> concluded that surface and grain boundary diffusion are the dominant mechanisms of movement of material in solid phase nanosized particles. Lunden also shows in her work that surface diffusion dominates as temperature increases. Sintering is normally accompanied by densification and an increase in particle size resulting in loss of surface area.

Results of studies on microstructural changes of titania films with heat treatment revealed that crystallinity, specific surface area and photocatalytic properties of the titania films changed with increasing calcining temperature.<sup>20; 21</sup> Titania films sintered by heating were shown to have a more homogeneous morphology and higher electrical density than pressure sintered titania films.<sup>18</sup> The result was attributed to the heat sintered films being well connected. The above-mentioned studies are of the effect of heat on photocatalytic properties of titania films. In this work, we show the influence of annealing on the mechanical properties of titania nanoparticulate films.

## 4.3 Experimental

### 4.3.1 Experimental Procedure

Titania nanoparticulate films were prepared by thermal oxidation of titanium tetraisopropoxide (TTIP; Acros Organics, 98+ %) at 1000 °C to form nanoparticle aggregates, followed by deposition. The aerosol reactor is shown in Fig. 4.1. The reaction chamber is a quartz tube (National scientific; ID 47 mm, OD 50 mm, 43 inches in length) that is vertically mounted within a three-zone furnace (Lindberg 54747-V Tube Furnace). Within the quartz tube, film deposition occurs by thermophoresis onto a substrate placed on an adjustable, vertical water-cooled stage with the cooling water maintained at 15 °C. The stage surface temperature was measured to be 120 °C at a furnace temperature of 1000 °C and with the stage in the lower heating zone.<sup>58</sup> The substrate used to collect the particles was a polished square shaped silicon wafer (475-575 μm in thickness, cut to 2 cm x 2 cm, Silicon Quest International). The liquid TTIP was housed in a 150 ml electropolished stainless steel bubbler placed horizontally in line with the gas-drying unit. A gas-drying unit (Drierite) was used to remove any moisture from the carrier gas before it comes in contact with the precursor, which is moisture sensitive.

The bubbler was heated to 50 °C to increase the vapor pressure of the TTIP. The feed lines going into the reactor chamber were heated to 150 °C to prevent condensation of the TTIP vapor. Oxygen (99.99%, Air Products) was allowed to flow in at 900 sccm (standard cubic centimeters per minute). Argon (99.99%, Air Products), the carrier gas, was fed into the gas-drying unit at 325 sccm. The TTIP vapor molar flow rate out of the bubbler was  $8 \times 10^{-6}$  moles/min assuming vapor was

saturated with TTIP. The processing time in the film formation experiments, defined as the amount of time in which the carrier gas was supplied to the bubbler, was four hours.

All runs were produced under the same conditions. Material was collected for additional characterization requiring larger sample amounts by scraping off the film deposited on the sides of the cooling stage. This material is representative in terms of surface area as well as chemical composition and crystalline phase of the film on the wafer. The titania nanoparticle aggregates were deposited at the same time on both the wafer and stem of the water-cooled stage on which the wafer was placed. Scraping the material off the stem breaks some van der Waals bonds between aggregates in the structure, but it is still representative of the film on the wafer on a shorter length scale.

The powders collected from the experiments were annealed in a 5 mm diameter porcelain crucible placed in a bigger crucible for ease of handling. The samples were annealed in a BlueM furnace at temperatures ranging from 400 to 1000 °C for 12 hours. 400 and 1000 °C were chosen, as they are both lower and upper ends of annealing temperatures seen in literature<sup>20; 74</sup>. The heating rate determined by careful temperature measurements ranged from 11-28 °C per minute and cooling rate ranged from 2-7 °C per minute.

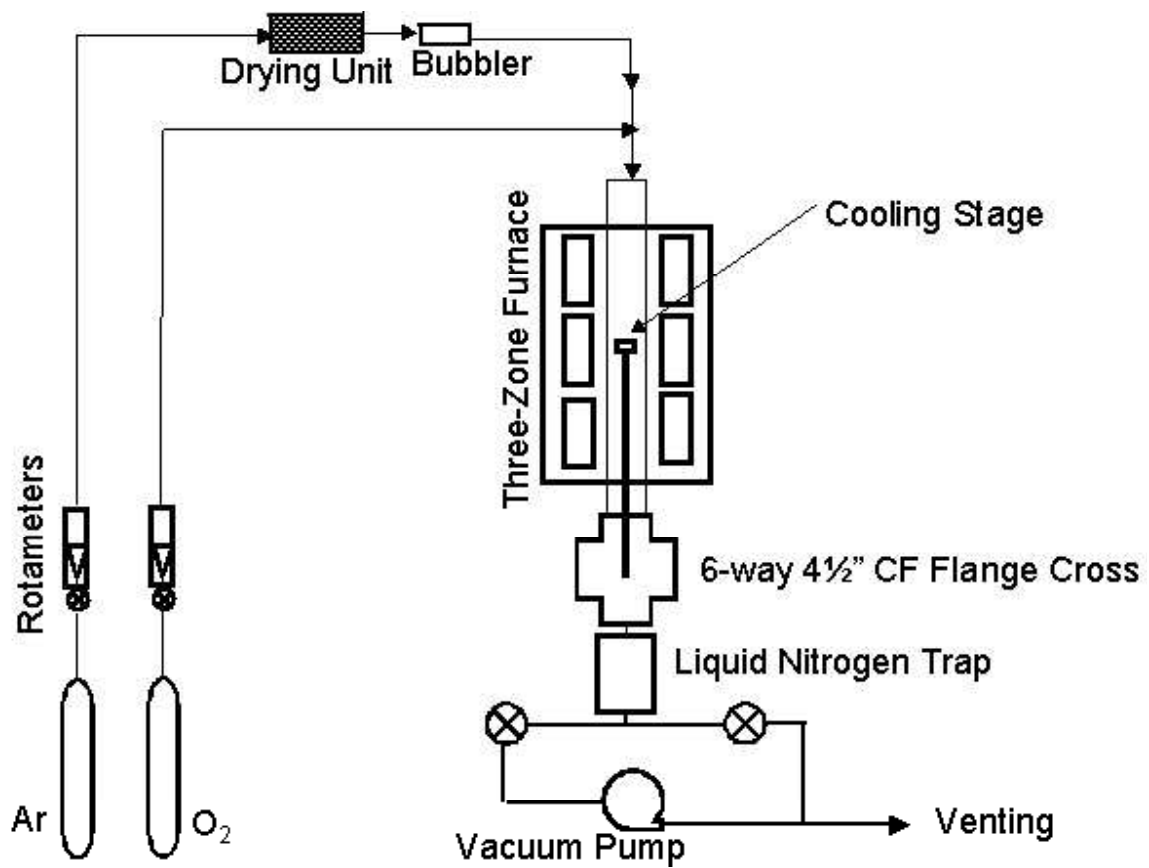


**Fig. 4.1.** Overall schematic of the aerosol growth and film deposition process.

## 4.4 Characterization Methods

### 4.4.1 Physical and Chemical Characterization

Transmission electron microscopy (TEM; Hitachi 600AB) was used to determine the size distribution of primary particles. Samples were prepared by pressing a carbon TEM grid to the collected powder and tapping to remove excess powder. The average size was determined by measuring the diameters of 50 primary particles. Measurements of aggregate size were obtained using dynamic light scattering (DLS; Photocor-FC). The photon correlation method is used to determine the velocity distributions of particles in suspension and undergoing Brownian motion by measuring the dynamic fluctuations of the intensity of the scattered light. From these measurements, the radius of a hydrodynamically equivalent sphere, one with the same diffusion coefficient as the aggregate, is determined.<sup>75</sup> Samples were diluted in 4 ml of water and sonocated for an hour to break the powder into aggregates before measurements were taken. Scanning electron microscopy (SEM; JEOL SEM 5400) was used to measure the approximate thickness of films. The mass of the film was measured gravimetrically by weighing the wafer before and after film deposition. The density of the films was estimated from the measured area of the wafer, and measured thickness and mass of the films. The porosities of the films were calculated with the densities of the film ( $\rho_{film}$ ) and bulk solid ( $\rho_{solid}$ ) as shown in the equation below

$$Porosity = 1 - \frac{\rho_{film}}{\rho_{solid}} \times 100 \quad . \quad (1)$$

The Brunauer-Emmett-Teller gas adsorption method (BET; Quantachrome Nova 1200) was used to perform surface area measurements. X-ray diffraction (XRD; Bruker D8 Diffractometer) analysis was used to determine the crystalline

phase of the material. Titania production was confirmed with Fourier transform infrared spectroscopy (FTIR; Nicolet 550 Series II) on pellets consisting of a 1:200 ratio of titania to KBr.

#### **4.4.2 Mechanical Characterization: AFM Indentation**

The AFM indentations were conducted by Prof. Gil Lee and Dr Jin-won Park of Purdue University. Indentation was conducted using a 3-D Molecular Force Probe AFM (Asylum Research, Santa Barbara, CA) with a closed loop piezoelectric transducer. The measurements were made in a closed chamber, allowing the environment to be changed from air to ultra-dry nitrogen. Indentations were performed with a 7.3  $\mu\text{m}$  diameter amorphous silica sphere attached to silicon oxynitride and silicon cantilevers (Olympus, Shinjuku-ku, Tokyo, Japan). The spring constants for the silicon oxynitride and silicon cantilevers were determined from the thermal frequency spectrum of the cantilevers to be 0.22 and 70 N/m, respectively.<sup>76</sup>

The applied load and depth of penetration into the titania films were continuously monitored at a series of maximum loads, resulting in a set of displacement-deflection curves. Two different force loads were used for the indentation experiments. A 7 nN force load was applied on the films with the 0.22 N/m cantilever, while 3.9  $\mu\text{N}$  force load was applied with the 70 N/m cantilever. Indentation is made up of two components, namely plastic and elastic indentation. These components can be identified from analysis of the unload curve. If the unload curve is approximately identical to the load curve, the indentation includes only the

elastic component. For an elastic half space, the depths of the elastic indentation ( $\delta$ ) into the films were determined using the relation

$$\delta = \Delta d - \Delta z , \quad (2)$$

where  $\Delta d$  is displacement of the porous film and  $\Delta z$  is the deflection of the silica sphere attached to the cantilever. The lateral motion of the cantilever on the surface is neglected in this calculation, which is a reasonable approximation due to the 100 to 400 nm displacement distance used in this study.

The unload curve was used to estimate the elastic modulus according to the following equation

$$S = \frac{2}{\sqrt{\pi}} E^* \sqrt{A} . \quad (3)$$

Here,  $S$  is the measured stiffness of the upper portion of the unloading curve and  $A$  is the projected area of the contact of the spherically elastic indentation which was obtained by subtracting a residual depth ( $h_r$ ) from the total indentation depth ( $h_t$ ).<sup>60; 77</sup>

The residual depth was measured by monitoring the difference in the distance between the point where the load data started to increase above zero and the point where the unload curve reached zero. Therefore, the equation for  $A$  is as follows

$$A = \pi \left\{ 2R(h_t - h_r) - (h_t - h_r)^2 \right\} . \quad (4)$$

The reduced Young's modulus is given as

$$\frac{1}{E^*} = \left( \frac{1 - \nu_m^2}{E_m} \right) + \left( \frac{1 - \nu_i^2}{E_i} \right) . \quad (5)$$

In which  $\nu_m$  and  $E_m$  are the Poisson's ratio and Young's modulus for the porous film respectively, and  $\nu_i$  and  $E_i$  are Poisson's ratio and Young's modulus for the material of the indenter material, respectively. Since the silica sphere's Young's modulus, 94

GPa, is much larger than what was expected for the Young's modulus of the films, the value of  $E^*$  is dominated by the properties of the film and reduces to

$$\frac{1}{E^*} \approx \left( \frac{1 - \nu_m^2}{E_m} \right). \quad (6)$$

The Poisson's ratio of the films was not known. However, Arnold *et al* show that Poisson's ratio asymptotically approaches 0.5 as the porosity becomes close to 1.<sup>61</sup> The minimum porosity of all films including as synthesized and annealed was estimated to be 0.96. Therefore, the Young's modulus was calculated using 0.5 as a Poisson's ratio. Use of smaller values of the Poisson's ratio had a small effect on the measured mechanical properties of the films. The hardness,  $H$ , was calculated from the applied force divided by the projected contact area

$$H = \frac{P}{A} \quad (7)$$

where  $A$  is given by equation 4 and  $P$  is the applied load.<sup>77</sup>

## 4.5 Results and Discussion

In the reactor, TTIP precursor vapor reacted to form condensable product species. The presence of condensable species in the gas phase caused the system to be in a non-equilibrium supersaturated state; the system then tries to achieve equilibrium by generation of new particles (homogeneous nucleation) or condensation on existing particles (heterogeneous condensation).<sup>50</sup> The particles then grow by collision and coalescence. The particles collide at a faster rate than they can completely coalesce, leading to formation of aggregates of partially sintered particles. The particles in each aggregate have chemical bonds connecting them together because of partial sintering. The aggregates are deposited on the silicon wafer, where they do not sinter further because of the low temperature at the surface; they are then connected via van der Waals forces. A schematic illustrating the bond types between the particles in the film is shown in Fig 3. After deposition, various structural and mechanical characterization techniques were used to understand the structure-mechanical property relationship of the as synthesized and annealed films.

X-ray diffraction (XRD) analyses, of the synthesized material revealed the crystalline phase of the as-synthesized materials to be anatase, as shown in Fig. 4.2. The XRD spectrum has the characteristic single peaks at d spacing values of 3.54, 2.37 and 1.89 Å with a characteristic double peak at 1.70 and 1.67 Å.<sup>62</sup> The diffraction pattern values and intensities are given in Appendix A.

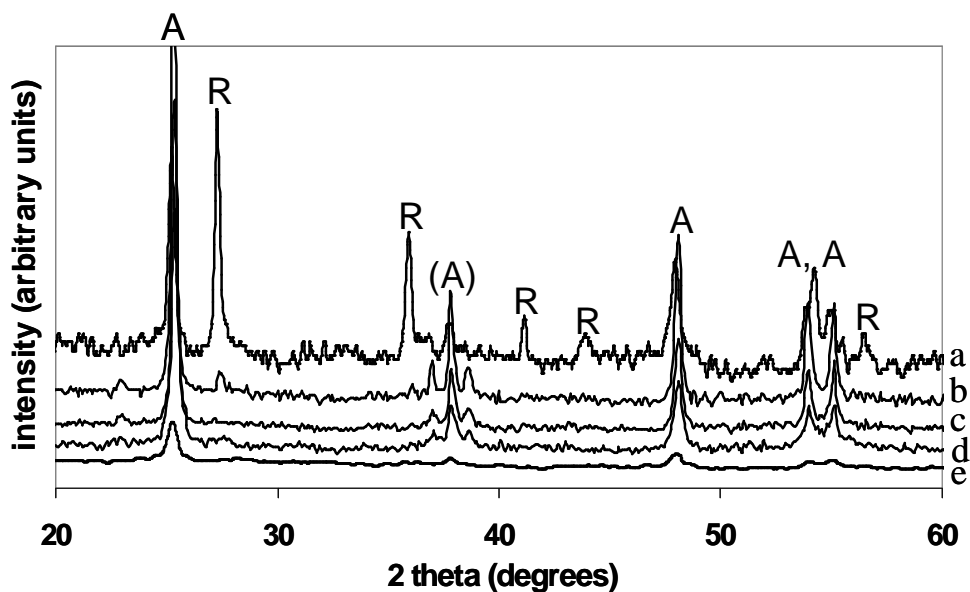


**Fig. 4.2.** XRD spectra of a) the sample annealed at 1000 °C, b) the sample annealed at 800 °C, c) the sample annealed at 600 °C, d) the sample annealed at 400 °C and e) the unannealed sample. The notations A and R represent anatase and rutile crystalline phases respectively.

Annealing results in a partial phase transition from anatase to rutile, starting between 800 and 1000 °C. The XRD spectrum of material annealed at 1000 °C has additional peaks at d spacing values of 3.28, 2.50, 2.19, 2.06 and 1.63 Å which all correspond to the presence of the rutile crystalline phase.<sup>62</sup> This was expected as other reports on the heat treatment of titania describe a phase transformation from anatase to rutile at 800 °C<sup>20</sup> and even at 600 °C<sup>21</sup>, although the duration of the heat treatment was shorter, one hour and three hours respectively. X-ray photoelectron spectroscopy (XPS; Kratos AXIS 165) was used to check for impurities in the films.

The results showed the presence of carbon in the as synthesized and annealed films. The carbon could be from products of incomplete reaction condensing on the films, or even from compounds that condense out of the air onto the films. The thickness of the deposited films ranged from 456 to 627  $\mu\text{m}$  as measured from SEM images.

After annealing at 600  $^{\circ}\text{C}$ , a slight increase was seen in primary particle diameter, as measured from TEM images, examples of which are shown in Fig. 4.3.

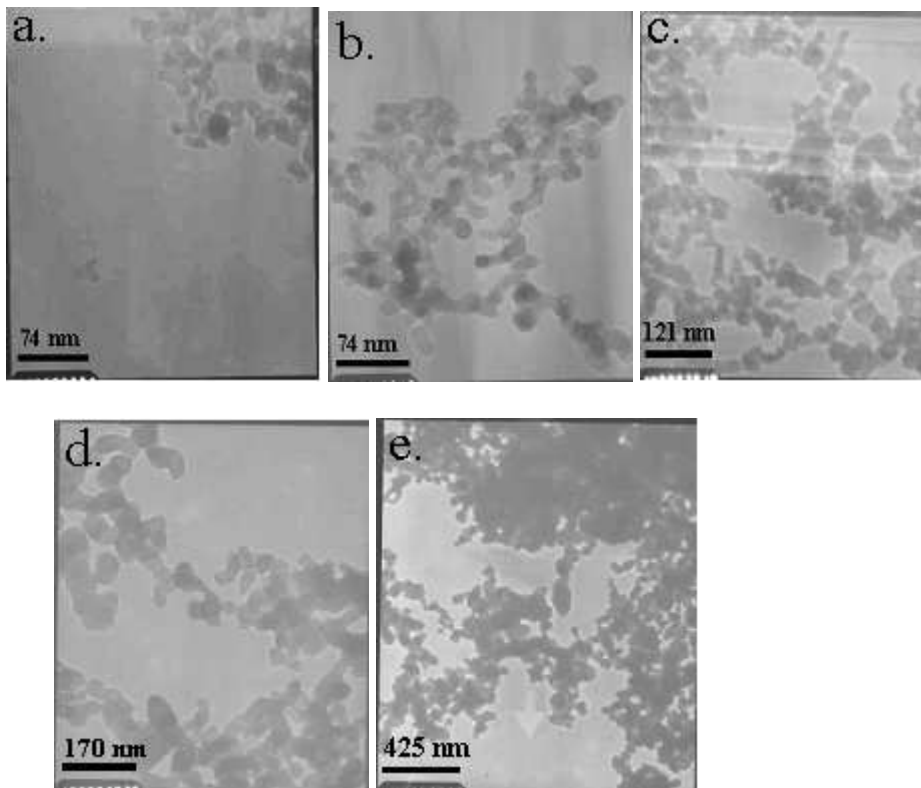


**Fig. 4.3.** Transmission electron microscope images of a) the unannealed sample, b) the sample annealed at 400  $^{\circ}\text{C}$ , c) the sample annealed at 600  $^{\circ}\text{C}$ , d) the sample annealed at 800  $^{\circ}\text{C}$  and e) the sample annealed at 1000  $^{\circ}\text{C}$ .

The number average primary particle diameter as a function of annealing temperature is given in Fig. 4.4.

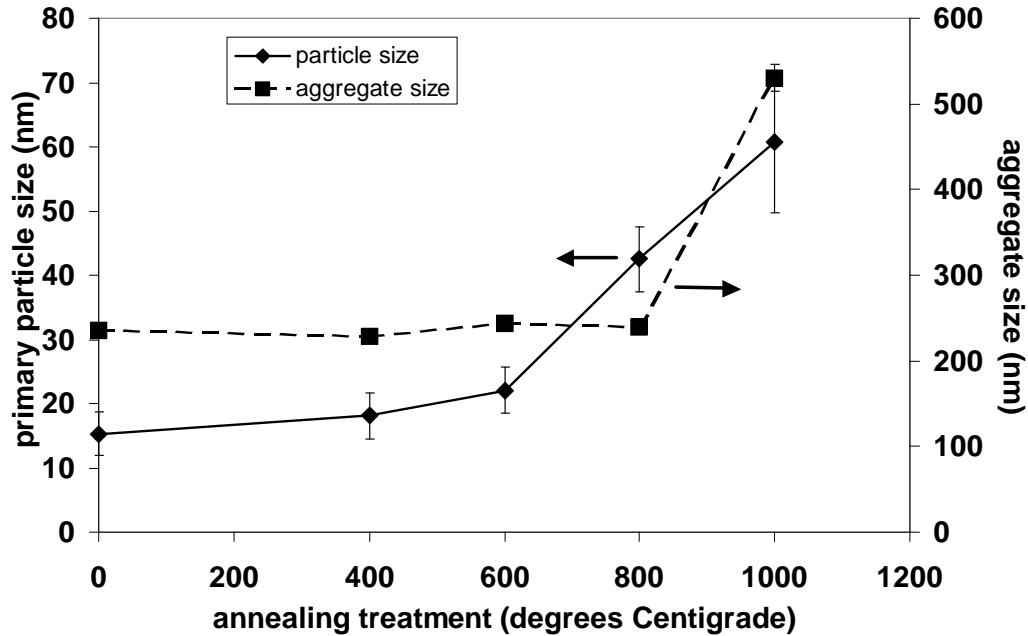


**Fig. 4.4.** Effect of annealing temperature on primary particle and aggregate sizes.

Error bars represent measurement uncertainty. In some cases, the error bars are smaller than the data point markers.

As shown in Fig. 4.4, the particles grew to three times their original diameter when annealed at 800 °C and to quadruple their original diameter at 1000 °C. As these temperatures are well below the melting temperature of titania (1855 °C), particle growth is believed to occur via solid-state diffusion. The above-described growth occurred within each aggregate.

Aggregate size measurements were made using dynamic light scattering. There was evidence of growth via sintering between particles from different

aggregates only at the highest annealing temperature. As shown in Fig. 4.4, the aggregate size remains constant at 800 °C but the primary particles are three times their original diameter. At 1000 °C, the aggregate size increases while the primary particles have grown to four times their original diameter.

This increase in aggregate size, observed using DLS, is evidence that there is sintering at very high temperature between particles from initially distinct aggregates. During sintering, van der Waals bonds between particles are converted to chemical bonds, or new chemical bonds between particles are formed where there was no bond before, or some combination of both occurs. The number of particles connected by chemical bonds increases and this ultimately increases the relative proportion of chemical bonds to van der Waals bonds within the film. In other words, this increases the interconnectivity of the particles within the film, forming a more networked and presumably stronger structure. This may have implications in the application of titania in solar cells, as a results from a recent study<sup>24</sup> showed that electron diffusion increases with increasing connectivity between particles.

BET specific surface area ranged from 40 m<sup>2</sup>/g for the unannealed film to 4.3 m<sup>2</sup>/g for the sample annealed at 1000 °C. The specific surface area of the particles decreased as expected with increase in particle size. The BET results depicted in Fig. 4.5 show a loss of surface area in the film when annealed.

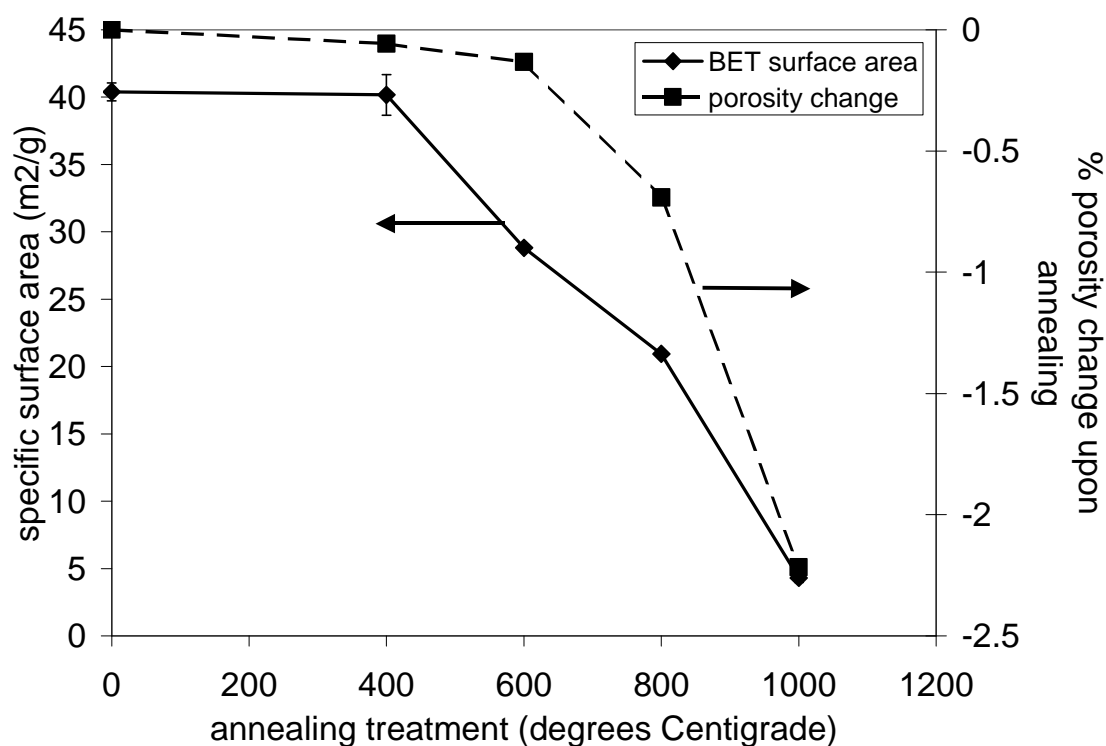


**Fig. 4.5.** Change in specific surface area and film porosity with annealing treatment. Error bars represent measurement uncertainty. In some cases, the error bars are smaller than the data point markers.

The estimated density and porosity of as synthesized film were  $0.044 \pm 0.003 \text{ g/cm}^3$  and  $98.6 \pm 0.1\%$ . The density and porosity of the films did not change significantly until annealing at  $1000 \text{ }^\circ\text{C}$ , after which both were estimated to be  $0.129 \pm 0.008 \text{ g/cm}^3$  and  $96.7 \pm 0.2\%$ . The percentage change in porosity of annealed films to as synthesized film was slight until annealing at  $800 \text{ }^\circ\text{C}$  and then became more significant with the  $1000 \text{ }^\circ\text{C}$  annealing treatment. This is probably because annealing increases the particle size and degree of neck formation between the particles.

However, the overall porosity of the film is not significantly affected. The overall porosity in the film decreased from 98.6% to 96.7%, when annealed at 1000 °C. The film's thickness observed by SEM decreased with increasing annealing temperature and decreased to a third of the original thickness when annealed at 1000 °C.

Fig. 4.6 presents load-indenter displacement curve for the indentation on the porous films annealed at 1000°C with the cantilevers. The form of the retracting force curve reflects the fact that the indentation included plastic deformation. The retracting force curve (unload curve) was used to calculate the Young's modulus of the films. The Young's modulus was found to be  $56 \pm 6$  MPa for 0.5 Poisson's ratio.

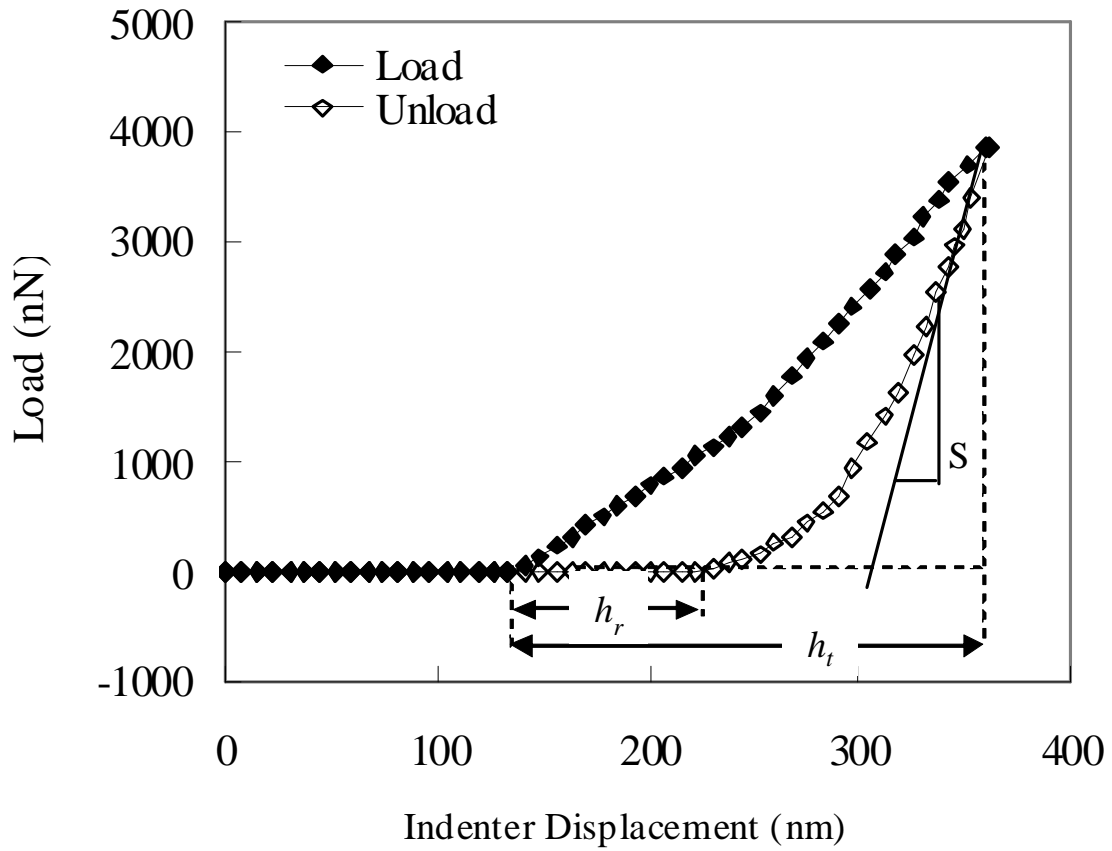


**Fig. 4.6.** Atomic force microscope indentation measurements on the porous films annealed at 1000 °C. Load - indenter displacement behavior for a 70 N/m cantilever at a maximum load of 3.9  $\mu$ N.

An average Young's modulus and hardness, calculated using three force curves as a function of anneal temperature, are presented in Table 4.1 and Fig. 4.7.

**Table 4.1.** Average value of Young’s modulus and hardness for each film. The error represents standard deviation of three measurements.

Treatment	Young’s Modulus (MPa) ( $k = 70 \text{ N/m}$ , $\nu_m = 0.5$ )	Hardness (MPa)
Unannealed	$4.1 \pm 0.3$	$0.032 \pm 0.003$
Annealed at 400 °C	$3.9 \pm 0.3$	$0.024 \pm 0.003$
Annealed at 600 °C	$3.9 \pm 0.3$	$0.021 \pm 0.003$
Annealed at 800 °C	$4.0 \pm 0.3$	$0.029 \pm 0.002$
Annealed at 1000 °C	$56 \pm 6$	$0.10 \pm 0.001$

The Young’s modulus was 3.6 - 4.4 MPa for unannealed films and films annealed at temperatures up to 800°C. This modulus is approximately five orders of magnitude smaller than the bulk modulus of titania which is 230 GPa.<sup>78</sup> These Young’s modulus results are for films with porosities of approximately 98%. Our results compare well to silica aerogel with a porosity of 96%, that has a reported Young’s modulus of 1.2 MPa.<sup>79</sup> The results from our previous work show a much smaller Young’s modulus, and this may be attributed to the differences in adhesion of the sphere unto the cantilever tip. However, we can focus on the relative values of the Young’s modulus as a function of film properties. There is no change in Young’s modulus when annealed at 800 °C even though there is a significant increase observed in primary particle size. However, the aggregate size remains the same as

that of when initially deposited. This suggests that the proportion of chemical bonds to van der Waals bonds is approximately the same as when initially deposited. The indentation results show no major change in Young's modulus until the film is annealed at 1000 °C, at which point the value is seen to increase by approximately one order of magnitude as shown in Fig. 4.7. This significant increase could be because of the increased networking (the formation of chemical bonds) between initially distinct aggregates. In this case, we suggest the possibility that the relative proportion of chemical bonds to van der Waal's bonds within the film increases, thus increasing the Young's modulus

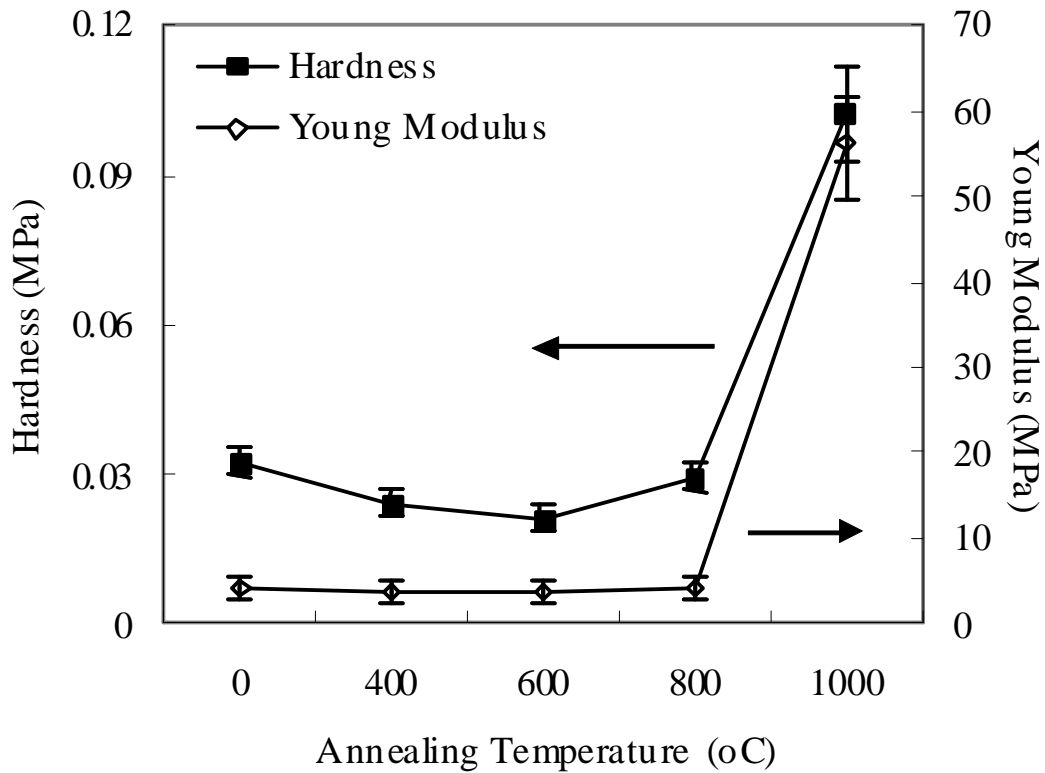


**Fig. 4.7.** Young’s modulus and hardness of the titania film as a function of annealing temperature. Error bars represent standard deviation of three measurements.

We suggest that annealing of the films at the higher temperatures may decrease the aggregate size via intraparticle growth within each aggregate, but this is counterbalanced by interparticle growth between initially distinct aggregates leading to an increase in aggregate size. These processes, particularly intraparticle growth within each aggregate, may cause mechanical instability in the film and densification will occur, as seen in the reduction of thickness of the films at the higher temperatures. The amount of densification that occurs is a function of the annealing temperature. At a higher annealing temperature, the rate of surface diffusion is

greater, leading to a faster rate of particle growth. The change in porosity resulting from the densification is one of two contributing factors to the Young's modulus increase at the highest annealing temperature. Growth of aggregates by interparticle sintering between initially distinct aggregates means more chemical bonds being formed and is the second contributing factor in the Young's modulus increase seen at the highest annealing temperature.

This relationship between Young's modulus and microstructure for porous materials has been explored through the development of theoretical models of structure-property correlations. A finite element approach was used to study the influence of porosity and pore shape on the elastic properties of model porous ceramics.<sup>80</sup> A differential method was used to calculate the Young's moduli of a solid that contains a random distribution of spherical inclusions and analytical solutions were obtained for the two limiting cases of rigid inclusions and vacuous pores.<sup>81</sup> For general cases, the predictions of the differential method compare very well to experimental results from the literature.<sup>81</sup> A comparative analysis of several theoretical models has been carried out to evaluate effectiveness of the models in predicting the Young's moduli by comparisons of predictions to experimental observations.<sup>82</sup> Interestingly, as shown by Roberts and Garboczi<sup>83</sup>, these theoretical models reduced to the same empirical power law relationship reported by Gibson and Ashby<sup>84</sup>

$$E_{film} = CE_{bulk\ solid} \left( \frac{\rho_{film}}{\rho_{bulk\ solid}} \right)^n \quad (7)$$

where the Young's modulus of the porous material ( $E_{film}$ ) is related to the solid Young's modulus ( $E_{bulk\ solid}$ ) via the film and solid densities,  $\rho_{film}$  and  $\rho_{bulk\ solid}$ , respectively. C and n are constants, the values of which depend upon material and processing history. For the case of our porous films, the observed values of Young's modulus and porosity also roughly follow this power law behavior with the pre-exponential constant C equal to 3.9, the exponent n equal to 2.9, and a correlation coefficient ( $R^2$ ) for the fit of 0.88.

Recently, an approach for predicting the elastic properties of porous materials was developed based upon a random network of struts of different thicknesses. This Gaussian Random Field (GRF) based structure is similar to our porous materials in that the struts (cells) in the model structure have varying thickness (size) representative of different bond strengths. The effect of porosity on the Young's modulus was investigated for the GRF structures by varying the thickness of the cell walls.<sup>85</sup> Increasing the cell wall thickness is similar to what occurs in our structures during annealing. The dependency of the Young's modulus on porosity also fit the general form of Equation 5. The parameters (pre-exponent and exponent) obtained in fitting results from the GRF structural model to the power law form, are within 7% of those obtained using our observed values. This suggests the GRF structural model with its varying strut thicknesses may indeed be representative of our film structure. Thus this model could be used in further studies for *a priori* predictions of the properties of highly porous films made by the same route of materials other than titania, or for predictions of properties of materials with microstructural parameters such as porosity beyond what can be easily generated experimentally.

As discussed earlier, Young's modulus and hardness of the nanoparticulate films were found to be dependent on the aggregate size. This is notable, as mostly primary particle size has been generally thought to influence properties of nanoparticle-based materials.<sup>17; 51; 52</sup> The change in aggregate size at 1000 °C, also corresponds to the change in porosity of the films. Porosity influences mechanical properties as corroborated with results of studies mentioned earlier of related materials. The results of this work indicate the importance of nanoscale structure (such as aggregate size) on macroscale properties (such as porosity, Young's modulus and hardness) after post processing. In order to investigate the effect of humidity, which might have lead to capillary bridging within the porous film, indentation experiments were performed with the film annealed at 600 °C at relative humidities between 2 and 60%. No significant difference was observed between the humidities suggesting that no capillary bridging occurred at the higher relative humidity.

## 4.6 Summary

The effect of heat treatment on nanostructure and mechanical properties, Young's modulus and hardness, of titania films deposited on a silicon substrate were studied via AFM indentation measurements and particle characterization techniques. The titania films were composed of titania nanoparticle aggregates connected together by van der Waals bonds, with chemical bonds between the primary particles in the aggregates. The Young's modulus of the prepared films was  $4.0 \pm 0.4$  MPa, significantly lower than bulk values for titania. The hardness was estimated to be  $0.026 \pm 0.003$  MPa, which is also significantly lower than bulk values. The films were annealed for 12 hours at temperatures ranging from 400 to 1000 °C. There was no change in Young's modulus and hardness until after annealing at 1000 °C. Both mechanical properties changed significantly and was estimated to be  $56 \pm 6$  MPa and  $0.10 \pm 0.01$  MPa, respectively. The change in the mechanical properties corresponds to the point at which the porosity value and aggregate size changes. This is attributed to a significant increase in the density and degree of networking between the aggregates, and is hypothesized to correspond to an increase in the amount of material per volume and proportion of chemical bonds to van der Waals bonds existing within the film. This increase in the amount of chemical bonds is likely from a conversion of van der Waals bonds in the film during annealing at very high temperatures. The increase in density is likely from the collapse of the film, resulting in reduced volume. It is interesting to note that annealing did not result in a significant increase in Young's modulus or hardness until most of the surface area was lost. This suggests

that annealing may not be the most effective process for strengthening films, if preservation of high surface area is desired.

## **CHAPTER 5: EFFECT OF STRUCTURE ON MECHANICAL PROPERTIES**

### **– SIMULATION STUDY**

#### **5.1 Abstract**

A combination of Monte Carlo and equivalent continuum simulation approach was used to investigate the structure-mechanical relationships of titania nanoparticle deposits. Deposits of titania composed of nanoparticle aggregates were simulated using a Monte Carlo approach with diffusion-limited aggregation. Each aggregate in the simulation is fractal-like and random in structure. In the deposit structure, it is assumed that there are only two values for the bond strengths; one representing the strong chemical bond between the particles in the aggregate and the other representing the weak van der Waals bond between particles from different aggregates. The Young's modulus is estimated from strain energy using an equivalent-continuum modeling approach. Influence of particle diameter and aggregate size on predicted Young's modulus of the titania deposit is investigated. The Young's modulus is observed to increase with a decrease in primary particle size and is independent of the size of the aggregates deposited.

## 5.2 Introduction

Titania nanostructured films have a variety of uses in high surface area applications such as gas sensors,<sup>1; 2</sup> photocatalysts in treatment of wastewater<sup>3</sup> and air pollutants,<sup>4; 5</sup> optical filters,<sup>6</sup> and photovoltaic electrodes for lithium batteries<sup>7</sup> and low cost solar cells.<sup>8</sup> Various processing routes<sup>12; 14; 18; 29</sup> have been used to synthesize titania films and it is important to understand the different processing-structure-property relationships to better improve on the efficiencies of the applications. In simulations of the microstructure of nanoparticle films, Lagemaat et al.<sup>23</sup> showed that increasing the porosity of the film decreases the coordination number of each particle while Cass et al.<sup>24</sup> showed the particle connectivity to influence electron transport. A study of titania nanoparticle size on electron diffusion by Nakade et al.<sup>17</sup> showed that diffusion coefficient increased with particle size. To ensure higher efficiency of solar cells, the stability of the titania nanoparticulate film has to be ensured. To that end, the results of this work are used to understand the effect of primary particle size, porosity and aggregate size on the mechanical properties of titania nanostructured films.

Simulations of aggregates are differentiated based on whether the aggregate grows by monomer-cluster or cluster-cluster. The monomer or cluster moves towards another monomer or cluster via reaction-limited, ballistic or diffusion-limited motion. Different aggregates that are fractal in nature can be generated with various fractal dimensions to indicate the compactness of the aggregate. Various groups have extensively studied aggregate and deposit growth. Meakin<sup>86</sup> studied the growth of aggregates in which clusters combined via ballistic trajectories. Meakin concluded

that the fractal dimensionality of the resulting aggregate of a cluster-cluster aggregation via linear trajectories is similar to that via Brownian motion. In another study, Meakin used an off-lattice ballistic aggregation to deposit particles on a surface. He showed that the tangent rule, the relationship between angle of growth and angle of incidence, for the orientation of columnar microstructures was only qualitatively correct.<sup>87</sup> Rosner et al.<sup>88</sup> used a combination of a deterministic motion and a random motion to simulate particle deposition. The height and porosity of the deposit was shown to depend on the Peclet number in a power law manner. In a similar approach, Giona and Patierno<sup>89</sup> used the same technique as Rosner et al. to study the structural properties of particle deposits and determined that surface and topological properties of deposits are fractal in nature. Kulkarni et al.<sup>26</sup> used Brownian dynamics simulations to predict the morphology of nanoparticle deposits in the presence of van der Waals and coulombic interactions. It was shown that more open structured deposits were generated in the presence of van der Waals interactions and increasing the electrical field strength generated more compact deposits.

The influences of a structure's characteristic length in the nanometer range on its mechanical properties are being studied by various researchers. Molecular dynamics simulations of straining of copper nanoparticle chain aggregates show kinked aggregates breaking at a greater applied strain compared to straight chain aggregates.<sup>90</sup> Molecular mechanics and Voronoi construction method was used to study the effect of grain size on elastic properties of nanocrystalline  $\alpha$ -iron.<sup>70</sup> A softening of the material was observed with decrease in grain size and attributed to the increase in grain boundaries. However, the latter mentioned material is not made

up of nano-sized structures but is a nanostructured material. Dingreville et al.<sup>71</sup> defined a nanostructured material as a microstructure having a characteristic length, such as the grain size of a polycrystal, in the nanometer range. They further defined a nano-sized structure as a structural element having at least one of the overall dimensions in the nanometer range. In their simulation work, it was found that the effect of surface energy on the elastic behavior becomes significant when one of the dimensions is below 10 nm. Evidently, the dimensions of the primary particles and aggregates will influence the mechanical properties of nanostructured titania deposits.

In this work, we simulate fractal aggregates by a monomer-cluster and diffusion-limited method. Deposition is simulated using a Monte Carlo approach in which the aggregates are randomly moved towards the substrate sequentially. The particle interactions at the nano level are captured as particle bond energies and are included in the strain energy calculation of the deposit. An equivalent continuum method via finite element analysis is further applied on the deposit structure to calculate the macroscopic Young's modulus of the deposit from the strain energy. We report results of influence of nanostructure on Young's modulus of deposits composed of titania nanoparticle aggregates.

## 5.3 Deposit Simulation

### 5.3.1 Aggregate Simulation

The first particle in the aggregate is created by randomly choosing  $x$  and  $z$  positions from a random number generator and fixing the  $y$  position at a chosen distance from the substrate. The chosen distance is close to the substrate to reduce computational time. A second particle is attached to the already created first particle in a random manner. Two of the Cartesian coordinates are randomly chosen via a random number generator and the third Cartesian coordinate is calculated to ensure the interparticle distance between the two particles is equal to the particle diameter. Based on the description above, the attaching particle can be attached to the existing particle in 24 different ways. The other particles making up the aggregate are attached by first randomly choosing a particle out of the already generated aggregate and then attaching in the same manner used above for the second attached particle. All randomly chosen coordinates and choices are done so using a random number generator. Each aggregate generated can have identical number of particles or a range of numbers of particles. The aggregate size is defined as the number of particles in the aggregate. The average coordination number of each aggregate is calculated using the average of the particle coordination numbers. The radius of gyration is the average distance of particles in an aggregate to the center of the aggregate; fractal dimension and fractal prefactor are exponential and pre-exponential parameters when the number of particles in an aggregate is plotted against the radius of gyration. The fractal dimension in particular is used to characterize the openness or compactness of

an aggregate. To characterize the aggregates, radius of gyration, fractal dimension and fractal prefactor are determined from equations 1 and 2.

$$R_g^2 = \frac{1}{N_p \sum_i r_i^2} \quad (1)$$

where  $r_i$  represents the distance between the center of the particle and the center of mass of the aggregate.

$$N_p = k_f \left( \frac{R_g}{d_p} \right)^{D_f} \quad (2)$$

where  $N_p$  represents the number of particles in aggregate,  $d_p$  is the diameter of a particle,  $R_g$  is the radius of gyration,  $D_f$  and  $k_f$  are the fractal dimension and fractal prefactor of the aggregate respectively.

### 5.3.2 Final Deposit Simulation

The growth of the deposit is by random motion of the aggregates sequentially towards the substrate. It is based on the assumption that the surrounding fluid is air and the particle concentration is dilute, so there is no interaction between aggregates until they collide on the substrate. An aggregate is generated and released from a height  $H$  above the substrate. The generated aggregate continuously moves and checks for collision between the particles in the incoming aggregate and deposited aggregates/substrate particles. Once a collision occurs, represented by an overlap between the particles, the aggregate is said to be deposited and the overlap removed mathematically along the axis joining the particle centers of the collided particles.

The motion of the aggregates is simulated on a substrate of length  $L$  and width  $W$ . When the aggregate moves out of the sidewalls of the substrate, periodic boundary conditions are applied, in which the aggregate leaving the sidewall on one side is reintroduced on the opposite sidewall. The length, width and height of the simulation box are  $40d_p$  each. The height of deposit varied with number of particles deposited. The porosity of the deposit grown was calculated on a box (approximately 6% of the deposit box) inside the deposit to remove any edge effects and was defined as:

$$P = 1 - \frac{n_{actual}}{n_{possible}} \quad (3)$$

where  $n_{actual}$  is defined as the number of simulated particles in the volume and  $n_{possible}$  is defined as the number of particles that can fill the volume and is given by

$$n_{possible} = \frac{\text{volume of box}}{\text{volume of single particle}} \cdot \quad (4)$$

#### 5.4 Continuum Finite Element Analysis

The methodology used is based on an equivalent-continuum method (ECM) developed by Odegard et al.<sup>91</sup> ECM is used to determine the bulk level mechanical properties of a material by combining computational chemistry and solid mechanics. Odegard et al. used the ECM method on a nanostructured material comprised of atoms. We extend this method here to determine mechanical properties of a nanostructured material comprised of nanoparticles.

This approach represents the particles and the bonds between the particles as an equivalent mechanical pin jointed truss model. The truss model is then substituted with an equivalent-continuum model, which is representative of the nanoparticulate structure. The equivalent continuum model is strained along the x-axis and the Young's modulus is calculated from the strain energy and solid mechanics constitutive laws. This method is computationally fast as finite element analysis is applied on only one structure. The strain value chosen is 1%. Fig. 5.1 illustrates how the equivalent-continuum model is representative of the nanostructured model.

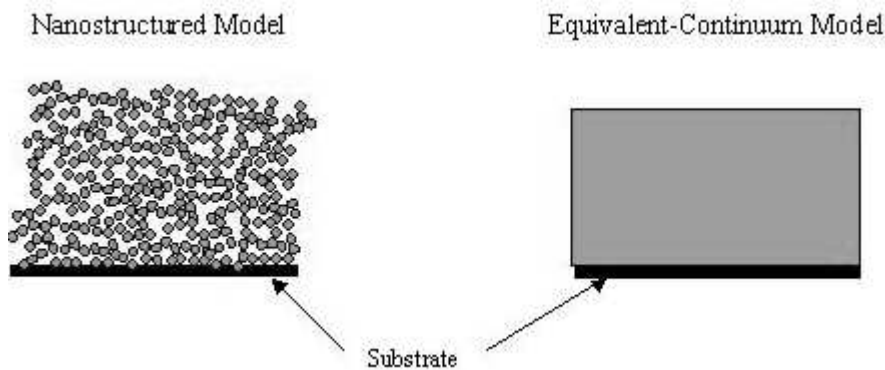


**Fig. 5.1.** Equivalent-continuum model representation of the nanoparticulate film.

In the deposit structure, it is assumed that there are only two values for the bond strengths; one representing the strong chemical bond between the particles in an aggregate and the other representing the weak van der Waals bond strength between particles from different aggregates. This is illustrated in Fig. 5.2.

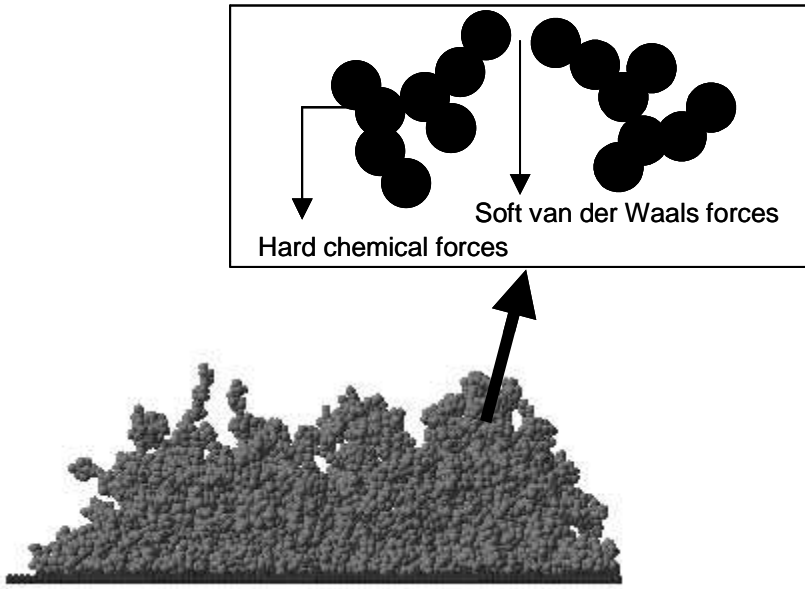


**Fig. 5.2.** Bond distribution in the nanoparticulate film.

The equivalent-continuum model starts with the derivation of the potential energy of the nanostructured deposit followed by the representation of the potential energy with an equivalent mechanical truss system. The truss system is then represented with a continuum method from which Young's modulus is calculated. A breakdown of the above is as follows:

*Nanopotential Energy:* The potential energy of the nanoparticulate deposit,  $\Lambda^n$ , is calculated as:

$$\Lambda^n = \sum E^{che} + \sum E^{vdw} \quad (5)$$

where  $E^{\text{che}}$ , defined as the chemical bond energy, is assumed to be a value that is one order of magnitude greater than the van der Waals bond energy. This is a first approximation and is consistent with what has been reported in literature.<sup>52</sup> The value of chemical bond energy is assumed to change linearly with particle diameter.  $E^{\text{vdw}}$ , defined as the van der Waals bond energy, is calculated from the theory of Hamaker<sup>92</sup> as shown in equation 6

$$E^{\text{vdw}} = - \frac{A}{12 \left\{ \frac{1}{x^2 + 2x} + \frac{1}{x^2 + 2x + 1} + 2Ln \left( \frac{x^2 + 2x}{x^2 + 2x + 1} \right) \right\}} \quad (6)$$

$$x = \frac{a_o}{d_p} \quad (7)$$

where  $d_p$  is the particle diameter,  $a_o$  is an assumed interparticle distance and A, the Hamaker constant.

*Equivalent Truss Model:* The mechanical strain energy,  $\Lambda^t$ , of the pin jointed truss model in which each truss member/rod represents a chemical bond of type a or van der Waals bond of type b between the particles is calculated as shown below

$$\Lambda^t = \sum \frac{A^a E^a (r^a - R^a)^2}{2R^a} + \sum \frac{A^b E^b (r^b - R^b)^2}{2R^b} \quad (8)$$

with  $A^a$  being the cross sectional area of the rod representing a chemical bond,  $E^a$  the Young's modulus of rod a,  $r^a$  and  $R^a$  are the deformed and undeformed lengths of rod a,  $A^b$  the cross sectional area of the rod representing a van der Waals bond,  $E^b$  the Young's modulus of rod b,  $r^b$  and  $R^b$  are the deformed and undeformed lengths of rod b.

To represent the mechanical behavior of the nanoparticles with the truss model, equations 5 and 8 must be equated using the Young's modulus of each rod by introduction of the nanopotential energy into the Young's modulus. The strain energy of the truss model (equation 8) is divided into a chemical component and a van der Waals component as shown in equations 9 and 10 respectively.

$$E^{che} = \frac{A^a E^a (r^a - R^a)^2}{2R^a} \quad (9)$$

$$E^{vdw} = \frac{A^b E^b (r^b - R^b)^2}{2R^b} \quad (10)$$

An equation for the Young's modulus of the rods can be obtained by solving equations 9 and 10, for  $E^a$  &  $E^b$  as shown in equations 11 and 12.

$$E^a = \frac{2E^{che} R^a}{A^a (r^a - R^a)^2} \quad (11)$$

$$E^b = \frac{2E^{che} R^b}{A^b (r^b - R^b)^2} \quad (12)$$

The equations for Young's modulus for the rods are then replaced in the equivalent truss equation (equation 8). A finite element model is then used to calculate the resultant mechanical strain energy in the equivalent-truss structure, which is given by

$$\Lambda^t = \sum \left( E_{after\ strain}^{che} - E_{before\ strain}^{che} \right) + \left( E_{after\ strain}^{vdw} - E_{before\ strain}^{vdw} \right) \quad (13)$$

*Continuum Model:* the mechanical properties of the continuum (a solid rectangle as shown in Fig. 1) are determined by equating  $\Lambda^t \equiv \Lambda^c$  under identical loading conditions (strain).  $\Lambda^c$  is the mechanical strain energy of the continuum model.

$$\Lambda^c = \frac{V\sigma_{ij}E_{ij}}{2} \quad (14)$$

where V is the volume of the rectangle,  $\sigma_{ij}$  is the stress component and  $E_{ij}$  is the strain component. Applying finite element analysis to the continuum structure gives

$$\Lambda^c = \pi E_L e^2 \quad (15)$$

where  $E_L$  is the longitudinal Young's modulus and e is the strain along the x-axis. Straining the truss elements changes the interparticle distance between the particles (the truss length), which results in a strain energy. The strain energies of the truss elements are calculated and summed as the mechanical strain energy of the continuum. The Young's modulus is calculated from the total strain energy and equation 15. All parameter values used are listed in Table 5.1.

**Table 5.1.** Parameter values used in simulations.

Parameter	Values
Hamaker constant	$164.9 \times 10^{-21}$ J
Chemical bond energy	$3.5 \times 10^{-18}$ J
Strain	0.01
Chemical bond interparticle distance	0.1 nm
van der Waals bond interparticle distance	0.4 nm

## 5.5 Results and Discussion

In the simulation, the fractal dimension, fractal pre-factor and average coordination number of the aggregates increased with aggregate size. The fractal dimension increased from 1.7 with 5 particles to 2.9 with 100 particles. The fractal pre-factor increased from 6.2 with 5 particles to 9.0 with 100 particles, while the average coordination number of the particles in each aggregate increased and stabilized at 2.02.

A growth of a deposit is shown in Fig. 5.3. As seen in Fig. 5.3 the deposit is very porous. The calculated porosity of a deposit simulated with particle size of 17 nm and aggregate size of 15 particles is 0.95, which is comparable to the experimental value of 0.98 porosity reported for titania nanoparticle deposits by Ogunsola et al.<sup>93</sup> The above-mentioned porous films of titania composed of nanoparticle aggregates were synthesized via gas-to-particle conversion and particle precipitated chemical vapor deposition. Indentation using atomic force microscopy, was used to determine the Young's modulus of the synthesized films. Our deposit simulations were based on achieving the same level of porosity and structure in the deposits as had been synthesized, to compare both experimental and simulated Young's modulus.

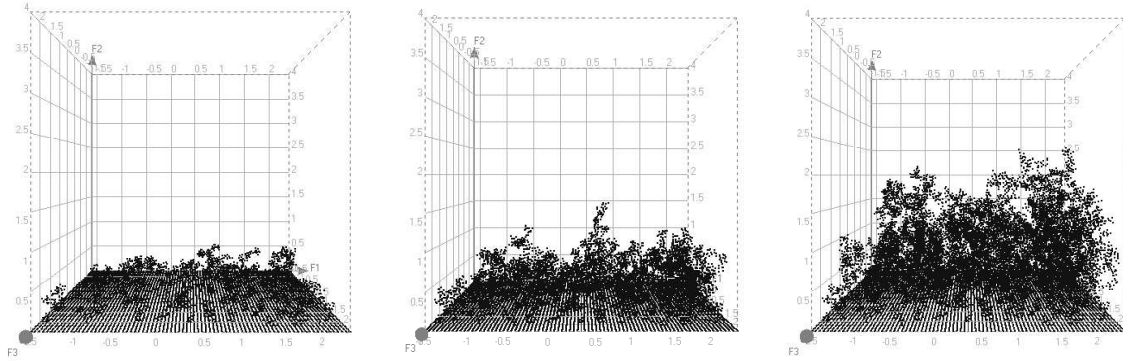


**Fig. 5.3.** Growth of nanoparticle deposit obtained from simulations. F1, F2 and F3 represent x, y and z axis respectively.

The Odegard continuum method was applied to a deposit with primary particle size of 17 nm, aggregate size of 15 particles and porosity of 0.95. The calculated Young's modulus is 3.5 MPa. In previous studies in the literature, the Young's modulus for bulk titania estimated from nanoindentation<sup>78</sup> and 3 point bending<sup>94</sup> were reported to be approximately the same; therefore, comparing the Young's modulus from the simulation to the indentation measurements is reasonable. The Young's modulus calculated from the simulation was compared to Young's modulus estimated from indentation measurements of a titania deposit with similar parameters. The experimentally generated titania deposit had particles that were 17 nm in average diameter. The Young's modulus estimated from the indentation results was 2.6 MPa, which is comparable to the calculated Young's modulus of the simulated deposit. The very small difference is attributed to porosity of the simulated deposit being slightly lower than the experimentally generated deposit. This shows that the continuum method is a viable way of predicting the Young's modulus of a

deposit of nanoparticles. After validation of the continuum method, the effect of primary particle size, aggregate size and porosity on the Young's modulus was studied. Fig. 5.4 shows the Young's modulus of the simulated deposit increasing with decreasing particle size. This could be as a result of increase in surface energy with decreasing particle size. In a study of influence of grain size on Young's modulus, a decrease in grain size led to an increase in grain boundary defects, which ultimately resulted in a decrease in Young's modulus.<sup>70</sup> However, Dinreville et al.<sup>71</sup> showed that the effect of surface energy on the elastic behavior becomes more significant when one of the dimensions is below 10 nm. The result of our study is comparable to the results of Dinreville et al.'s study because our simulated films are made up of particles and not grains. A reasonable explanation is that grain boundaries affect materials composed of grains, while surface energy affects materials composed of particles.

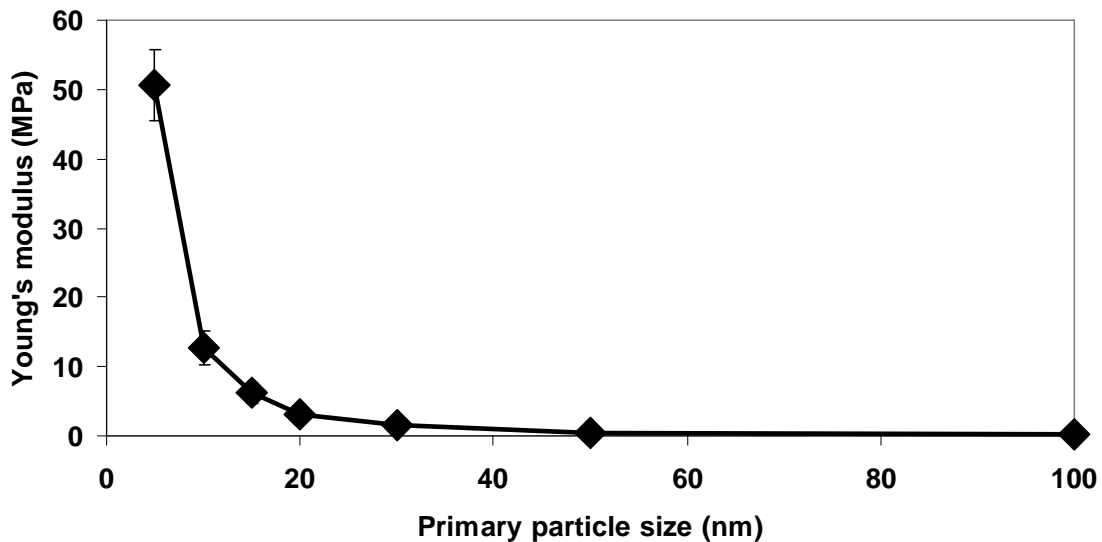


**Fig. 5.4.** Influence of primary particle size on Young's modulus.

However, our results show that aggregate size does not seem to have an effect on Young's modulus as illustrated in Fig. 5.5.

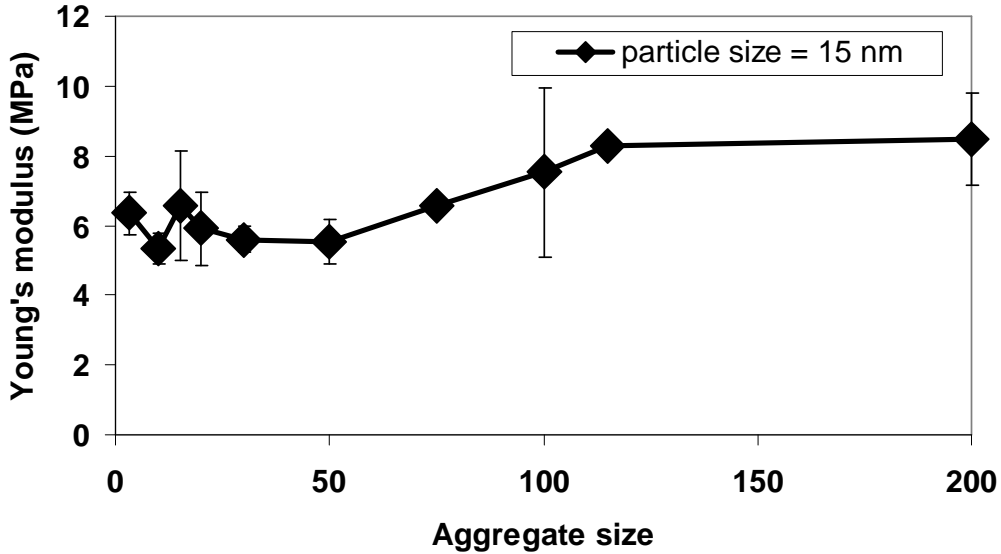
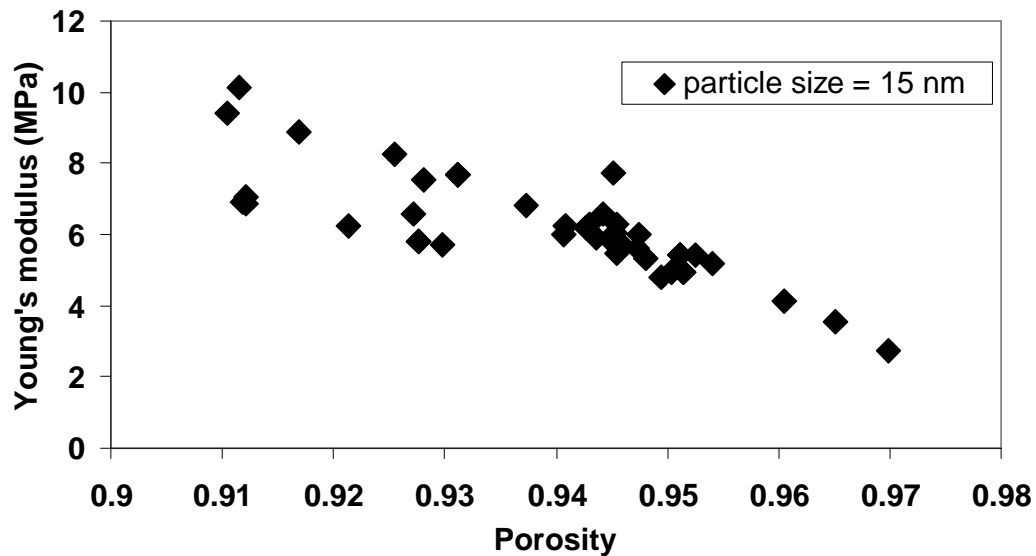


Fig. 5.5. Influence of aggregate size on Young's modulus.

This is perplexing, as it would be expected that increasing aggregate size would increase the chemical bonds in the deposit. It could be that the aggregate sizes considered were not large enough. Comparing the number of particles that could possibly be in an experimentally generated aggregate (from the films synthesized experimentally) to a simulated aggregate, it is 3 orders of magnitude larger. Young's modulus of the deposits decreased with porosity reduction as shown in Fig. 5.6.



**Fig. 5.6.** Influence of porosity on Young's modulus.

Experimental<sup>95; 96</sup> and theoretical reports<sup>83; 97</sup> in the literature indicate that the Young's modulus of a material reduces with increasing porosity. This makes sense as an increase in porosity corresponds to a decrease in total bond strength per volume resulting from a decrease in material.<sup>97</sup> This leads ultimately to a decrease in the Young's modulus.

Simulations were performed for the bonds being all chemical and all van der Waals. This was to see effect of both ends of the bond strength on Young's modulus. Young's modulus calculated was 3.01 MPa and 57.4 MPa for all van der Waals and all chemical bonds respectively. This is an indication that any dramatic increase in Young's modulus to the range of GPa will have to be by drastically densifying the film, which will also have the negative effect of losing surface area.

## 5.6 Summary

Aggregates were simulated via monomer-cluster diffusion limited aggregation. The simulated aggregates were deposited via Monte Carlo and a continuum method was applied to the resulting nanoparticle deposit to predict the Young's modulus of the deposit. Young's modulus of titania nanoparticle deposit of particles 17 nm in diameter and aggregate size of 15 particles was 3.5 MPa, comparable to experimental results for Young's modulus of titania nanoparticle deposits with similar parameters. Increasing particle size of nanoparticle deposit resulted in a decrease in Young's modulus. However, aggregate size had no noticeable effect on the Young's modulus. Decreasing porosity resulted in an increase in Young's modulus as expected from results reported previously in the literature. The results of this work indicate the importance of structure (primary particle size and porosity) on macroscale properties such as Young's modulus.

## **CHAPTER 6: CONCLUSIONS AND RECOMMENDATIONS FOR FUTURE WORK**

### **6.1 Conclusions**

A hybrid process based upon gas-to-particle conversion and particle precipitated chemical vapor deposition was used to synthesize deposits of titania nanoparticle aggregates. The residence time of particles in the reactor was varied and the influence was studied in relationship to particle morphology and mechanical properties. Increase in residence time was shown to result in increase in primary particle diameter but indifferent to aggregate diameter. This was interpreted to be because the nanoparticles within each initial aggregate coalesce and grow. The mass of each aggregate is still conserved, because of the low frequency of collisions between aggregates, resulting in a nearly constant aggregate electrical mobility diameter as measured with a differential mobility analyzer and a condensation particle counter. The Young's modulus is shown to increase with a decrease in the primary particle diameter.

A study of the effect of post processing annealing on the particle morphology and mechanical properties was conducted. Annealing was chosen to increase the interconnectivity of nanoparticles within the deposit by replacement of van der Waals

bonds with chemical bonds and enhancing of old chemical bonds. Increasing the annealing temperature resulted in particle growth at different temperatures and aggregate growth only at the highest temperature studied. The Young's modulus, however, shows only an influence of aggregate diameter and porosity. The annealing is proposed to cause particle growth within each aggregate, leading to collapse of the deposit network. The amount of collapse is related to the porosity change, which increases at the highest annealing temperature. After collapse of the network, particles from different aggregates are able to connect via chemical bond and thus increase the aggregate diameter as measured by dynamic light scattering. Only the highest annealing temperature studied showed an increase in aggregate diameter and an increase in Young's modulus and hardness.

The results of the study on synthesized films shows Young's modulus increases with a decrease in primary particle diameter. The annealing post processing study shows Young's modulus increases with aggregate diameter. The results are conflicting. We interpreted this to be that each diameter has a more dominant effect on the Young's modulus at different regimes. Primary particle diameter has been known to have a more pronounced effect below 15 nm,<sup>71</sup> and this is why primary particle diameter was not seen to have any effect in the annealing study. To better understand the effect of change in primary particle and aggregate diameters on Young's modulus, Monte Carlo and continuum methods were employed. A Monte Carlo method was used to simulate nanoparticle aggregate deposits and a finite element method was used to calculate the Young's modulus from strain energy of the deposits simulated. The results of the computational study indicate that a decrease in

primary particle diameter increases the Young's modulus, especially below 15 nm. Aggregate size was not seen to have any effect. This may be because the aggregate sizes simulated were not large enough to see any significant effect on Young's modulus. Porosity was also shown to have an influence on Young's modulus; increase in porosity decreased the Young's modulus. This is reasonable as there is a reduction in amount of chemical bonds/material per volume and hence a decrease in Young's modulus.

Our work shows that Young's modulus of a film made up of nanoparticle aggregates is mainly influenced by the primary particle diameter. Aggregate size affects the packing of particles within a deposit which ultimately affects the Young's modulus via porosity, as shown in the annealing studies. Aggregate diameter has an effect when the primary particle diameter is not an important factor, which is after 15 nm.

## 6.2 Recommendations for future work

Thermophoresis has been the basis of particle deposition on the silicon wafer. Using an electric field may generate aggregates that are structurally different from those synthesized in our work. The aggregates could be more chain like and therefore affect the mechanical properties of the porous film. It would be interesting to see how aggregate structure influences the Young's modulus of the porous films. A dynamic mechanical analyzer could also be used as a complimentary technique to estimate Young's modulus of the films.

Post processing could also be done on the films at lower temperatures to conserve surface area while making the films stronger. Chemical condensation of titania vapor between the particles would increase the necking between particles within each aggregate and replace the van der Waals bonds, between particles of different aggregates, with chemical bonds. This would slightly reduce the surface area and increase the strength as opposed to the annealing, which lead to a large loss in surface area in exchange for an increase in the mechanical strength.

In the simulation work, aggregates size could be increased much more than has been considered. This would drastically increase the computation time. However, it would clarify the effect of aggregate size on the Young's modulus. Aggregates that are more chain like could also be simulated to study the influence of aggregate compactness on the Young's modulus. This model could also serve as a base to simulate nano wires (essentially short nano chains) and to predict the Young's modulus of films made up of nano wires.

## APPENDICES

### APPENDIX A: Supplementary Experimental Information

#### A1: Operating procedures

Standard Operating Procedures for  
Modern Particle Precipitate Chemical Vapor Deposition Reactor  
**Place: Building 090 Room # 1127**

0 hr

1. Turn on Chiller. (Set to 15 degrees C)
2. Weigh substrate.
3. Load substrate onto cold stem.

0.5 hr

4. Turn on furnace.

4.5 hrs

5. Raise cold stem to desired height of 19 inches.
6. Now set chiller to 0 degrees C
7. Fill liquid nitrogen cold trap.

4.75 hrs

9. Turn on Oxygen dilution stream, and set to 1 L/min.
10. Turn on heating tape.

5 hrs

11. Turn on argon carrier gas, set flowmeter to 50.
12. Open valve at the exit stream of the bubbler.
13. Open valve at the entrance to the bubbler.

7 hrs

14. Refill liquid nitrogen cold trap.

9 hrs

15. Turn off furnace.
16. Close valve at entrance to bubbler.
17. Close valve at exit of bubbler.
18. Turn off argon carrier gas.
19. Turn off heating tape.
20. Lower cold stem.

9.25 hrs

21. Turn off Oxygen dilution stream.

9.5 hrs

22. Turn off chiller.

Next day

23. Remove substrate.
24. Scrap cold stem.
25. Clean cold stem.
26. Weigh substrate.

Note: Periodically record readings on various meters throughout experiment, and also monitor flow rates and temperatures.

Safety concerns: TTIP in bubbler very moisture sensitive; turn off furnace power switch, close bubbler valves, close oxygen and nitrogen valves if any problem occurs.

## A2: Reactor kinetics

Distance from quartz tube entrance (cm)	Temperature (°C)	Reaction time (secs)	Residence time (secs)
0	324	17.09	0
7.62	456	1.307	2.495
15.24	680	0.085	4.404
22.86	745	0.048	6.190
30.48	807	0.030	7.875
38.10	829	0.026	9.525
45.72	829	0.026	11.18
53.34	814	0.028	12.85
60.96	785	0.035	14.57
68.58	734	0.053	16.37
76.20	599	0.194	18.46
83.82	427	2.115	21.06
91.44	275	60.80	24.38
99.06	139	10019	28.79

$$t_{reaction} = \frac{-\ln \frac{C_o}{C_i}}{k} \quad (A2.1)$$

$$t_{residence} = \frac{L}{v_{gas}} \quad (A2.2)$$

where R is gas constant, T is temperature, L is distance in quartz tube,  $v_{\text{gas}}$  is gas flow rate (cm/min) and k, the rate constant for TTIP thermal decomposition, is given by

$$k = 3.96 \times 10^5 \exp\left(-\frac{70500}{RT}\right) \quad (\text{A2.3})$$

Gas viscosity values are tabulated below:

---

---

<b>Temperature (°C)</b>	<b>Viscosity (Kgm<sup>-1</sup>s<sup>-1</sup>)</b>
177	$2.8 \times 10^{-5}$
430	$3.8 \times 10^{-5}$
599	$4.4 \times 10^{-5}$
710	$4.7 \times 10^{-5}$

---

---

**A3: Titanium dioxide diffraction pattern<sup>62</sup>**

<b>ANATASE</b>	<b>ANATASE</b>	<b>RUTILE</b>	<b>RUTILE</b>
<b>d spacing</b>	<b>Intensity (%)</b>	<b>d spacing</b>	<b>Intensity (%)</b>
3.52	100	3.247	100
2.431	10	2.487	50
2.378	20	2.297	8
2.332	10	2.188	25
1.892	35	2.054	10
1.6999	20	1.6874	60
1.6665	20	1.6237	20

## **APPENDIX B: Procedures for characterization**

### **B1: Brunauer-Emmett-Teller Method (BET)**

Quantachrome Nova 1200

Note: The operation of this device is fairly straightforward as the accompanying software is very menu-driven. Hit the ESC key to go back to a previous menu. Also, finger-tightening of the fittings is sufficient to maintain vacuum in the apparatus. When tightening/untightening fittings, make sure that the o-rings are accounted for! Finally, the manual suggests that a measured surface area between 2 to 50 m<sup>2</sup> is necessary for an accurate result.

#### 1. START UP

##### A. Preparation

- a. Get liquid nitrogen!
- b. Wash the sampling tubes and dry them in a furnace.
- c. Determine the weight of the sample by weight-by-difference.

#### 2. OPERATION

##### A. Degas the sample.

- a. Wrap sample with heating mantle.

Note: For applications in this work, through experience, degassing for 30 min is sufficient as results are consistent with results from samples degassed for 3 hr, the time recommended in the manual.

Furthermore, a degassing temperature of 373 K is the minimum temperature required for removing water vapor within the sample.

B. Activate the gas adsorption.

a. Fill dewar with liquid nitrogen to the red line.

Note: Menu options are as follows.

Tube selection: 01 = small, 66 = big

BET: 01 = 6 pt, 02 = 3 pt

### 3. SHUTDOWN

A. Shutdown.

a. Reverse order of start up.

## **B2: Fourier Transform Infrared Spectroscopy (FTIR)**

Nicolet 550 Series II

OMNIC Software

### 1. OPERATION

A. Data collection setup.

Note: Make sure “N-B strong” is selected.

B. Optical bench setup.

Note: Take the difference between the “min” and “max” velocity. The absolute value of the difference should be approximately less than 8.

C. Collect the background.

D. Collect the sample.

### **B3: Transmission Electron Microscopy (TEM)**

Hitachi 600AB

#### **1. START UP**

A. Start up.

a. Insert sample.

Note: Flip the EVAC/AIR switch for 3 cycles to ensure good vacuum!

b. Power up the accelerating voltage.

Note: Check voltage stability! If the voltage is unstable, hold at 75 kV for a few minutes, and then proceed.

c. Power up the filament.

Note: Check voltage stability!

#### **2. BEAM ALIGNMENT**

A. Gun (filament) alignment.

- a. Converge beam with BRIGHTNESS button.
- b. Use GUN TILT knobs (left side of control panel) to make the “lighting” symmetric around the filament “shadow.”

B. Horizontal alignment.

- a. Use FUNCTION and DATA SET buttons to change spot size.
- b. 0.4  $\mu\text{m}$ : Center with BRIGHTNESS CENTERING button.
- c. 1  $\mu\text{m}$ : Converge beam with BRIGHTNESS button and center with GUN HOIRZ (left side of control panel) knob.
- d. Repeat steps a. to c. as necessary until the beam is centered with both spot sizes.

C. First condenser lens aperture alignment.

- a. Spread beam until its diameter touches the “rectangular” marker.
- b. Center with x & y alignment knobs on the aperture.

D. Astigmatism correction.

- a. Use COND STIGM knobs to achieve a circular beam spot.

E. Insert sample.

F. Height alignment.

Note: Experience suggests that this step is not necessary for improving the image quality of the samples observed in this work.

G. Objective lens alignment.

Note: Use current centering or high voltage centering methods.

Experience suggests that this step is not necessary for improving the image quality of samples observed in this work.

### 3. SHUTDOWN

#### A. Shutdown.

- a. Reverse order of start up.

### 4. ELECTRON DIFFRACTION

#### A. Dark field image procedure.

- a. Align horizontally three spots: one is “weak”, one is “strong”, and one is the transmitted beam.
- b. Use BEAM TILT button to move and BEAM HORIZ to converge (equivalent effect as BRIGHTNESS button in normal field operation) to move “weak” spot to transmitted spot.
- c. Use pedals to tilt the sample and focus the diffraction pattern.

### 5. PHOTOGRAPHY

#### A. Developing negatives.

- a. Wash negative in developer (~ 1 min).
- b. Wash negatives with water (~ few sec).
- c. Wash negatives in fixer (~ 10 min).
- d. Wash negatives in running water (~ 10 min).

e. Dry in oven (~ 25 min).

**B. Developing film.**

a. Put negative in holder with film number positioned at the bottom right.

b. Use hand-held meter determine exposure time.

c. Set exposure time.

d. Wash film in developer (~ 1 min).

e. Wash film with water (~ few sec).

f. Wash film in fixer (~ 10 min).

g. Wash film in running water (~ 10 min).

h. Put film on conveyor dryer.

**B4: Dynamic Light Scattering (DLS)**

Photocor-FC

1. Prepare samples by diluting a small amount of material in 4 ml of water and sonocating for one hour.
2. Turn on instrument laser.
3. Put sample vial in sample holder.
4. Take measurements every 30-60 seconds.

## **B5: Differential Mobility Analyzer and Condensation Particle Counter**

The Differential Mobility Analyzer (DMA) separates particles based on their electrical mobility. The DMA is made up of two concentric cylinders, inlet exit and outlet exit. Voltage is applied to the inner cylinder to create an electric field. A small stream of the generated particles will be electrically charged before entrance into DMA by ions from a radioactive Kr-85 source. Not all the particles are charged, but only the positive charged ones are used. It is mixed with a flow of air before entrance into the DMA; this is to dilute the particle stream and prevent further coagulation. A narrow range of the particles is then selected by their electrical mobility by varying the voltage applied to the inner cylinder. The diameter of the particles selected is calculated from the equation below

$$Z = eC/3\pi\mu d \quad \text{B5.1}$$

where  $Z$  is the electrical mobility,  $e$  is the charge on the electron,  $C$  is the slip correction factor,  $\mu$  is the air viscosity and  $d$  is the particle diameter. Particles of a given mobility would be of the same size if they have the same charge. The selected range passes through the outlet exit to the Condensation Particle Counter (CPC). The CPC counts the particles by condensing water or alcohol on the particles to make them large enough to be scattered by light. A detector in the CPC detects and counts the number of times a beam of light is scattered. This number gives the concentration of the particles in the selected range from the DMA. This is done repeatedly until a large range of particle size is covered, thereby getting the size distribution of the generated particles.

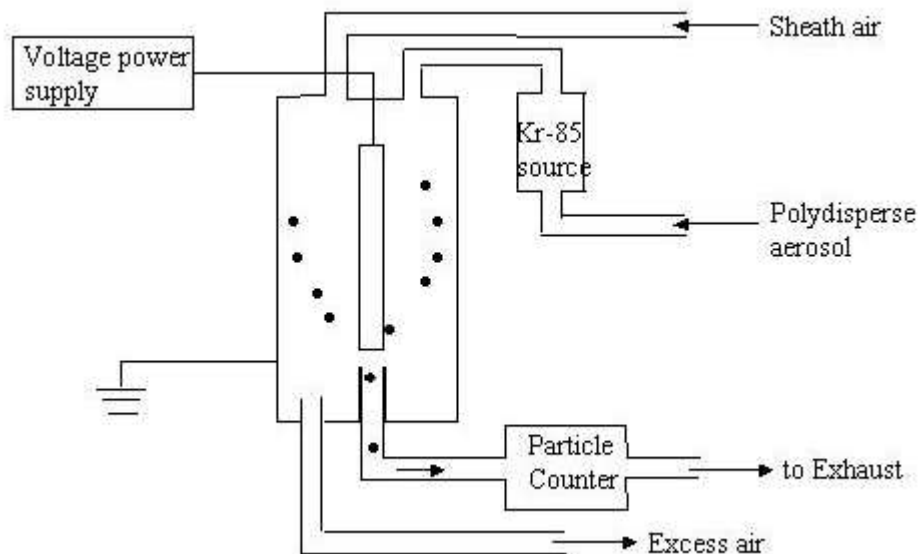


**Figure B5.1.** DMA and CPC configuration.

#### TSI Model 3081 and TSI Model 3022A

1. Turn on TSI Model 3022A (CPC) and TSI Model 3081 (DMA).
2. Connect Aerosol stream (from reactor) to polydisperse inlet of DMA.
3. Connect monodisperse outlet of DMA to CPC inlet.
4. Connect an HEPA filter to sheath air flow inlet of DMA.
5. Insert a critical orifice into the tubing connected to the vacuum pump.
6. Connect the excess air flow outlet of DMA to a vacuum pump.
7. Change the CPC to be used in high flow.
8. Attach a Y connector before the CPC inlet, then connect the DMA monodisperse outlet and a HEPA filter to the short ends of the Y connector in front of the CPC.
9. Balance flows using a ratio of 10: 1 for the sheath air flow rate to the polydisperse air flow rate. The critical orifice would pull out the same amount of flow as the sheath air by setting the rotameter of the sheath air to the critical orifice flow rate.

10. The polydisperse pressure gauge is set to pull in one tenth of the sheath air flow rate.
11. By mass balance, the flow rate of the monodisperse out would be equal to the polydisperse flow rate.
12. After flow balancing, the voltage knob is rotated to different voltages and the particle count on the CPC is written down.
13. The corresponding particle mobility diameters are calculated from the voltages.

## **APPENDIX C: Supplementary Computational Information**

### **C1: Simulation process**

#### **Deposit simulation**

1. Enter # of particles to be simulated (j)
2. Enter simulation step of particle (d)
3. Enter diameter of particle (particle)
4. Enter aggregate size (rn2)
5. Enter seed1, seed2, seeda, seedb, seedc, seedd, seed3, seed4, seedd2
6. Type report.txt
7. Type data1.txt
8. Type data2.txt
9. Type data3.txt
10. Type data4.txt
11. Type data5.txt
12. Type data6.txt

File > close workspace > yes

File > open workspace > double click on density file > click on density.mdp > ok

#### **Density and strain energy calculation**

13. Check report.txt on desk top for last particle #

14. Enter simulation step of particles
15. Enter “rn”
16. Enter “rnn”
17. Enter “s”
18. Enter dimension LL1 of box in x direction
19. Enter dimension LL2 of box in x direction
20. Enter dimension LL3 of box in z direction
21. Enter dimension LL4 of box in z direction
22. Enter dimension LL5 of box in y direction
23. Enter dimension rr of box in y direction
24. Write down results generated

## **C2: Deposit simulation source code in FORTRAN programming language**

### **! Program Nanoparticle MonteCarlo Simulation**

!Program to simulate the deposit morphology of nanoparticle aggregates deposit.  
!Particles are randomly generated and randomly moved till they attach to another particle/substrate.

!Definitions of some variables used are:

!ran2: random number generator function

!Theta: angle used in direction of particle movement, in radians

!ranout: direct output from random number generator function "ran2" for x positions

!APART: distance between 2 particles, calculated with formula of distance between 2 points which in this case is the center of the particles

!seed1: seed for random number generated for x position of particles

!seed2: seed for random number generated for z position of particles

!xPos(i): incoming particle x position

!yPos(i): incoming particle y position

!zPos(i): incoming particle z position

!xPos(k): deposited particles x position

!yPos(k): deposited particles y position

!zPos(k): deposited particles z position

!l : number of particles for substrate film

!j : Total number of particles simulated, includes substrate particles

!d : diameter of particle

!r : radius of particle

## PROGRAM Nanoparticle\_MC\_Simulation

USE PORTLIB, ONLY: ETIME

IMPLICIT NONE

```
REAL :: d, ran2, ranout1,
ranout2, ab1, ab, ab2, abb, avgCN, totalH, Rg, totalaggH, aggRg, avgCoN
REAL :: coordinationN,
coordnumber, averageCN1, averageCN2, totalCN, coordDist
REAL :: XXcg, YYcg, ZZcg, Xcg, Ycg,
Zcg, X1cg, Y1cg, Z1cg, Xattach, Yattach, Zattach
REAL :: E1, V, dist1, dist2, dist4, dist5, cosAngle, StrainEnergy, CE
REAL :: E2, E3, d12, AA5, AA6, db, rb, ainitial3, ainitial4
REAL :: achem, ac, axc, aoc, mc, cc, dist1c, dist2c, dist3ac, dist3bc, dist4c, dist5c
REAL :: distance4, a, HA, dp, ao, ax, strain, xy, xyy, AA7, AA8, d13
REAL :: AA1, AA2, AA3, AA4, da, ra, ainitial1, ainitial2, dist3a, dist3b
REAL :: RandomAngle1, RandomAngle2, Theta1, Theta2
REAL :: r, particle, aggl, agglb, mm3, abc, AP1, AP2, APART, stepsize, distance1,
distance2, distance3
REAL :: X3, Y3, Z3, X4, Y4, Z4, XX, YY, ZZ, distance8
REAL :: xmax, xmin, zmax, zmin, xadd, xsub, zadd, zsub
INTEGER ::
rn1, rn2, seeda, seedb, seedc, seedd, seedd2, mm1, mm2, mm, agglpos, agg, ag, g
INTEGER :: seed3, seed4, num, ii, m, range
INTEGER :: f, l, b, b1, b2, b3, b4, b5, b6, j, i, k, n, OpenStatus, seed1, seed2, collision, kk
REAL, DIMENSION(1000000) :: xPos, yPos, zPos
REAL, DIMENSION(600000) :: Eche, Van2, Evdw, SE, Eche1, Eche2, Eche3
REAL, DIMENSION(600000) :: h, chenum, coord, h1, aggche
INTEGER :: cnum, iii, nnn, aggnum, iagg, agn, totalvdwbonds, totalchebonds
INTEGER, DIMENSION(600000) :: che, vdw
```

```
OPEN (UNIT = 12, FILE = "REPORT.txt", STATUS = "NEW", &
ACTION = "WRITE", IOSTAT = OpenStatus)
OPEN (UNIT = 13, FILE = "data1.txt", STATUS = "NEW", &
ACTION = "WRITE", IOSTAT = OpenStatus)
OPEN (UNIT = 14, FILE = "data2.txt", STATUS = "NEW", &
ACTION = "WRITE", IOSTAT = OpenStatus)
OPEN (UNIT = 15, FILE = "data3.txt", STATUS = "NEW", &
ACTION = "WRITE", IOSTAT = OpenStatus)
OPEN (UNIT = 16, FILE = "data4.txt", STATUS = "NEW", &
ACTION = "WRITE", IOSTAT = OpenStatus)
OPEN (UNIT = 17, FILE = "data5.txt", STATUS = "NEW", &
ACTION = "WRITE", IOSTAT = OpenStatus)
OPEN (UNIT = 18, FILE = "data6.txt", STATUS = "NEW", &
ACTION = "WRITE", IOSTAT = OpenStatus)
```

```
PRINT *, "Enter # of particles to be simulated"  
READ *, j
```

!SUBSTRATE PARTICLE GENERATION: substrate particles are made to cover the  
entire grid at  $y = 0$

```
PRINT *, "Enter simulation step of particle"  
READ *, d
```

```
PRINT *, "Enter diameter of particle"  
READ *, particle
```

```
PRINT *, "Enter aggregate size"  
READ *, m2
```

```
b = INT(4.0/ d)  
r = d/2
```

```
b1 = 2  
b2 = b+2
```

```
DO f = b1, b2  
xPos(1) = -1.6  
yPos(1) = 0.0  
zPos(1) = -1.6
```

```
xPos(f) = xPos(f-1) + d  
yPos(f) = 0.0  
zPos(f) = -1.6  
END DO
```

```
b3 = b2+1  
b4 = b2+b+1
```

```

DO WHILE (.true.)
    b5 = ((b+2)**2 )
    b6 = b5+2

    DO 1 = b3, b4
        xPos(1) = xPos(1- b-2)
        yPos(1) = yPos(1- b-2)
        zPos(1) = zPos(1- b-2)+d
    END DO
    b3 = b4+1
    b4 = b4+b+1

    IF (b4>b6) THEN
        EXIT
    END IF

END DO

b4 = b4-b-1

```

### **!GENERATION OF PARTICLE FOR DEPOSITION**

```

Write (*, *) 'Enter seed1 for random number generator:'
Read (*, *) seed1
Write (*, *) 'Enter seed2 for random number generator:'
Read (*, *) seed2
Write (*, *) 'Enter seeda for random number generator:'
Read (*, *) seeda
Write (*, *) 'Enter seedb for random number generator:'
Read (*, *) seedb
Write (*, *) 'Enter seedc for random number generator:'
Read (*, *) seedc
Write (*, *) 'Enter seedd for random number generator:'
Read (*, *) seedd
Write (*, *) 'Enter seed3 for random number generator:'
Read (*, *) seed3
Write (*, *) 'Enter seed4 for random number generator:'
Read (*, *) seed4
Write (*, *) 'Enter seedd2 for random number generator:'
Read (*, *) seedd2

```

```
rn1 = b4+1
```

```
DO WHILE (.true.)
```

```
  aggla = ran2(seeda)
```

```
  agglb = aggla*11
```

```
  !1st particle in aggregate generated
```

```
  ranout1 = -1.6 + 4*ran2(seed1)
```

```
  ranout2 = -1.6 + 4*ran2(seed2)
```

```
  xPos(rn1) = ranout1
```

```
  yPos(rn1) = 5
```

```
  zPos(rn1) = ranout2
```

```
  ! In the loop below, the particle generated will keep on moving and checking  
  ! for out of bound and collision
```

```
  dp = particle*1E-9
```

```
  HA = 164.9E-21
```

```
  strain = 0.01
```

```
  ainitial3 = 0.1E-9
```

```
  ainitial4 = (d* ainitial3)/dp
```

```
  db = d + ainitial4
```

```
  rb = db/2
```

```
DO i = rn1+1, rn1+rn2-1
```

```
totalCN = 0
```

```
  DO iii = rn1, i-1
```

```
    coord(iii)= 0
```

```
      DO nnn = rn1, i-1
```

```
        coordDist =
```

```
        Dist(xPos(iii),xPos(nnn),yPos(iii),yPos(nnn),zPos(iii),zPos(nnn))
```

```
        IF (ABS(coordDist - db) < 0.0001) THEN
```

```
          coord(iii) = coord(iii) + 1
```

```
        END IF
```

```
      END DO
```

```
totalCN = totalCN + coord(iii)
END DO
```

```
averageCN1 = totalCN/(i-rn1)
```

**!Random choosing of particle to attach to**

```
DO WHILE (.true.)
```

```
mm1 = i
```

```
mm2 = rn1
```

```
abc = ran2(seedb)
```

```
mm3 = (i - rn1)*abc
```

```
mm = rn1 + INT(mm3)
```

```
averageCN2 = (totalCN + 1)/(i - rn1 + 1)
```

```
IF (averageCN2 <= 3.0) THEN
```

```
EXIT
```

```
END IF
```

```
END DO
```

```
AP1= ran2(seedc)
```

```
AP2= 24* AP1
```

```
agglpos = 1 + INT(AP2)
```

```
ab1 = ran2(seedd)
```

```
ab2 = ran2(seedd2)
```

```
ab = ab1*r
```

```
abb = ab2*r
```

**!attachment form chosen**

```
IF (agglpos == 1) THEN
```

```
  xPos(i) = xPos(mm) - ab
```

```
  yPos(i) = yPos(mm) - abb
```

```
  zPos(i) = zPos(mm) + SQRT((db**2) - ((yPos(i)-yPos(mm))**2) -  
  ((xPos(i)-xPos(mm))**2))
```

```
ELSE IF (agglpos == 2) THEN
```

```
  xPos(i) = xPos(mm) + ab
```

```

        yPos(i) = yPos(mm) - abb
        zPos(i) = zPos(mm) + SQRT((db**2) - ((yPos(i)-yPos(mm))**2) -
        ((xPos(i)-xPos(mm))**2))
ELSE IF (agglpos == 3) THEN
        xPos(i) = xPos(mm) - ab
        yPos(i) = yPos(mm) + abb
        zPos(i) = zPos(mm) + SQRT((db**2) - ((yPos(i)-yPos(mm))**2) -
        ((xPos(i)-xPos(mm))**2))
ELSE IF (agglpos == 4) THEN
        xPos(i) = xPos(mm) + ab
        yPos(i) = yPos(mm) + abb
        zPos(i) = zPos(mm) + SQRT((db**2) - ((yPos(i)-yPos(mm))**2) -
        ((xPos(i)-xPos(mm))**2))
ELSE IF (agglpos == 5) THEN
        xPos(i) = xPos(mm) - abb
        yPos(i) = yPos(mm) - ab
        zPos(i) = zPos(mm) + SQRT((db**2) - ((yPos(i)-yPos(mm))**2) -
        ((xPos(i)-xPos(mm))**2))
ELSE IF (agglpos == 6) THEN
        xPos(i) = xPos(mm) - abb
        yPos(i) = yPos(mm) + ab
        zPos(i) = zPos(mm) + SQRT((db**2) - ((yPos(i)-yPos(mm))**2) -
        ((xPos(i)-xPos(mm))**2))
ELSE IF (agglpos == 7) THEN
        xPos(i) = xPos(mm) + abb
        yPos(i) = yPos(mm) - ab
        zPos(i) = zPos(mm) + SQRT((db**2) - ((yPos(i)-yPos(mm))**2) -
        ((xPos(i)-xPos(mm))**2))
ELSE IF (agglpos == 8) THEN
        xPos(i) = xPos(mm) + abb
        yPos(i) = yPos(mm) + ab
        zPos(i) = zPos(mm) + SQRT((db**2) - ((yPos(i)-yPos(mm))**2) -
        ((xPos(i)-xPos(mm))**2))
ELSE IF (agglpos == 9) THEN
        xPos(i) = xPos(mm) - ab
        zPos(i) = zPos(mm) - abb
        yPos(i) = yPos(mm) + SQRT((db**2) - ((xPos(i)-xPos(mm))**2) -
        ((zPos(i)-zPos(mm))**2))
ELSE IF (agglpos == 10) THEN
        xPos(i) = xPos(mm) + ab
        zPos(i) = zPos(mm) - abb
        yPos(i) = yPos(mm) + SQRT((db**2) - ((xPos(i)-xPos(mm))**2) -
        ((zPos(i)-zPos(mm))**2))
ELSE IF (agglpos == 11) THEN
        xPos(i) = xPos(mm) - ab
        zPos(i) = zPos(mm) + abb

```

```

        yPos(i) = yPos(mm) + SQRT((db**2) - ((xPos(i)-xPos(mm))**2) -
        ((zPos(i)-zPos(mm))**2))
ELSE IF (agglpos == 12) THEN
        xPos(i) = xPos(mm) + ab
        zPos(i) = zPos(mm) + abb
        yPos(i) = yPos(mm) + SQRT((db**2) - ((xPos(i)-xPos(mm))**2) -
        ((zPos(i)-zPos(mm))**2))
ELSE IF (agglpos == 13) THEN
        xPos(i) = xPos(mm) - abb
        zPos(i) = zPos(mm) - ab
        yPos(i) = yPos(mm) + SQRT((db**2) - ((xPos(i)-xPos(mm))**2) -
        ((zPos(i)-zPos(mm))**2))
ELSE IF (agglpos == 14) THEN
        xPos(i) = xPos(mm) - abb
        zPos(i) = zPos(mm) + ab
        yPos(i) = yPos(mm) + SQRT((db**2) - ((xPos(i)-xPos(mm))**2) -
        ((zPos(i)-zPos(mm))**2))
ELSE IF (agglpos == 15) THEN
        xPos(i) = xPos(mm) + abb
        zPos(i) = zPos(mm) - ab
        yPos(i) = yPos(mm) + SQRT((db**2) - ((xPos(i)-xPos(mm))**2) -
        ((zPos(i)-zPos(mm))**2))
ELSE IF (agglpos == 16) THEN
        xPos(i) = xPos(mm) + abb
        zPos(i) = zPos(mm) + ab
        yPos(i) = yPos(mm) + SQRT((db**2) - ((xPos(i)-xPos(mm))**2) -
        ((zPos(i)-zPos(mm))**2))
ELSE IF (agglpos == 17) THEN
        yPos(i) = yPos(mm) + abb
        zPos(i) = zPos(mm) + ab
        xPos(i) = xPos(mm) + SQRT((db**2) - ((yPos(i)-yPos(mm))**2) -
        ((zPos(i)-zPos(mm))**2))
ELSE IF (agglpos == 18) THEN
        yPos(i) = yPos(mm) + abb
        zPos(i) = zPos(mm) + ab
        xPos(i) = xPos(mm) + SQRT((db**2) - ((yPos(i)-yPos(mm))**2) -
        ((zPos(i)-zPos(mm))**2))
ELSE IF (agglpos == 19) THEN
        yPos(i) = yPos(mm) + abb
        zPos(i) = zPos(mm) + ab
        xPos(i) = xPos(mm) + SQRT((db**2) - ((yPos(i)-yPos(mm))**2) -
        ((zPos(i)-zPos(mm))**2))
ELSE IF (agglpos == 20) THEN
        yPos(i) = yPos(mm) + abb
        zPos(i) = zPos(mm) + ab

```

```

        xPos(i) = xPos(mm) + SQRT((db**2) - ((yPos(i)-yPos(mm))**2) -
        ((zPos(i)-zPos(mm))**2))
ELSE IF (agglpos == 21) THEN
        yPos(i) = yPos(mm) + abb
        zPos(i) = zPos(mm) + ab
        xPos(i) = xPos(mm) + SQRT((db**2) - ((yPos(i)-yPos(mm))**2) -
        ((zPos(i)-zPos(mm))**2))
ELSE IF (agglpos == 22) THEN
        yPos(i) = yPos(mm) + abb
        zPos(i) = zPos(mm) + ab
        xPos(i) = xPos(mm) + SQRT((db**2) - ((yPos(i)-yPos(mm))**2) -
        ((zPos(i)-zPos(mm))**2))
ELSE IF (agglpos == 23) THEN
        yPos(i) = yPos(mm) + abb
        zPos(i) = zPos(mm) + ab
        xPos(i) = xPos(mm) + SQRT((db**2) - ((yPos(i)-yPos(mm))**2) -
        ((zPos(i)-zPos(mm))**2))
ELSE IF (agglpos == 24) THEN
        yPos(i) = yPos(mm) + abb
        zPos(i) = zPos(mm) + ab
        xPos(i) = xPos(mm) + SQRT((db**2) - ((yPos(i)-yPos(mm))**2) -
        ((zPos(i)-zPos(mm))**2))

END IF

```

**!Making sure particles in aggregate do not overlap**

```

DO g = 1, 1
DO ag = rn1, i-1
        distance1 = Dist(xPos(i), xPos(ag), yPos(i), yPos(ag), zPos(i), zPos(ag))
        IF (distance1 <= db) THEN
                CALL SOLVE(xPos(i), xPos(ag), yPos(i), yPos(ag), zPos(i), zPos(ag), rb)
                distance2 = Dist(xPos(i), xPos(ag), yPos(i), yPos(ag), zPos(i), zPos(ag))
                END IF
END DO
END DO

```

```

Xattach = 0
Yattach = 0
Zattach = 0
coordnumber = 0

```

```

DO aggnum = rn1, i
aggche(aggnum) = 0
DO agn = rn1, i
distance8 = Dist(xPos(aggnum), xPos(agn), yPos(aggnum), yPos(agn),
zPos(aggnum), zPos(agn))
IF (ABS(distance8 - db) < 0.0001) THEN
aggche(aggnum) = aggche(aggnum) + 1
END IF
END DO
Xattach = Xattach + xPos(aggnum)
Yattach = Yattach + yPos(aggnum)
Zattach = Zattach + zPos(aggnum)
coordnumber = coordnumber + aggche(aggnum)
END DO

```

```

avgCoN = coordnumber/(i-rn1+1)
X1cg = Xattach / (i-rn1+1)
Y1cg = Yattach / (i-rn1+1)
Z1cg = Zattach / (i-rn1+1)

```

```

totalaggH = 0
DO iagg = rn1, i
h1(iagg) = 1*(Dist(xPos(iagg), X1cg, yPos(iagg), Y1cg, zPos(iagg),
Z1cg))
totalaggH = totalaggH + (h1(iagg))**2
END DO

```

```

aggRg = (totalaggH/(i-rn1+1))**0.5 !Radius of gyration of growing aggregate

```

```

END DO

```

```

XXcg = 0
YYcg = 0
ZZcg = 0
coordinationN = 0

```

```

DO cnum = rn1, rn1+rn2-1
chenum(cnum) = 0
DO n = rn1, rn1+rn2-1
distance8 = Dist(xPos(cnum), xPos(n), yPos(cnum), yPos(n),
zPos(cnum), zPos(n))

```

```

                IF (ABS(distance8 - db) < 0.0001) THEN
                chenum(cnum) = chenum(cnum) + 1
                END IF
            END DO
            XXcg = XXcg + xPos(cnum)
            YYcg = YYcg + yPos(cnum)
            ZZcg = ZZcg + zPos(cnum)
            coordinationN = coordinationN + chenum(cnum)
        END DO

        avgCN = coordinationN/rn2
        Xcg = XXcg/rn2
        Ycg = YYcg/rn2
        Zcg = ZZcg/rn2

        totalH = 0
        DO i = rn1, rn1+rn2-1
            h(i) = 1*(Dist(xPos(i), Xcg, yPos(i), Ycg, zPos(i), Zcg))
            totalH = totalH + (h(i))**2
        END DO

        Rg = (totalH/rn2)**0.5  !Radius of gyration of final aggregate

```

### **! CALCULATION OF CHEMICAL BOND ENERGY**

```

E1 = (3.5E-18)*(dp/15E-9)
DO i = rn1, rn1+rn2-1
    che(i) = 0
    Eche1(i) = 0
    !Van1(i) = 0
    DO n = rn1, rn1+rn2-1
        distance4 = Dist(xPos(i), xPos(n), yPos(i), yPos(n), zPos(i),
        zPos(n))
        IF (ABS(distance4 - db) < 0.0001) THEN
            che(i) = che(i) + 1
            Eche1(i) = Eche1(i) + E1*0.5
        END IF
    END DO
END DO

```

```

DO i = rn1, rn1+rn2-1
  DO agg = rn1, i-1
    distance3 = Dist(xPos(i), xPos(agg), yPos(i), yPos(agg), zPos(i),
    zPos(agg))
  END DO
END DO

```

collision = 0

```

DO
  !MOVE PARTICLE
  stepsize = d
  RandomAngle1 = ran2(seed3)
  RandomAngle2 = ran2(seed4)
  Theta1 = 3.14*(RandomAngle1 + 1)
  Theta2 = 3.14*(RandomAngle2 + 1)

  DO i = rn1, rn1+rn2-1
    xPos(i) = xPos(i) + stepsize*cos(Theta1)
    yPos(i) = yPos(i) + stepsize*sin(Theta1)
    zPos(i) = zPos(i) + stepsize*cos(Theta2)
  END DO

```

**!CHECK FOR OUT OF BOUNDS AND CORRECT**

```

num = 0
DO i = rn1, rn1+rn2-1
  IF (xPos(i) < (r-1.6)) THEN
    num = 1
  ELSE IF (xPos(i) > (2.4-r)) THEN
    num = 2
  ELSE IF (zPos(i) < (r-1.6)) THEN
    num = 3
  ELSE IF (zPos(i) > (2.4-r)) THEN
    num = 4
  END IF
END DO

```

```

xmax = xPos(rn1)
DO range = rn1, rn1+rn2-1

```

```

        IF (xPos(range) > xmax) THEN
            xmax = xPos(range)
        END IF
    END DO

```

```

xmin = xPos(rn1)
DO range = rn1, rn1+rn2-1
    IF (xPos(range) < xmax) THEN
        xmin = xPos(range)
    END IF
END DO

```

```

zmax = zPos(rn1)
DO range = rn1, rn1+rn2-1
    IF (zPos(range) > zmax) THEN
        zmax = zPos(range)
    END IF
END DO

```

```

zmin = zPos(rn1)
DO range = rn1, rn1+rn2-1
    IF (zPos(range) < zmin) THEN
        zmin = zPos(range)
    END IF
END DO

```

```

IF (num == 1) THEN
    xadd = 2.4 - r - xmax
    DO i = rn1, rn1+rn2-1
        xPos(i) = xPos(i) + xadd
        yPos(i) = yPos(i)
        zPos(i) = zPos(i)
    END DO

```

```

ELSE IF (num == 2) THEN
    xsub = xmin - r + 1.6
    DO i = rn1, rn1+rn2-1
        xPos(i) = xPos(i) - xsub
        yPos(i) = yPos(i)
        zPos(i) = zPos(i)
    END DO

```

```

ELSE IF (num == 3) THEN
    zadd = 2.4 - r - zmax
    DO i = rn1, rn1+rn2-1
        xPos(i) = xPos(i)

```

```
yPos(i) = yPos(i)
zPos(i) = zPos(i) + zadd
END DO
```

```
ELSE IF (num == 4) THEN
  zsub = zmin - r + 1.6
  DO i = rn1, rn1+rn2-1
    xPos(i) = xPos(i)
    yPos(i) = yPos(i)
    zPos(i) = zPos(i) - zsub
  END DO
```

```
END IF
```

### **! DATA FOR VAN DER WAALS BOND ENERGY**

```
HA = 164.9E-21
ainitial1 = 0.4E-9
strain = 0.01
ainitial2 = (d* ainitial1)/dp
da = d + ainitial2
ra = da/2
```

### **!CHECK FOR COLLISION**

```
collision = 0
DO i = rn1, rn1+rn2-1
  kk = rn1 - 1
  DO k = 1, kk
    APART = Dist(xPos(i), xPos(k), yPos(i), yPos(k), zPos(i),
    zPos(k))

    IF (APART <= da) THEN
      collision = 1
    END IF
  END DO
END DO
```

```
END DO
```

```
IF (collision == 1) EXIT
```

```
END DO
```

**!REMOVING OVERLAP**

DO m = 1,2

DO i = rn1, rn1+rn2-1

DO k = 1, rn1-1

APART = Dist(xPos(i), xPos(k), yPos(i), yPos(k), zPos(i), zPos(k))

IF (APART <= da) THEN

X3 = xPos(i)

Y3 = yPos(i)

Z3 = zPos(i)

CALL SOLVE(xPos(i), xPos(k), yPos(i), yPos(k), zPos(i), zPos(k), ra)

APART = Dist(xPos(i), xPos(k), yPos(i), yPos(k), zPos(i), zPos(k))

X4 = xPos(i)

Y4 = yPos(i)

Z4 = zPos(i)

XX = X4 - X3

YY = Y4 - Y3

ZZ = Z4 - Z3

xPos(i) = xPos(i) - XX

yPos(i) = yPos(i) - YY

zPos(i) = zPos(i) - ZZ

DO ii = rn1, rn1+rn2-1

xPos(ii) = xPos(ii) + XX

yPos(ii) = yPos(ii) + YY

zPos(ii) = zPos(ii) + ZZ

END DO

END IF

END DO

END DO

END DO

rn1 = rn1 + rn2

IF (rn1 >= j) THEN  
EXIT  
END IF

END DO

## **!CALCULATION OF STRAINED VAN DER WAALS BOND ENERGY IN DEPOSIT**

totalvdwbonds = 0

DO i = b4+1, rn1-1

vdw(i) = 0

Van2(i) = 0

DO n = 1, rn1-1

distance4 = Dist(xPos(i), xPos(n), yPos(i), yPos(n), zPos(i),  
zPos(n))

IF (ABS(distance4 - da) < 0.0001) THEN

totalvdwbonds = totalvdwbonds + 1

vdw(i) = vdw(i) + 1

a = ABS(distance4 - d)

dist1 = Dist(xPos(i), xPos(n), yPos(i), yPos(n), zPos(i), zPos(n))

dist2 = Dist(xPos(i), xPos(n), yPos(i), yPos(i), zPos(i), zPos(n))

dist3a = ABS(zPos(i) - zPos(n))

dist3b = SQRT((dist1)\*\*2 - (dist2)\*\*2)

cosAngle = dist2/dist1

ax = a\* cosAngle

dist4 = dist2 + ax\* (strain)

dist5 = SQRT((dist4)\*\*2 + (dist3b)\*\*2)

ao = dist5 - d

xy = a/d

xyy = ao/d

AA1 = xy\*\*2 + 2\*xy

AA2 = xy\*\*2 + 2\*xy + 1

AA3 = xyy\*\*2 + 2\*xyy

AA4 = xyy\*\*2 + 2\*xyy + 1

$$V = (-HA/12) * (((1/AA3)+(1/AA4)+ 2*LOG(AA3/AA4)) - ((1/AA1)+(1/AA2)+ 2*LOG(AA1/AA2)))$$

$$Van2(i) = Van2(i) + V*0.5$$

END IF

END DO

END DO

### **!CALCULATION OF STRAINED CHEMICAL BOND ENERGY IN DEPOSIT**

$$E1 = (3.5E-18)*(dp/15E-9)$$

$$d12 = ainitial1/ dp$$

$$AA5 = d12**2 + 2*d12$$

$$AA6 = d12**2 + 2*d12 + 1$$

$$E2 = (HA/12)* ((1/AA5)+(1/AA6)+ 2*LOG(AA5/AA6))$$

$$cc = ((0.4*E1) - (0.1*E2))/0.3$$

$$mc = (E2 - E1)/0.3E-9$$

$$totalchebonds = 0$$

DO i = b4+1, m1-1

$$Eche2(i) = 0$$

$$Eche3(i) = 0$$

DO n = 1, m1-1

$$distance4 = \text{Dist}(xPos(i), xPos(n), yPos(i), yPos(n), zPos(i), zPos(n))$$

IF (ABS(distance4 - db) < 0.0001) THEN

$$totalchebonds = totalchebonds + 1$$

$$ac = \text{ABS}(distance4 - d)$$

$$dist1c = \text{Dist}(xPos(i), xPos(n), yPos(i), yPos(n), zPos(i), zPos(n))$$

$$dist2c = \text{Dist}(xPos(i), xPos(n), yPos(i), yPos(i), zPos(i), zPos(n))$$

$$dist3ac = \text{ABS}(zPos(i) - zPos(n))$$

$$dist3bc = \text{SQRT}((dist1c)**2 - (dist2c)**2)$$

$$\cosAngle = dist2c/dist1c$$

$$axc = ac * \cosAngle$$

$$dist4c = dist2c + axc * (\text{strain})$$

$$dist5c = \text{SQRT}((dist4c)**2 + (dist3bc)**2)$$

$$aoc = dist5c - d$$

$$achem = (aoc*dp)/d$$

$$xy = ac/d$$

$$xyy = aoc/d$$

$$AA1 = xy**2 + 2*xy$$

$$AA2 = xy**2 + 2*xy + 1$$

$$AA3 = xyy**2 + 2*xyy$$

$$AA4 = xyy**2 + 2*xyy + 1$$

$$CE = (-HA/12)* (((1/AA3)+(1/AA4)+ 2*LOG(AA3/AA4)) - ((1/AA1)+(1/AA2)+ 2*LOG(AA1/AA2)))$$

$$Eche3(i) = Eche3(i) + CE*0.5$$

IF (achem <= ainitial1) THEN

$$E3 = (mc*achem) + cc$$

ELSE

$$d13 = achem/ dp$$

$$AA7 = d13**2 + 2*d13$$

$$AA8 = d13**2 + 2*d13 + 1$$

$$E3 = (HA/12)* ((1/AA7)+(1/AA8)+ 2*LOG(AA7/AA8))$$

END IF

$$Eche2(i) = Eche2(i) + E3*0.5$$

END IF

END DO

END DO

$$\text{StrainEnergy} = 0$$

DO i = b4+1, m1-1

$$\text{Evdw}(i) = \text{Van2}(i)$$

$$\text{Eche}(i) = -(\text{Eche2}(i) - \text{Eche1}(i))$$

$$\text{SE}(i) = \text{Eche3}(i)$$

END DO

WRITE (12,\*) 'totalvdwbonds = ', totalvdwbonds, 'totalchebonds = ', totalchebonds

WRITE (12,\*) 'n,m1-1: xPos(n): yPos(n): zPos(n) after collision'

DO n = 1,m1-1

WRITE(12,\*) n, xPos(n), yPos(n), zPos(n)

END DO

WRITE (12,\*) 'xPos'

DO n = 1,m1-1

WRITE(12,\*) xPos(n)

END DO

WRITE (12,\*) 'yPos'

DO n = 1,m1-1

WRITE(12,\*) yPos(n)

```

END DO
WRITE (12,*) 'zPos'
DO n = 1,m1-1
WRITE(12,*) zPos(n)
END DO

DO n = 1,m1-1
WRITE (13, *) xPos(n)
END DO
DO n = 1,m1-1
WRITE (14, *) yPos(n)
END DO
DO n = 1,m1-1
WRITE (15, *) zPos(n)
END DO
DO n = 1,m1-1
WRITE (16, *) Eche(n)
END DO
DO n = 1,m1-1
WRITE (17, *) Evdw(n)
END DO
DO n = 1,m1-1
WRITE (18, *) SE(n)
END DO

```

## CONTAINS

!Calculate distance between 2 particles: using the center of the particles as the points

```

FUNCTION Dist(X1, X2, Y1, Y2, Z1, Z2)
IMPLICIT NONE
REAL:: X1, X2, Y1, Y2,Z1, Z2, XDist, YDist, ZDist, Dist

XDist = X1 - X2
YDist = Y1 - Y2
ZDist = Z1 - Z2
Dist = SQRT(XDist**2 + YDist**2 + ZDist**2)

END FUNCTION Dist

```

## ! SUBROUTINE SOLVE

!This subroutine removes the overlap by

- !1. Drawing a line between the spheres using the center of the particles
- !2. Now we have 2 spheres (the particles) and a line
- !3. Solve for the intersection point of the line and each sphere
- !4. Based on each sphere, you get 2 set of values for the intersection point  
! as a line will intersect each sphere at two points. Whether the particle is  
! the incoming one or an as deposited one, one set is chosen.
- !5. The distance between the set that is chosen for each sphere is  
! then calculated and the incoming particle which overlapped is moved  
! by that distance on the same line that was drawn previously.

!Variables used are:

!xa1, xa2, ya1, ya2, za1, za2: intersection points of line with deposited particle

!xa, ya, za: the intersection point chosen based on geometry

!xb1, xb2, yb1, yb2, zb1, zb2: intersection points of line with incoming particle

!xb, yb, zb: the intersection point chosen based on geometry

SUBROUTINE SOLVE(X2, X1, Y2, Y1, Z2, Z1, r)

IMPLICIT NONE

REAL, INTENT(INOUT):: X2, X1, Y2, Y1, Z2, Z1

REAL:: r, V1, V2, V3, V, ta1, ta2, tb1, tb2, xa1, ya1, za1

REAL:: xa2, ya2, za2, xb1, yb1, zb1, xb2, yb2, zb2, xa, xb

REAL:: ya, yb, za, zb, deltaX, deltaY, deltaZ, X, Y, Z

X = X2 - X1

Y = Y2 - Y1

Z = Z2 - Z1

IF (X == 0) THEN

V1 = 0

V2 = 2\*Y1\*Y2 - Y1\*\*2 - Y2\*\*2

V3 = 2\*Z1\*Z2 - Z1\*\*2 - Z2\*\*2

V = V1+ V2 + V3

ta1 = 1 + SQRT(-(r\*\*2)/V)

ta2 = 1 - SQRT(-(r\*\*2)/V)

tb1 = SQRT(-(r\*\*2)/V)

tb2 = - (SQRT(-(r\*\*2)/V))

xa1 = X1 + ta1\*(X2 - X1)

ya1 = Y1 + ta1\*(Y2 - Y1)

za1 = Z1 + ta1\*(Z2 - Z1)

$xa2 = X1 + ta2*(X2 - X1)$   
 $ya2 = Y1 + ta2*(Y2 - Y1)$   
 $za2 = Z1 + ta2*(Z2 - Z1)$

$xb1 = X1 + tb1*(X2 - X1)$   
 $yb1 = Y1 + tb1*(Y2 - Y1)$   
 $zb1 = Z1 + tb1*(Z2 - Z1)$

$xb2 = X1 + tb2*(X2 - X1)$   
 $yb2 = Y1 + tb2*(Y2 - Y1)$   
 $zb2 = Z1 + tb2*(Z2 - Z1)$

IF (Z > 0) THEN  
    IF (za1 < za2) THEN  
        za = za1  
        ya = ya1  
    ELSE  
        za = za2  
        ya = ya2  
    END IF

    IF (zb1 > zb2) THEN  
        zb = zb1  
        yb = yb1  
    ELSE  
        zb = zb2  
        yb = yb2  
    END IF

deltaX = 0  
deltaY = abs(ya - yb)  
deltaZ = abs(za - zb)  
X2 = X2 + deltaX  
Z2 = Z2 + deltaZ  
IF (Y > 0) THEN  
    Y2 = Y2 + deltaY  
ELSE  
    Y2 = Y2 - deltaY  
END IF

ELSE IF (Z < 0) THEN  
    IF (za1 > za2) THEN  
        za = za1

```

        ya = ya1
    ELSE
        za = za2
        ya = ya2
    END IF

```

```

    IF (zb1 < zb2) THEN
        zb = zb1
        yb = yb1
    ELSE
        zb = zb2
        yb = yb2
    END IF

```

```

deltaX = 0
deltaY = abs(ya - yb)
deltaZ = abs(za - zb)
X2 = X2 + deltaX
Z2 = Z2 - deltaZ
IF (Y > 0) THEN
    Y2 = Y2 + deltaY
ELSE
    Y2 = Y2 - deltaY
END IF

```

```

END IF

```

```

ELSE

```

```

V1 = 2*X1*X2 - X1**2 - X2**2
V2 = 2*Y1*Y2 - Y1**2 - Y2**2
V3 = 2*Z1*Z2 - Z1**2 - Z2**2
V = V1 + V2 + V3

```

```

ta1 = 1 + SQRT(-(r**2)/V)
ta2 = 1 - SQRT(-(r**2)/V)
tb1 = SQRT(-(r**2)/V)
tb2 = - (SQRT(-(r**2)/V))

```

```

xa1 = X1 + ta1*(X2 - X1)
ya1 = Y1 + ta1*(Y2 - Y1)
za1 = Z1 + ta1*(Z2 - Z1)

```

```

xa2 = X1 + ta2*(X2 - X1)
ya2 = Y1 + ta2*(Y2 - Y1)

```

$$za2 = Z1 + ta2*(Z2 - Z1)$$

$$xb1 = X1 + tb1*(X2 - X1)$$

$$yb1 = Y1 + tb1*(Y2 - Y1)$$

$$zb1 = Z1 + tb1*(Z2 - Z1)$$

$$xb2 = X1 + tb2*(X2 - X1)$$

$$yb2 = Y1 + tb2*(Y2 - Y1)$$

$$zb2 = Z1 + tb2*(Z2 - Z1)$$

IF (X < 0) THEN

  IF (Z > 0) THEN

    IF (xa1 > xa2) THEN

$$xa = xa1$$

$$ya = ya1$$

$$za = za1$$

    ELSE

$$xa = xa2$$

$$ya = ya2$$

$$za = za2$$

  END IF

  IF (xb1 < xb2) THEN

$$xb = xb1$$

$$yb = yb1$$

$$zb = zb1$$

  ELSE

$$xb = xb2$$

$$yb = yb2$$

$$zb = zb2$$

  END IF

$$\text{deltaX} = \text{abs}(xa - xb)$$

$$\text{deltaY} = \text{abs}(ya - yb)$$

$$\text{deltaZ} = \text{abs}(za - zb)$$

$$X2 = X2 - \text{deltaX}$$

$$Z2 = Z2 + \text{deltaZ}$$

IF (Y > 0) THEN

$$Y2 = Y2 + \text{deltaY}$$

ELSE

$$Y2 = Y2 - \text{deltaY}$$

END IF

ELSE IF (Z < 0) THEN

  IF (xa1 > xa2) THEN

```
        xa = xa1
        ya = ya1
        za = za1
ELSE
        xa = xa2
        ya = ya2
        za = za2
END IF
```

```
IF (xb1<xb2) THEN
        xb = xb1
        yb = yb1
        zb = zb1
ELSE
        xb = xb2
        yb = yb2
        zb = zb2
END IF
```

```
deltaX = abs(xa - xb)
deltaY = abs(ya - yb)
deltaZ = abs(za - zb)
X2 = X2 - deltaX
Z2 = Z2 - deltaZ
IF (Y > 0) THEN
Y2 = Y2 + deltaY
ELSE
Y2 = Y2 - deltaY
END IF
```

```
ELSE IF (Z == 0) THEN
        IF (xa1>xa2) THEN
                xa = xa1
                ya = ya1
        ELSE
                xa = xa2
                ya = ya2
        END IF
```

```
IF (xb1<xb2) THEN
        xb = xb1
        yb = yb1
ELSE
        xb = xb2
        yb = yb2
```

END IF

```
deltaX = abs(xa - xb)
deltaY = abs(ya - yb)
deltaZ = 0
X2 = X2 - deltaX
Z2 = Z2 + deltaZ
IF (Y > 0) THEN
Y2 = Y2 + deltaY
ELSE
Y2 = Y2 - deltaY
END IF
```

END IF

```
ELSE IF (X > 0) THEN
  IF (Z > 0) THEN
    IF (xa1 < xa2) THEN
      xa = xa1
      ya = ya1
      za = za1
    ELSE
      xa = xa2
      ya = ya2
      za = za2
    END IF
  END IF
```

```
  IF (xb1 > xb2) THEN
    xb = xb1
    yb = yb1
    zb = zb1
  ELSE
    xb = xb2
    yb = yb2
    zb = zb2
  END IF
```

```
deltaX = abs(xa - xb)
deltaY = abs(ya - yb)
deltaZ = abs(za - zb)
X2 = X2 + deltaX
Z2 = Z2 + deltaZ
IF (Y > 0) THEN
Y2 = Y2 + deltaY
ELSE
```

```
Y2 = Y2 - deltaY
END IF
```

```
ELSE IF (Z < 0) THEN
  IF (xa1 < xa2) THEN
    xa = xa1
    ya = ya1
    za = za1
  ELSE
    xa = xa2
    ya = ya2
    za = za2
  END IF
```

```
  IF (xb1 > xb2) THEN
    xb = xb1
    yb = yb1
    zb = zb1
  ELSE
    xb = xb2
    yb = yb2
    zb = zb2
  END IF
```

```
deltaX = abs(xa - xb)
deltaY = abs(ya - yb)
deltaZ = abs(za - zb)
X2 = X2 + deltaX
Z2 = Z2 - deltaZ
IF (Y > 0) THEN
  Y2 = Y2 + deltaY
ELSE
  Y2 = Y2 - deltaY
END IF
```

```
ELSE IF (Z == 0) THEN
  IF (xa1 < xa2) THEN
    xa = xa1
    ya = ya1
  ELSE
    xa = xa2
    ya = ya2
  END IF
```

```
  IF (xb1 > xb2) THEN
    xb = xb1
```

```
        yb = yb1
    ELSE
        xb = xb2
        yb = yb2
    END IF
```

```
    deltaX = abs(xa - xb)
    deltaY = abs(ya - yb)
    deltaZ = 0
    X2 = X2 + deltaX
    Z2 = Z2 + deltaZ
    IF (Y > 0) THEN
        Y2 = Y2 + deltaY
    ELSE
        Y2 = Y2 - deltaY
    END IF
```

```
    END IF
```

```
    END IF
```

```
    END IF
```

```
END SUBROUTINE SOLVE
```

```
END PROGRAM Nanoparticle_MC_Simulation
```

### C3: Random number generator code

```
FUNCTION ran2(idum)
INTEGER idum,IM1,IM2,IMM1,IA1,IA2,IQ1,IQ2,IR1,IR2,NTAB,NDIV
REAL ran2,AM,EPS,RNMX
PARAMETER(IM1=2147483563,IM2=2147483399,AM=1./IM1,IMM1=IM1-1, &
          IA1=40014,IA2=40692,IQ1=53668,IQ2=52774,IR1=12211,IR2=3791, &
          NTAB=32,NDIV=1+IMM1/NTAB,EPS=1.2e-7,RNMX=1.-EPS)
INTEGER idum2,j,k,iv(NTAB),iy
SAVE iv,iy,idum2
DATA idum2/123456789/,iv/NTAB*0/,iy/0/
if (idum.le.0) then
idum=max(-idum,1)
idum2=idum
do j=NTAB+8,1,-1
k=idum/IQ1
idum=IA1*(idum-k*IQ1)-k*IR1
if (idum.lt.0) idum=idum+IM1
if (j.le.NTAB) iv(j)=idum
end do
iy=iv(1)
endif

k=idum/IQ1
idum=IA1*(idum-k*IQ1)-k*IR1
if (idum.lt.0) idum=idum+IM1
k=idum2/IQ2
idum2=IA2*(idum2-k*IQ2)-k*IR2
if (idum2.lt.0) idum2=idum2+IM2
j=1+iy/NDIV
iy=iv(j)-idum2
iv(j)=idum
if (iy.lt.1) iy=iy+IMM1
ran2=min(AM*iy,RNMX)
return
END FUNCTION ran2
```

#### C4: Density and strain energy calculation code

##### PROGRAM Density\_Calculation

!Program to calculate the porosity and strain energy of the deposit

IMPLICIT NONE

REAL :: LL1, LL2, LL3, LL4, LL5, LL6, LL7, LL8

REAL :: rr, dd, density, voidfraction, TotalStrainEE, Vol,

TotalStrainEE2, TotalStrainEE3

REAL :: Voltotal, density2, voidfraction2

INTEGER :: counter, rn, rnn, ss, s

REAL, DIMENSION(100000) :: xxPos, yyPos, zzPos, EEche, EEvdw, SSE

REAL, DIMENSION(100000) :: chemicalE, vanderwaalsE, ParticlestrainE

OPEN (UNIT = 11, FILE = "C:\MSDEV\PROJECTS\Tosin\density.txt", STATUS =  
"OLD")

OPEN (UNIT = 13, FILE = "C:\MSDEV\PROJECTS\Tosin\data1.txt", STATUS =  
"OLD")

OPEN (UNIT = 14, FILE = "C:\MSDEV\PROJECTS\Tosin\data2.txt", STATUS =  
"OLD")

OPEN (UNIT = 15, FILE = "C:\MSDEV\PROJECTS\Tosin\data3.txt", STATUS =  
"OLD")

OPEN (UNIT = 16, FILE = "C:\MSDEV\PROJECTS\Tosin\data4.txt", STATUS =  
"OLD")

OPEN (UNIT = 17, FILE = "C:\MSDEV\PROJECTS\Tosin\data5.txt", STATUS =  
"OLD")

OPEN (UNIT = 18, FILE = "C:\MSDEV\PROJECTS\Tosin\data6.txt", STATUS =  
"OLD")

PRINT \*, "Enter simulation step of particles"

READ \*, dd

PRINT \*, "Enter rn"

READ \*, rn

PRINT \*, "Enter rnn"

READ \*, rnn

PRINT \*, "Enter s"

READ \*, s

DO ss = rn, s

```
READ (13, *) xxPos(ss)
END DO
```

```
DO ss = rn,s
READ (14, *) yyPos(ss)
END DO
```

```
DO ss = rn,s
READ (15, *) zzPos(ss)
END DO
```

```
DO ss = rn,s
READ (16, *) EEche(ss)
END DO
```

```
DO ss = rn,s
READ (17, *) EEvdw(ss)
END DO
```

```
DO ss = rn,s
READ (18, *) SSE(ss)
END DO
```

```
PRINT *, "Enter dimension LL1 of box in x direction"
READ *, LL1
PRINT *, "Enter dimension LL2 of box in x direction"
READ *, LL2
PRINT *, "Enter dimension LL3 of box in z direction"
READ *, LL3
PRINT *, "Enter dimension LL4 of box in z direction"
READ *, LL4
PRINT *, "Enter dimension LL5 of box in y direction"
READ *, LL5
PRINT *, "Enter dimension rr of box in y direction"
READ *, rr
```

```
counter = 0
TotalStrainEE = 0
TotalStrainEE2 = 0
TotalStrainEE3 = 0
```

```
DO ss = rnn,s
ParticleStrainE(ss) = 0
```

```

chemicalE(ss) = 0
vanderwaalsE(ss) = 0

IF (xxPos(ss) >= LL1 .AND. xxPos(ss) <= LL2) THEN
  IF (zzPos(ss) >= LL3 .AND. zzPos(ss) <= LL4) THEN
    IF (yyPos(ss) >= rr .AND. yyPos(ss) <= LL5) THEN
      counter = counter + 1
      chemicalE(ss) = EEche(ss)
      vanderwaalsE(ss) = EEvdw(ss)
      ParticleStrainE(ss) = SSE(ss)
      TotalStrainEE = TotalStrainEE + vanderwaalsE(ss)
      TotalStrainEE2 = TotalStrainEE2 + vanderwaalsE(ss) +
        chemicalE(ss)
      TotalStrainEE3 = TotalStrainEE3 + vanderwaalsE(ss) +
        ParticleStrainE(ss)
    END IF
  END IF
END IF

END DO

LL6 = abs(LL2 - LL1)/dd
LL7 = abs(LL4 - LL3)/dd
LL8 = abs(LL5 - rr)/dd

Vol = LL6*LL7*LL8
Voltotal = (6*Vol*(dd**3))/(22*(dd**3)/7)
density = counter/Vol
density2 = counter/Voltotal
voidfraction = 1 - density
voidfraction2 = 1 - density2

WRITE (11, *) 'density2', density2,'voidfraction2',voidfraction2, counter, Voltotal
WRITE (11, *) 'ss: vanderwaalsE(ss): chemicalE(ss): ParticleStrainE(ss) '
WRITE (11, *) 'TotalStrainEE is', ' ', TotalStrainEE
WRITE (11, *) 'TotalStrainEE2 is', ' ', TotalStrainEE2
WRITE (11, *) 'TotalStrainEE3 is', ' ', TotalStrainEE3

END PROGRAM Density_Calculation

```

## REFERENCES

1. M. Baraton, L. Merhari, J. Wang, and K. E. Gonsalves: Investigation of the TiO<sub>2</sub> / PPV nanocomposite for gas sensing applications. *Nanotechnology* **9**, 356 (1998).
2. H. Tang, K. Prasad, R. Sanjines, and F. Levy: TiO<sub>2</sub> anatase thin films as gas sensors. *Sensors and Actuators B* **26**, 71 (1995).
3. C. J. Yu, W. Ho, J. Lin, H. Yip, and P. K. Wong: Photocatalytic activity, antibacterial effect, and photoinduced hydrophilicity of TiO<sub>2</sub> films coated on a stainless steel substrate. *Environ. Sci. Tech.* **37**, 2296 (2003).
4. J. Yu, and L. Chan: Photocatalytic degradation of a gaseous organic pollutant. *J. Chem. Ed.* **75**, 750 (1998).
5. Y. Ohko, K. Hashimoto, and A. Fujishima: Kinetics of photocatalytic reactions under extremely low-intensity UV illumination on titanium dioxide thin films. *J. Phy. Chem. A* **101**, 8057 (1997).
6. D. S. Hinczewski, M. Hinczewski, F. Z. Tepehan, and G. G. Tepehan: Optical filters from SiO<sub>2</sub> and TiO<sub>2</sub> multi-layers using sol-gel spin coating method. *Solar Energy Materials & Solar Cells* **87**, 181 (2005).
7. M. Grätzel, S. Y. Huang, L. Kavan, and I. Exnar: Rocking chair lithium battery based on nanocrystalline TiO<sub>2</sub> (anatase). *J. Electrochem. Soc.* **142**, L142 (1995).
8. C. J. Barbe, F. Arendse, P. Comte, M. Jirousek, F. Lenzmann, V. Shklover, and M. Grätzel: Nanocrystalline titanium oxide electrodes for photovoltaic applications. *J. Am. Ceram. Soc.* **80**, 3157 (1997).
9. C. H. Winter, P. H. Sheridan, T. S. Lewkebandara, M. J. Heeg, and J. W. Proscia: A single source precursor to titanium nitride thin films, evidence for the intermediacy of imido complexes in the chemical vapor deposition process. *J. Am. Che. Soc.* **114**, 1095 (1992).
10. J. P. Dekker, P. J. V. d. Put, H. J. Veringa, and J. Schoonman: Gas-to-particle conversion in the particle precipitated-aided chemical vapor deposition process I: synthesis of the binary compound titanium nitride. *Aerosol Sci. & Tech.* **19**, 549 (1993).
11. L. J. Meng, C. P. Moreira, and M. P. Santos: Study of porosity of titanium oxide films by X-ray photoelectron spectroscopy and IR transmittance. *Thin Solid Films* **239**, 117 (1994).
12. Y. Han, S. Hong, and K. Xu: Porous nanocrystalline titania films by plasma electrolytic oxidation. *Surface & Coatings Tech.* **154**, 314 (2002).
13. G. Tang, R. Zhang, Y. Yan, and Z. Zhu: Preparation of porous anatase titania film. *Mat. Lett.* **58**, 1857 (2004).
14. S. Seifried, M. Winterer, and H. Hahn: Nanocrystalline titania films and particles by chemical vapor synthesis. *Chemical Vapor Deposition* **6**, 239 (2000).
15. S. Miyake, K. Honda, T. Kohno, Y. Setsuhara, M. Satou, and A. Chayahara: Rutile-type TiO<sub>2</sub> formation by ion beam dynamic mixing. *J. Vac. Sci. Technol. A* **10**, 3253 (1992).
16. M. Gratzel: Conversion of sunlight to electric power by nanocrystalline dye-sensitized solar cells. *J. Photochemistry & Photobiology A* **164**, 3 (2004).

17. S. Nakade, Y. Saito, W. Kubo, T. Kitamura, Y. Wada, and S. Yanagida: Influence of TiO<sub>2</sub> nanoparticle size on electron diffusion and recombination in dye-sensitized TiO<sub>2</sub> solar cells. *J. Phys. Chem. B* **107**, 8607 (2003).
18. P. D. Almeida, J. V. Deelen, C. Catry, H. Sneyers, T. Pataki, R. Andriessen, C. V. Roost, and J. Kroon: Microstructure characterization of titanium dioxide nanodispersions and thin films for dye-sensitized solar cell devices. *App. Phys. A* **79**, 1819 (2004).
19. P. Wang, C. Klein, R. Humphry-Baker, S. Zakeeruddin, and M. Gratzel: A high molar extinction coefficient sensitizer for stable dye-sensitized solar cells. *J. Am. Chem. Soc.* **127**, 808 (2005).
20. K. Takeuchi, and N. Negishi: Structural changes of transparent TiO<sub>2</sub> thin films with heat treatment. *Mat. Lett.* **38**, 150 (1999).
21. C. K. Chan, J. F. Porter, Y. Li, W. Guo, and C. Chan: Effects of calcinations on the microstructures and photocatalytic properties of nanosized titanium dioxide powders prepared by vapor hydrolysis. *J. Am. Ceram. Soc.* **82**, 566 (1999).
22. L. Hu, S. Dai, and K. Wang: Influence of particle coordination number in nanoporous TiO<sub>2</sub> films on the performance of dye-sensitized solar cell modules. *Chin. Phys. Lett.* **22**, 493 (2005).
23. J. Lagemaat, K. D. Benkstein, and A. J. Frank: Relation between particle coordination number and porosity in nanoparticle films: implications to dye-sensitized solar cells. *J. Phy. Chem. B* **105**, 12433 (2001).
24. M. J. Cass, F. L. Qiu, A. B. Walker, A. C. Fisher, and L. M. Peter: Influence of grain morphology on electron transport in dye sensitized nanocrystalline solar cells. *J. Phy. Chem. B* **107**, 113 (2003).
25. K. Benkstein, N. Kopdakis, J. v. d. Lagemaat, and A. Frank: Influence of the percolation network geometry on electron transport in dye-sensitized titanium dioxide solar cells. *J. Phys. Chem. B* **107**, 7759 (2003).
26. P. Biswas, and P. Kulkarni: A Brownian dynamics simulation to predict morphology of nanoparticle deposits in the presence of interparticle interactions. *Aerosol Sci. Tech.* **38**, 541 (2004).
27. S. K. Friedlander, W. Rong, A. E. Pelling, A. Ryan, and J. K. Gimzewski: Complementary TEM and AFM force spectroscopy to characterize the nanomechanical properties of nanoparticle chain aggregates. *Nano Lett.* **4**, 2287 (2004).
28. F. A. Bonilla, G. U. Lee, Q. T. Nguyen, and S. H. Ehrman: Mechanical properties of aluminium oxide by nanoindentation (2003).
29. N. Castillo, D. Olguin, and A. Conde-Gallardo: Structural and morphological properties of TiO<sub>2</sub> thin films prepared by spray pyrolysis. *Revista Mexicana de Fisica* **50**, 382 (2004).
30. R. Palgrave, and I. Parkin: Aerosol assisted CVD of photochromic tungsten oxide and doped tungsten oxide films. *J. Mater. Chem.* **14**, 2864 (2004).
31. J. Klemberg-Sapieha, J. Oberste-Berghaus, L. Martinu, R. Blacker, I. Stevenson, G. Sadkhin, D. Morton, S. McEldowney, R. Klinger, P. Martin, N. Court, S. Dligatch, M. Gross, and R. Netterfield: Mechanical characteristics of optical coatings prepared by various techniques: a comparative study. *Applied Optics* **43**, 2670 (2004).

32. H. Demiryont, L. Thompson, and G. Collins: Optical properties of aluminum oxynitrides deposited by laser-assisted CVD. *Applied Optics* **25**, 1311 (1986).
33. A. Gurav, T. Kodas, T. Pluym, and Y. Xiong: Aerosol processing of materials. *Aerosol Sci. & Tech.* **19**, 411 (1993).
34. Q. T. Nguyen, S. H. Ehrman, and J. N. Kidder: Hybrid gas-to-particle conversion and chemical vapor deposition for the production of porous alumina films. *Thin Solid Films* **410**, 42 (2002).
35. J. McMurry: *Organic Chemistry*. (Brooks. Pacific Grove, 1988).
36. R. A. Nyquist, and R. O. Kagel (1997): *Handbook of infrared and Raman spectra of inorganic compounds and organic salts*, Academic Press, San Diego.
37. C. Suryanarayana, and M. Norton: *X-ray diffraction: a practical approach*. (Plenum Press. New York, 1998).
38. D. Williams, and C. Carter: *Transmission electron microscopy*. (Plenum Press. New York, 1996).
39. R. Keyse: *Introduction to scanning transmission electron microscopy*. (Springer. New York, 1998).
40. T. Allen: *Particle size measurement*. (Chapman and Hall. London, 1990).
41. T. Allen: *Powder sampling and particle size determination*. (Elsevier. Amsterdam, 2003).
42. N. A. Burnham, and R. J. Colton: Measuring the nanomechanical properties and surface forces of materials using an atomic force microscope. *J. Vac. Sci. Technol. A* **7**, 2906 (1989).
43. P. K. Valavala, and G. M. Odegard: Modeling techniques for determination of mechanical properties of polymer nanocomposites. *Rev. Adv. Mater. Sci.* **9**, 34 (2005).
44. K. Chou, K. Huang, and H. Lee: Fabrication and sintering effect on the morphologies and conductivity of nano-Ag particle films by the spin coating method. *Nanotechnology* **16**, 779 (2005).
45. H. Sakaue, N. Yoshimura, S. Shingubara, and T. Takahagi: Low dielectric constant porous diamond films formed by diamond nanoparticles. *App. Phys. Lett.* **83**, 2226 (2003).
46. K. McKenzie, F. Marken, M. Hyde, and R. Compton: nanoporous iron oxide membranes: layer-by-layer deposition and electrochemical characterisation of processes within nanopores. *New Journal of Chem.* **26**, 625 (2002).
47. J. Wrzyszc, H. Grabowska, M. Zawadzki, L. Kepinski, and L. Krajczyk: A method to produce porous platinum film. *Platinum Metals Rev.* **49**, 138 (2005).
48. U. Backman, A. Auvinen, and J. Jokiniemi: Deposition of nanostructured titania films by particle-assisted MOCVD. *Surface & Coatings Tech.* **192**, 81 (2005).
49. S. E. Pratsinis, and S. Vemury: Particle formation in gases: a review. *Powder Tech.* **88**, 267 (1996).
50. S. K. Friedlander: *Smoke, Dust and Haze*. (Oxford. New York, 2000).
51. K. Ogawa, T. Vogt, M. Ullmann, S. Johnson, and S. K. Friedlander: Elastic properties of nanoparticle chain aggregates of TiO<sub>2</sub>, Al<sub>2</sub>O<sub>3</sub>, and Fe<sub>2</sub>O<sub>3</sub> generated by laser ablation. *J. App. Phy.* **87**, 63 (2000).
52. S. Froeschke, S. Kohler, A. P. Weber, and G. Kasper: Impact fragmentation of nanoparticle agglomerates. *Aerosol Sci.* **34**, 275 (2003).

53. S. Tsantilis, and S. Pratsinis: Soft- and hard-agglomerate aerosols made at high temperatures. *Langmuir* **20**, 5933 (2004).
54. K. Nakaso, K. Okuyama, M. Shimada, and S. Pratsinis: Effect of reaction temperature on CVD-made TiO<sub>2</sub> primary particle diameter. *Chem. Eng. Sci.* **58**, 3327 (2003).
55. Y. Sun, T. Egawa, L. Zhang, and X. Yao: Effect of collection distance on the lattice structure of anatase titania nanoparticles prepared by metalorganic chemical vapor deposition. *Japanese J. App. Phys.* **41**, L1389 (2002).
56. C. S. Kim, K. Nakaso, B. Xia, K. Okuyama, and M. Shimada: A new observation on the phase transformation of TiO<sub>2</sub> nanoparticles produced by a CVD method. *Aerosol Sci. and Tech.* **39**, 104 (2005).
57. C. S. Kim, K. Okuyama, K. Nakaso, and M. Shimada: Direct measurement of nucleation and growth modes in titania nanoparticles generation by a CVD method. *J. Chem. Eng. of Japan* **37**, 1379 (2004).
58. Q. T. Nguyen: Thesis, University of Maryland (2003).
59. J. P. Cleveland, S. Manne, D. Bocek, and P. K. Hansma: A nondestructive method for determining the spring constant of cantilevers for scanning force microscopy. *Rev. Sci. Instruments* **64**, 403 (1993).
60. W. C. Oliver, and G. M. Pharr: An improved technique for determining hardness and elastic modulus using load and displacement sensing indentation experiments. *J. Mater. Res.* **7**, 1564 (1992).
61. M. Arnold, A. R. Boccaccini, and G. Ondracek: Prediction of the poisson's ratio of porous materials. *J. Mater. Sci.* **31**, 1643 (1996).
62. *Hanawalt search manual for experimental patterns: Inorganic phases*. (International centre for diffraction data. Pennsylvania, 2001).
63. P. F. DeCarlo, J. G. Slowik, D. R. Worsnop, P. Davidovits, and J. L. Jimenez: Particle morphology and density characterization by combined mobility and aerodynamic diameter measurements. Part 1: theory. *Aerosol. Sci. Tech.* **38**, 1185 (2004).
64. R. M. German: *Sintering theory and practice*. (Wiley. New York, 1996).
65. M. Astier, and P. Vergnon: Determination of the diffusion coefficients from sintering data of ultrafine oxide particles. *J. Solid State Chem.* **19**, 67 (1976).
66. M. R. Zachariah, and M. J. Carrier: Molecular dynamics computation of gas phase nanoparticle sintering: a comparison with phenomenological models. *J. Aerosol Sci.* **30**, 1139 (1999).
67. J. H. Seinfeld: *Atmospheric chemistry and physics of air pollution*. (Wiley. New York, 1986).
68. D. Mukherjee, C. G. Sonwane, and M. R. Zachariah: Kinetic Monte Carlo simulation of the effect of coalescence energy release on the size and shape evolution of nanoparticles grown as an aerosol. *J. Chemical Phys.* **119**, 3391 (2003).
69. K. Nakaso, T. Fujimoto, T. Seto, M. Shimada, K. Okuyama, and M. Lunden: Size distribution change of titania nano-particle agglomerates generated by gas phase reaction, agglomeration, and sintering. *Aerosol Sci. & Tech.* **35**, 929 (2001).
70. A. Latapie, and D. Farkas: Effect of grain size on the elastic properties of nanocrystalline alpha iron. *Scripta Materiala* **48**, 611 (2003).

71. R. Dingreville, J. Qu, and M. Cherkaoui: Surface free energy and its effect on the elastic behavior of nano-sized particles, wires and films. *J. Mech. & Phy. Solids* **53**, 1827 (2005).
72. G. S. Upadhyaya: *Sintered metallic and ceramic materials*. (Wiley. England, 2000).
73. M. M. Lunden: Thesis, California Institute of Technology (1995).
74. B. Xia, H. Huang, and Y. Xie: Heat treatment on titania nanoparticles prepared by vapor-phase hydrolysis. *Mater. Sci. Eng. B* **57**, 150 (1999).
75. I. K. Yudin, G. L. Nikolaenko, V. I. Kosov, V. A. Agayan, M. A. Anisimov, and J. V. Sengers: A compact photon-correlation spectrometer for research and education. *International J. Thermophysics* **18**, 1237 (1997).
76. C. P. Green, H. Lioe, J. P. Cleveland, R. Proksch, P. Mulvaney, and J. E. Sader: Normal and torsional spring constants of atomic force microscope cantilevers. *Rev. Sci. Instrum.* **75**, 1988 (2004).
77. J. S. Field, and M. V. Swain: A simple predictive model for spherical indentation. *J. Mater. Res.* **8**, 297 (1993).
78. M. Mayo, R. Siegel, A. Narayanasamy, and W. Nix: Mechanical properties of nanophase TiO<sub>2</sub> as determined by nanoindentation. *J. Mater. Res.* **5**, 1073 (1990).
79. J. Gross, G. Reichenauer, and J. Fricke: Mechanical properties of SiO<sub>2</sub> aerogels. *J. Phys. D* **21**, 1447 (1988).
80. A. P. Roberts, and E. J. Garboczi: Elastic properties of model porous ceramics. *J. Am. Ceram. Soc.* **83**, 3041 (2000).
81. R. W. Zimmerman: Elastic moduli of a solid containing spherical inclusions. *Mech. Mater.* **12**, 17 (1991).
82. N. Ramakrishnan, and V. S. Arunachalam: Effective elastic moduli of porous ceramic materials. *J. Am. Ceram. Soc.* **76**, 2745 (1993).
83. A. P. Roberts, and E. J. Garboczi: Elastic properties of model random three-dimensional open-cell solids. *J. Mech. & Phy. Solids* **50**, 33 (2002).
84. L. J. Gibson, and M. F. Ashby: The mechanics of three dimensional cellular materials. *Proc. R. Soc. Lond. Ser A* **382**, 43 (1982).
85. A. P. Roberts: Morphology and thermal conductivity of model organic aerogels. *Phy. Rev. E.* **55**, R1286 (1997).
86. P. Meakin: Computer simulation of cluster-cluster aggregation using linear trajectories: results from three-dimensional simulations and a comparison with aggregates formed using brownian trajectories. *J. Colloid and Interfcae Sci.* **102**, 505 (1984).
87. P. Meakin: Ballistic deposition on surfaces. *Phy. Rev. A.* **34**, 5091 (1986).
88. P. Tandon, and D. Rosner: Monte carlo simulation of particle aggregation and simultaneous restructuring. *J. Colloid and Interfcae Sci.* **213**, 273 (1999).
89. M. Giona, and O. Patierno: Monte carlo simulation of aggregation processes. *Chem. Eng. Comm.* **121**, 219 (1993).
90. A. Dalis, and S. Friedlander: Molecular dynamics simulations of the straining of nanoparticle chain aggregates - the case of copper. *Nanotechnology* **16**, S626 (2005).
91. G. Odegard, T. Gates, L. Nicholson, and K. Wise: Equivalent-continuum modeling of nano-structured materials. *Comp. Sci. Tech.* **62**, 1869 (2002).

92. H. C. Hamaker: The London-Van der Waals attraction between spherical particles. *Physica* **4**, 1058 (1937).
93. O. Ogunsola, J. Park, G. Lee, and S. Ehrman: Physical properties of porous titania films composed of nanoparticle aggregates. *Manuscript in preparation* (2005).
94. R. G. Munro: *Elastic moduli data for polycrystalline ceramics*. (NISTIR, 2002).
95. T. Woignier, J. Reynes, A. Alaoui, I. Beurroies, and J. Phalippou: Different kinds of structure in aerogels: relationships with the mechanical properties. *J. Non-Cryst. Solids* **241**, 45 (1998).
96. M. Moner-Girona, A. Roig, E. Molins, E. Martinez, and J. Esteve: Micromechanical properties of silica aerogels. *App. Phys. Lett.* **75**, 653 (1999).
97. H. Ma, J. Prevost, R. Jullien, and G. Scherer: Computer simulation of mechanical structure-property relationship of aerogels. *J. Non-Cryst. Solids* **285**, 216 (2001).